# Design and synthesis of gas permeation membranes for extracorporeal membrane oxygenation (ECMO)

**Maria Inês Bairos Teixeira Coelho**

Thesis to obtain the Master of Science Degree in

**Materials Engineering**

Supervisors:
Dr. Mónica Cristina Faria Besteiro
Prof. Vasco Daniel Bigas Bonifácio

**Examination Committee:**

Chairperson: Prof. José Paulo Sequeira Farinha
Supervisor: Dr. Mónica Cristina Faria Besteiro
Member of the committee: Dr. Liliana Sofia Carvalho Tomé

**May 2022**

# Acknowledgments

First and foremost, I would like to express my deep appreciation to my supervisors, Dr. Mónica Faria and professor Vasco Bonifácio, for the time and attention devoted to this thesis, as well as all the invaluable knowledge and guidance they provided.

I also wish to thank Dr. Anirban Karmakar for kindly contributing the metal organic frameworks used in this work, and Dr. Sérgio Gonçalves for the great assistance and advice extended during the mechanical tests.

Thank you also to professor Pedro Morgado and Tiago Eusébio for sharing with me their vast experience and knowledge of the gas permeation set-up.

I would like to offer a special thank you to Flávia and Rita for all their help during the various phases of this work, it was much appreciated.

I would also like to extend my deepest gratitude to my parents for the incredible example they set and for giving me the freedom to pave my own path. I must also thank my sister for her unconditional support and motivation.

I am very grateful for Duarte and the immense amount of patience and encouragement imparted over the course of this journey.

And last but not least, I am thankful for my great friends, Madalena and Beatriz, who were such an important part of my time at IST.

# Abstract

Three groups of nonporous symmetric membranes were prepared by the solvent evaporation technique: pure polyurethane (PU) membranes, polyurethane-based membranes with tris(hydroxymethyl)aminomethane (TRIS), Congo red (CR) and methyl-beta-cyclodextrin (MBCD), and mixed matrix membranes (MMMs) incorporating Zn-$NH_2$-BDC and Cu-BTC metal organic frameworks (MOFs). The solvent used in the preparation of the casting solutions was dimethylformamide (DMF). Different total polymer/solvent and polyurethane/second reagent weight ratios were used across the different formulations.

All the membranes were examined by scanning electron microscopy (SEM), which revealed their nonporous, dense cross-section morphology. Energy-dispersive X-ray spectroscopy (EDS) was performed on the MMMs to confirm the presence of MOFs. The chemical nature of the membranes was characterized by Attenuated total reflection (ATR)–Fourier transform infrared (FTIR) spectroscopy. Tensile tests were performed on the pure polyurethane and polyurethane-based membranes to determine mechanical properties such as the Young's modulus, tensile strength, and elongation at break.

Single gas, oxygen ($O_2$) and carbon dioxide ($CO_2$) permeation studies were carried out by the constant volume method at 37 °C in an in-house built experimental set-up. The permeability coefficients obtained from the permeation curves ranged from 237 to 346 Barrer for $CO_2$ and 24 to 30 Barrer for $O_2$. The ranges obtained for the diffusion coefficients by the time-lag method were $1.4x10^{-6}$-$3.1x10^{-6}$ $cm^2/s$ for $CO_2$ and $1.5x10^{-6}$-$2.6x10^{-6}$ $cm^2/s$ for $O_2$, and the ranges obtained for the solubility coefficients were $114.5x10^{-4}$-$185.5x10^{-4}$ $cm^3/cm^3.cmHg$ for $CO_2$, and $11.4x10^{-4}$-$16.6x10^{-4}$ $cm^3/cm^3.cmHg$ for $O_2$.

**Keywords:** Membrane blood oxygenator; Gas permeation; Nonporous symmetric membranes; Bi-soft segment polyurethanes; Mixed matrix membranes; Time-lag.

# Resumo

Três grupos de membranas simétricas não porosas foram preparados pelo método de evaporação de solvente: membranas de poliuretano (PU) puro, membranas mistas de PU com tris(hidroximetil) aminometano (TRIS), Congo red (CR) e metill-beta-ciclodextrina (MBCD), e membranas de matriz mista de PU com redes organometálicas (MOFs), nomeadamente Zn-$NH_2$-BDC e Cu-BTC. O solvente utilizado na preparação das soluções de casting foi dimetilformamida (DMF). Diferentes razões mássicas de polímero/solvente e de poliuretano/segundo reagente foram usadas para as diversas composições.

A morfologia das membranas foi caracterizada por microscopia eletrónica de varrimento (MEV) e a presença de MOFs nas membranas de matriz mista foi confirmada utilizando espectroscopia de raios-X por dispersão em energia (EDS). A natureza química das membranas foi caracterizada por espectroscopia de infravermelho (FTIR-ATR). Os ensaios de tração realizados nas membranas permitiram calcular propriedades mecânicas como o módulo de Young, resistência à tração e extensão de rotura.

Foram executados testes de permeação gasosa com dióxido de carbono ($CO_2$) e oxigénio ($O_2$) em todas as membranas, através do método do volume constante a 37°C numa instalação de permeação já existente. A partir das curvas de permeação, obtiveram-se coeficientes de permeabilidade de 237-346 Barrer e de 24-30 Barrer para o $CO_2$ e $O_2$ respetivamente. Os coeficientes de difusão, calculados pelo método do time-lag, encontram-se entre $1.4x10^{-6}$ e $3.1x10^{-6}$ $cm^2/s$ para o $CO_2$, e entre $1.5x10^{-6}$ e $2.6x10^{-6}$ $cm^2/s$ para o $O_2$. Os coeficientes de solubilidade obtidos para o $CO_2$ e $O_2$ foram de $114.5x10^{-4}$-$185.5x10^{-4}$ $cm^3/cm^3.cmHg$ e $11.4$ $x10^{-4}$-$16.6x10^{-4}$ $cm^3/cm^3.cmHg$, respetivamente.

**Palavras-chave:** Oxigenador de sangue; Permeação gasosa; Membranas simétricas não porosas; Poliuretanos com dois segmentos flexíveis; Membranas de matriz mista; Time-lag.

# Table of Contents

**List of Tables** ..... **ix**

**List of Figures** ..... **xi**

**List of Abbreviations** ..... **xv**

**List of Symbols** ..... **xvii**

**1. Introduction** ..... **1**

1.1. Cardiopulmonary bypass ..... 2

1.2. Membrane blood oxygenators ..... 3

1.3. Extracorporeal membrane oxygenation ..... 4

1.4. Membranes for gas permeation processes ..... 6

1.4.1. Pure polymer membranes ..... 7

1.4.2. Copolymer and polymer blend membranes ..... 8

1.4.3. Mixed matrix membranes ..... 9

1.4.4. Membrane structure and synthesis ..... 10

1.5. Membranes for membrane blood oxygenators ..... 11

1.5.1. PU/PBDO membranes ..... 13

1.5.2. PU/PDMS membranes ..... 13

1.5.3. PU/PCL membranes ..... 13

**2. Framework and Thesis Objectives** ..... **17**

**4. Experimental** ..... **19**

4.1. Materials ..... 19

4.1.1. Materials for membrane synthesis ..... 19

4.1.2. Commercial membrane ..... 20

4.1.3. Gases for permeation tests ..... 21

4.2. Membrane synthesis ..... 21

4.2.1. Group 1: Pure polyurethane membranes ..... 21

4.2.2. Group 2: Polyurethane-based membranes ..... 22

4.2.3. Group 3: Mixed Matrix Membrane ..... 23

4.3. Membrane characterization ..... 24

4.3.1. Scanning Electron Microscopy and Energy-dispersive X-ray spectroscopy ..... 24

4.3.2. Attenuated Total Reflectance - Fourier Transform Infrared Spectroscopy ..... 24
4.3.3. Mechanical Tests ..... 25
4.4. Gas permeation experiments ..... 26
4.4.1. Theory ..... 26
4.4.2. Experimental set-up ..... 30
4.4.3. Procedure ..... 33
**5. Results and Discussion ..... 35**
5.1. Scanning Electron Microscopy ..... 35
5.2. Energy-Dispersive X-ray Spectroscopy ..... 39
5.3. Attenuated Total Reflectance – Fourier Transform Infrared Spectroscopy ..... 41
5.4. Mechanical Tests ..... 44
5.5. Gas permeation experiments ..... 49
5.5.1. Permeate pressure as a function of time ..... 49
5.5.2. Volumetric flux as a function of the transmembrane pressure ..... 51
5.5.3. Permeances and permeability coefficients ..... 54
5.5.4. Commercial membrane ..... 57
5.5.5. $CO_2/O_2$ selectivities ..... 58
5.5.6. Total Surface Area required ..... 59
5.5.7. Diffusion and Solubility Coefficients ..... 60
**6. Conclusions ..... 63**
**7. Perspectives of Future Work ..... 65**
**8. Bibliography ..... 67**
**Appendix A ..... 71**
**Appendix B ..... 73**
**Appendix C ..... 74**

# List of Tables

Table 1. Average thickness ($\ell$) and respective standard deviation of the nonporous symmetric PU membranes from groups 1, 2 and 3, obtained from the SEM cross-sectional images. ..... 38
Table 2. Summary of the elements detected in the PU/Zn-$NH_2$-BDC membrane through Energy-dispersive X-ray Spectroscopy, with its respective atomic numbers and weight percentages. ..... 39
Table 3. Summary of the elements detected in the PU/Cu-BTC-1.0 membrane through Energy-dispersive X-ray Spectroscopy, with its respective atomic numbers and weight percentages. ..... 40
Table 4. Mechanical properties of the pure polyurethane and polyurethane-based membranes, obtained from the tensile tests. ..... 46
Table 5. Average $CO_2$ and $O_2$ permeances (Perm) and permeability coefficients (P) with respective standard deviations for all the studied membranes. ..... 54
Table 6. Membrane thickness ($\ell$) with respective standard deviation, permeance (Perm) and permeability coefficient (P) values obtained for $CO_2$ and $O_2$ through a sample of the commercial membrane. ..... 58
Table 7. $CO_2/O_2$ selectivity ($\alpha$) for all the studied membranes. ..... 58
Table 8. Volumetric fluxes and estimated required membrane surface areas for all formulations. ..... 59
Table 9. Time lag values ($t_{lag}$) diffusion coefficients (D) and solubility coefficients (S) obtained from the $O_2$ and $CO_2$ permeation curves for all the studied membranes. ..... 60
Table 10. Average thickness ($\ell$) and respective standard deviation of the nonporous symmetric PU membranes from groups 1, 2 and 3, obtained with manual and digital calipers. ..... 73
Table 11. Assignments of the ATR-FTIR spectra of the PU prepolymer and the PU-based membranes. ..... 74

# List of Figures

Figure 1. Principle of membrane blood oxygenation [7]. ..... 3
Figure 2. Schematic representation of an ECMO System [6]. ..... 4
Figure 3. Schematic representation of: a) VA ECMO, b) VV ECMO. FA is the femoral artery, FV the femoral vein, SVC the superior vena cava and IVC the inferior vena cava [6]. ..... 5
Figure 4. Chemical structures of: a) polyurethane prepolymer (PU), b) tris(hydroxymethyl) aminomethane (TRIS) , c) Congo red (CR), and d) methyl-beta-cyclodextrin (MBCD). ..... 19
Figure 5. Crystal structures of: a) Zn-$NH_2$-BDC [43] and b) Cu-BTC [44]. The blue tetrahedra represent the Zn atoms while the red, black, blue and green spheres represent the O, C, N and Cu atoms, respectively. ..... 20
Figure 6. Scanning electron microscopy (SEM) images of the commercial membrane: (a) upper surface, (b) bottom support surface and (c) cross-section [44]. ..... 21
Figure 7. Chemical structure of two conjugated PU prepolymer units. ..... 21
Figure 8. Possible chemical structures obtained from the reaction of PU and TRIS when the reaction occurs between the NCO group of PU and a) the OH group of TRIS, or b) the $NH_2$ group of TRIS. ..... 22
Figure 9. Possible chemical structure obtained from the reaction between the NCO group of PU and the $NH_2$ group of CR. ..... 23
Figure 10. Possible chemical structure obtained from the reaction between the NCO group of PU and the OH group of MBCD. ..... 23
Figure 11. Photograph of the Nicolet 5700 FT-IR spectrometer with Golden Gate MKII ATR accessory. ..... 25
Figure 12. Photograph of the Instron® 5544 universal testing machine and Instron® model 2663-822 standard video extensometer. ..... 25
Figure 13. Dimensions of a tensile test specimen. ..... 26
Figure 14. Schematic of gas separation through a membrane [49]. ..... 27
Figure 15. Plot of the permeate pressure versus time, showing the penetration, transient and steady regions. ..... 27
Figure 16. Plot of the permeate pressure versus time showing the time lag value, $t_{lag}$, at the interception of the x axis ($p_p$=0) and the steady state asymptote. ..... 30
Figure 17. Schematic representation of the gas permeation set-up [43]. ..... 31
Figure 18. Schematic representation of the permeation cell [44]. ..... 31
Figure 19. Photograph of the experimental set-up used for permeation measurements. ..... 32
Figure 20. SEM images of the nonporous symmetric PU membrane: (a) top surface (2000×), (b) cross-section (800x). ..... 35
Figure 21. SEM images of the nonporous symmetric PU-s* and PU-s membranes: (a) top surface of PU-s* (2000x), (b) cross-section of the of PU-s* (800x); (c) top surface of PU-s (2000x), (d) cross-section of PU-s (800x). ..... 35

Figure 22. SEM images of the nonporous symmetric PU/TRIS, PU/CR and PU/MBCD membranes: (a) top surface of PU/TRIS (2000x), (b) cross-section of PU/TRIS (800x); (c) top surface of PU/CR (2000x), (d) cross-section of PU/CR (800x); (e) top surface of PU/MBCD (2000x), (f) cross-section of PU/MBCD (800x)..... 36
Figure 23. SEM images of the nonporous symmetric PU/Zn-NH2-BDC, PU/Cu-BTC-0.1 and PU/Cu-BTC-1.0 membranes: (a) top surface of PU/Zn-NH2-BDC (2000x), (b) cross-section of PU/Zn-NH2-BDC (800x); (c) top surface of PU/Cu-BTC-0.1 (2000x), (d) cross-section of PU/Cu-BTC-0.1 (800x); (e) top surface of PU/Cu-BTC-1.0 (2000x), (f) cross-section of PU/Cu-BTC-1.0 (800x)..... 37
Figure 24. Energy-dispersive X-ray spectrum of the PU/Zn-$NH_2$-BDC membrane. The inset image shows the region of the sample that was analyzed (circled in blue)..... 39
Figure 25. Energy-dispersive X-ray spectrum of the PU/Cu-BTC-1.0 membrane. The inset image shows the region of the sample that was analyzed (circled in blue)..... 40
Figure 26. ATR-FTIR spectra of the uncured PU prepolymer and the PU, PU-s, PU/TRIS, PU/CR and PU/MBCD membranes..... 41
Figure 27. ATR-FTIR spectra of the uncured PU prepolymer and of the PU, PU/Zn-NH2-BDC, PU/Cu-BTC-0.1 and PU/Cu-BTC-1.0 membranes..... 42
Figure 28. ATR-FTIR spectra of the PU prepolymer, TRIS compound and PU/TRIS membrane..... 43
Figure 29. Photographs of the mechanical test specimens after rupture for the following compositions: (a) PU, (b) PU-s, (c) PU/TRIS, (d) PU/CR and (e) PU/MBCD..... 44
Figure 30. Stress-strain curves obtained for the pure polyurethane and polyurethane-based membranes: (a) PU, (b) PU-s, (c) PU/TRIS, (d) PU/CR and (e) PU/MBCD. Multiple specimens are shown for each composition..... 45
Figure 31. Average Young's moduli (E) and respective standard deviations for the pure polyurethane and polyurethane-based membranes..... 46
Figure 32. Average tensile strengths and respective standard deviations for the pure polyurethane and polyurethane-based membranes..... 47
Figure 33. Average elongations at break and respective standard deviations for the pure polyurethane and polyurethane-based membranes..... 47
Figure 34. Permeate pressure ($p_p$) vs. time (t) of $CO_2$ and $O_2$ gases ($p_f$=3 bar) for the pure polyurethane membranes: a) PU and b) PU-s..... 49
Figure 35. Permeate pressure ($p_p$) vs. time (t) of $CO_2$ and $O_2$ gases (at $p_f$=3 bar) for the polyurethane-based membranes: a) PU/TRIS, b) PU/CR, and c) PU/MBCD..... 50
Figure 36. Permeate pressure ($p_p$) vs. time (t) of $CO_2$ and $O_2$ gases (at $p_f$=3 bar) for the mixed matrix membranes: a) PU/Zn-NH2-BDC, b) PU/Cu-BTC-0.1, c) PU/Cu-BTC-1.0..... 51
Figure 37. $CO_2$ and $O_2$ volumetric fluxes (J) versus the transmembrane pressure (TMP) for the pure polyurethane and polyurethane-based membranes: a) PU, b) PU-s, c) PU/TRIS, d) PU/CR, e) PU/MBCD..... 52

Figure 38. $CO_2$ and $O_2$ volumetric fluxes (J) versus the transmembrane pressure (TMP) for the pure polyurethane and mixed matrix membranes: a) PU, b) PU/Zn-$NH_2$-BDC, c) PU/Cu-BTC-0.1, d) PU/ Cu-BTC-1.0. ..... 53
Figure 39. Average permeability coefficients (P) towards $CO_2$ and $O_2$, and respective standard deviations, for all the studied membranes. ..... 55
Figure 40. Permeate pressure (pp) vs. time (t) of $CO_2$ and $O_2$ gases (pf=3 bar) for the commercial membrane..... 57
Figure 41. $CO_2$ and $O_2$ volumetric fluxes (J) versus the transmembrane pressure (TMP) for the commercial membrane. ..... 57
Figure 42. Average diffusion coefficients (D) towards $CO_2$ and $O_2$, and respective standard deviations for all the studied membranes. ..... 61
Figure 43. Average solubility coefficients (S) towards $CO_2$ and $O_2$, and respective standard deviations for all the studied membranes. ..... 61
Figure 44. Chemical structures of: a) PURE-G1, b) PEI and c) TREN. ..... 71
Figure 45. Photographs of the precipitates that formed inside the casting solutions for: a) PU/PURE-G1, b) PU/PEI and c) PU/TREN. ..... 72
Figure 46. Chemical structure of tannic acid..... 72

# List of Abbreviations

6FDA – (Hexafluoroispropylidene) diphthalic anhydride
ATR-FTIR – Attenuated Total Reflectance - Fourier Transform Infrared
BPA – Bisphenol A
BSE – Back-Scattered Electron
CA – Cellulose Acetate
CMS – Carbon Molecular Sieve
CPB – Cardiopulmonary bypass
CR – Congo Red
DEE – Diethyl ether
DMF – Dimethylformamide
ECLS – Extracorporeal Life Support
ECMO – Extracorporeal Membrane Oxygenation
EDS – Energy-Dispersive X-Ray Spectroscopy
HS – Hard Segment
MBCD – Methyl-Beta-Cyclodextrin
MBO – Membrane blood oxygenators
MMM – Mixed Matrix Membrane
MOF – Metal Organic Framework
PBDO – Poly(butadienediol)
PBI – Polybenzimidazole
PC – Polycarbonate
PCL – Poly(caprolactone)
PDMS – Poly(dimethylsiloxane)
PE – Polyethylene
PEG – Polyethylene glycol
PEI – Polyethylenimine
PES – Polyether sulfone
PfT – Feed pressure sensor
PI – Polyimide
PMDA – Pyromellitic dianhydride
PMMA – Poly(methyl methacrylate)
PMP – Polymethylpentene
PP – Polypropylene
PPO – Poly(propylene oxide)
PpT – Permeate pressure transmitter
PRV – Pressure reducing valve
PSF – Polysulfone

PU – Polyurethane

PURE-G1 – First generation polyurea dendrimer

PUU – Poly(urethane urea)

PVA – Polyvinyl Acetate

PVDF – Polyvinylidene fluoride

SEM – Scanning Electron Microscopy

SS – Soft segment

STP – Standard conditions for temperature and pressure

TA – Tannic acid

TMP – Transmembrane pressure

TREN – Tris(2-aminoethyl)amine

TRIS – Tris(hydroxymethyl)aminomethane

UTS – Ultimate Tensile Strength

VA ECMO – Venoarterial Extracorporeal Membrane Oxygenation

VV ECMO – Venovenous Extracorporeal Membrane Oxygenation

ZIF – Zeolitic-Imidazolate Frameworks

# List of Symbols

$A$ – Effective membrane area

$\alpha$ – Selectivity

$C$ – Concentration

$D$ – Diffusion coefficient

E – Young's modulus

$J$ – Volumetric flux

$\ell$ – Membrane thickness

$n$ – Number of moles

$P$ – Permeability coefficient

$P_{CO2}$ – Permeability coefficient for $CO_2$

$P_{O2}$ – Permeability coefficient for $O_2$

$p$ – Pressure

$p_{CO2}$ – Partial pressure of $CO_2$

$p_{O2}$ – Partial pressure of $O_2$

$p_p$ – Permeate pressure

$p_f$ – Feed pressure

$p_{STP}$ – Pressure at STP conditions

$Perm$ – Permeance

$V$ – Volume

$V_s$ – Volume of the receiving chamber

$R$ – Ideal gas constant

$S$ – Solubility coefficient

$\sigma$ – Standard deviation

$T$ – Temperature

$T_{STP}$ – Temperature at STP conditions

$t$ – Time

$t_{lag}$ – Time lag

# 1. Introduction

The human circulatory system is divided into two subsets: the cardiovascular system, composed of the heart and blood vessels, and the lymphatic system, consisting of the lymphatic vessels and lymphoid tissues. There are an estimated 100,000 kilometers of blood vessels in the circulatory system of an average adult, forming a closed and pressurized system, through which approximately 5.5 liters of blood flow continuously. Blood circulation serves a multitude of functions: transportation of respiratory gases, nutritive molecules and metabolic waste, regulation of temperature and hormones, and protection, through processes such as clotting and immune responses.

The cardiovascular system is closely intertwined with the respiratory system. The blood that has become partially depleted of oxygen ($O_2$) and enriched in carbon dioxide ($CO_2$) through metabolic activity is returned to the right atrium of the heart. The heart pumps the oxygen-poor blood through the pulmonary arteries to the lungs, where a gas exchange occurs. The $O_2$ from the air in the lungs diffuses to the blood, while $CO_2$ diffuses in the opposite direction. The blood then becomes enriched in $O_2$ and partially depleted of $CO_2$ and is returned, through the pulmonary veins, to the left atrium of the heart. Finally, the heart pumps the oxygen-rich blood to a very large artery called the aorta, which in turn supplies blood to the rest of the body. The flow of blood from the right ventricle of the heart, through the lungs, and back to the left atrium of the heart is called pulmonary circulation, while the flow of blood from the left ventricle of the heart, through the organ systems, and back to the right atrium of the heart, is called the systemic circulation. The average cardiac output (volume of blood pumped by the heart) in an adult is 5.5 liters per minute, meaning that it takes about one minute for a drop of blood to complete the systemic and pulmonary circuits.

The respiratory system is composed of the lungs and the airways: nose, mouth, pharynx, larynx, trachea, primary bronchi and bronchioles. The main function of the lungs is to establish a gaseous equilibrium between the blood and the air. It does so by enriching the blood that goes into systemic circulation in $O_2$, which is necessary in the production of energy that keeps the body running, and ridding it of $CO_2$, which is a waste molecule that must be removed in order to maintain a stable blood pH. During respiration, the airways serve a multitude of additional functions besides the exchange of gasses, such as warming and humidifying of the inspired air, as well as filtration and cleaning.

The gas exchange that occurs during pulmonary circulation takes place in tiny air sacs at the end of the bronchioles called alveoli. The lungs contain an estimated 300 million alveoli, providing a vast surface area of 60 to 80 square meters. Moreover, each alveolus is surrounded by a big number of blood capillaries. The thickness of alveolar cells and capillary cells averages 0.15 mm each, resulting in an exceedingly small air-blood distance of approximately 0.3 mm. Because of the large alveolar surface area and thin air-blood barrier, the diffusion of gases across lung tissues occurs very rapidly and efficiently. Blood that is delivered to the lungs from the systemic circulation usually has partial pressures of oxygen ($p_{O2}$) and carbon dioxide ($p_{CO2}$) of 40mmHg and 46 mmHg respectively. The blood that is returned to the heart after the gas exchange in the lungs, has an increased $p_{O2}$ of about 100 mmHg and a decreased $p_{CO2}$ of 40 mmHg.

Despite being thin, alveolar walls exhibit great tensile strength provided by the strong fusion to the basement membranes of the blood capillaries. Consequently, alveolar walls are capable of withstanding the high stresses experienced during high lung inflation and heavy exercise [1].

## 1.1. Cardiopulmonary bypass

The top ten global leading causes of death are associated with either cardiovascular, respiratory or neonatal conditions, according to the World Health Organization [2].Patients with lung and/or cardiac failure are often cared for using blood oxygenation devices, also known as artificial lungs, which provide temporary partial or full support to the patient's lungs. Blood oxygenators are used for cardiopulmonary bypass (CPB) during heart surgery, providing surgeons with an operating environment free of blood and motion. They are also used in longer-term therapies such as extracorporeal life support (ECLS), giving the patient the necessary time for recovery. During the recent influenza A(H1N1) and COVID-19 pandemics, ECLS gained renewed attention in the treatment of patients with severe symptoms such as viral pneumonia, which can lead to respiratory failure and death [3], [4].

After decades of trial and error, the first successful cardiopulmonary bypass operation was performed in 1953, using a heart-lung machine designed by J. Gibbons Jr. [5] Over the years, three types of oxygenators have been developed and used: film-type oxygenator, bubble-type oxygenator, and membrane-type oxygenator.

In film oxygenators, the gas exchange occurs by direct contact with the surface of a thin blood film. This type of device requires large surface areas, and thus, high priming volumes of blood (volume needed to fill the entire device, eliminating any air in the system). In bubble oxygenators, gas bubbles are introduced directly into the blood. The high surface area of the gas bubbles ensures that oxygenation is effective, making this type of device simple and inexpensive. However, this oxygenator poses the highest risk of trauma due to the mechanical stresses caused by bubbling gas directly into the blood. Furthermore, in order to avoid complications, the complete removal of bubbles from the blood must be ensured. Lastly, in membrane oxygenators (flat sheet or hollow-fiber), the blood is exposed to oxygen through a gas-permeable membrane. The contact between the blood and the gas is indirect in this case, lowering the risk of trauma. However, because the membrane offers resistance to the permeation of gases, the gas transfer rate may be low, in which case the surface area and priming volume of blood must be maximized. Membrane oxygenators are the only ones used today [5], [6].

Nowadays, the guiding principle used in the design of blood oxygenators is to mimic the structure of the natural lung. The ideal oxygenator should therefore be able to obey the following requirements:

- oxygenation of venous blood at up to 5L/min,
- removal of $CO_2$ at a rate that ensures a stable blood pH, preventing both acidosis and alkalosis,
- use of reasonable priming volumes of blood, ranging from 1 to 4L,
- hemocompatibility (reduced risk of trauma to the blood by avoiding hemolysis, protein denaturation, platelet adhesion and activation, etc.),

- safety and ease of use [7].

## 1.2. Membrane blood oxygenators

Membrane blood oxygenators (MBOs) were an important breakthrough in the evolution of blood oxygenation devices. Because the contact between the air and blood happens indirectly (through a membrane), removal of gas bubbles from the blood stream is not necessary, which greatly diminishes the risk of air embolism.

Figure 1 illustrates the working principle behind an MBO. In this system, the gas exchange is driven by the concentration gradients of $O_2$ and $CO_2$ across the membrane, which acts as a selective barrier between the blood and the air. The oxygenator must supply approximately 250 $cm^3$ (STP)/min of $O_2$ and simultaneously remove about 200 $cm^3$ (STP)/min of $CO_2$. High blood flow rates of 2-4L/min are required because of the limited solubility of these gases in the blood. Nonetheless, $CO_2$ presents better solubility and diffusion properties than $O_2$, making the removal of $CO_2$ more efficient than the addition of $O_2$.

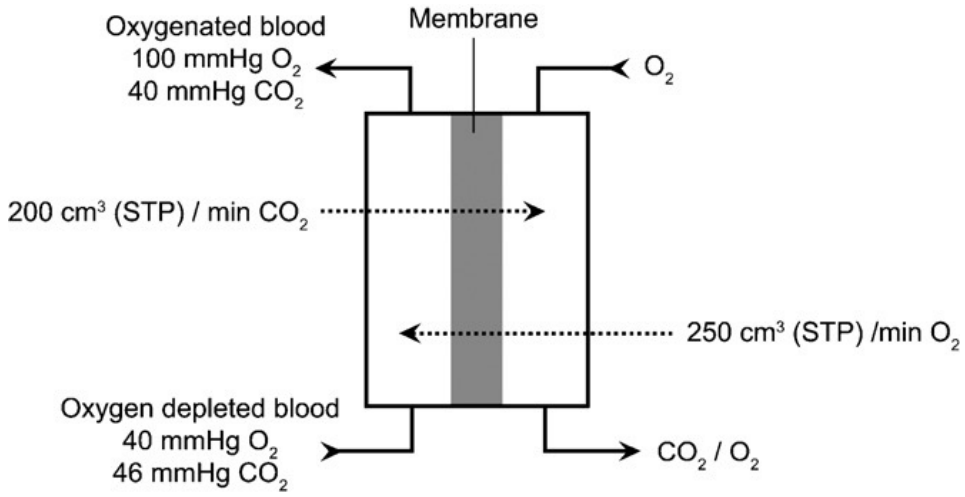


Figure 1. Principle of membrane blood oxygenation [7].

The presence of a membrane at the blood/gas interface poses resistance to mass transfer and therefore its properties in terms of gas permeability (gas solubility and diffusion) must be tailored to reduce the resistance offered by the additional barrier. In the recent past, substantial efforts have been directed towards the development of membrane materials with an optimized compromise between hemocompatibility and gas permeation properties [7].

## 1.3. Extracorporeal membrane oxygenation

Extracorporeal membrane oxygenation (ECMO) is a modified form of cardiopulmonary bypass that was first developed in the 1970s. In recent years, ECMO has undergone substantial technical improvements concerning pumps and oxygenators, as well as improved hemocompatibility. This therapy is used in intensive care units, as a bridge-to-transplant support for cardiac and lung transplants as well as lung resections. The latest generation ECMO systems are much simpler and can be managed entirely by one specialized nurse. However, although nowadays it is possible to keep patients on ECMO for weeks or even months, it is still considered a high risk procedure since the oxygenator has to be changed every couple of days [3], [8]. More efficient membranes could allow the oxygenators to be used for longer periods of time before being swapped.

Figure 2 shows a schematic representation of an ECMO circuit. Generally, thin tubes called cannulae are inserted into large blood vessels leading directly to the heart, allowing the blood to be drained and pumped through the ECMO circuit. Circulation is facilitated by an external centrifugal pump that pushes the blood into contact with the membrane where the gas exchange takes place. After oxygenation and removal of $CO_2$, the blood is warmed using a circulating water bath at body temperature and heat exchanger. Finally, the blood is returned to the heart [3], [6].

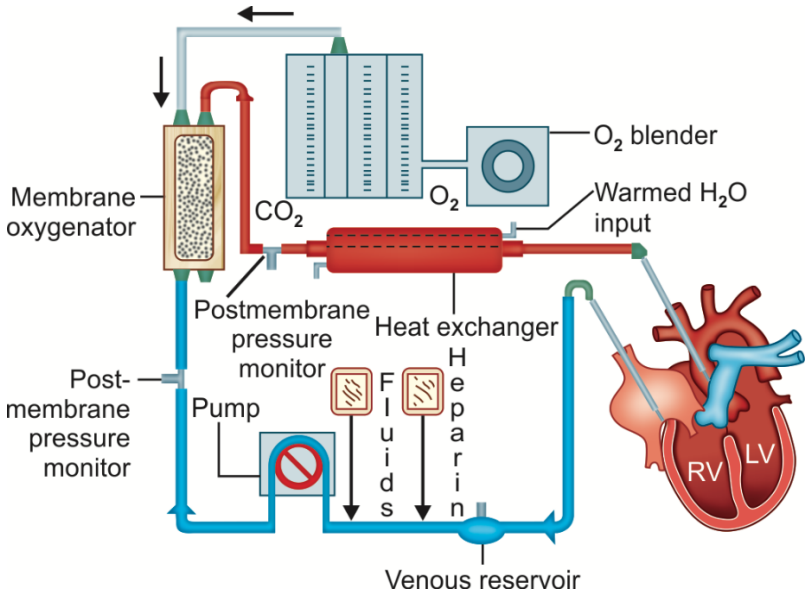


Figure 2. Schematic representation of an ECMO System [6].

There are two types of ECMO: venoarterial (VA) ECMO and venovenous (VV) ECMO. Normally, the patient's age, size, weight and motive for ECMO will dictate the size and placement of the cannulae, consequently determining which type of ECMO is most appropriate [6].

VA ECMO (Figure 3.a) can provide both respiratory and hemodynamic (circulatory) support and is, therefore, fit for patients with both lung and heart failure. Blood is drained from the right atrium

of the heart by inserting the cannula via the femoral vein. It is then pumped through the oxygenator, warmed up, returned to the heart via the femoral artery.

VV ECMO (Figure 3.b) only provides respiratory support, so the patient must present a stable heart. Blood is drained from one or both vena cavae (using one or two cannulae respectively) through the jugular or femoral veins. It is then oxygenated and returned to the right atrium of the heart [3].

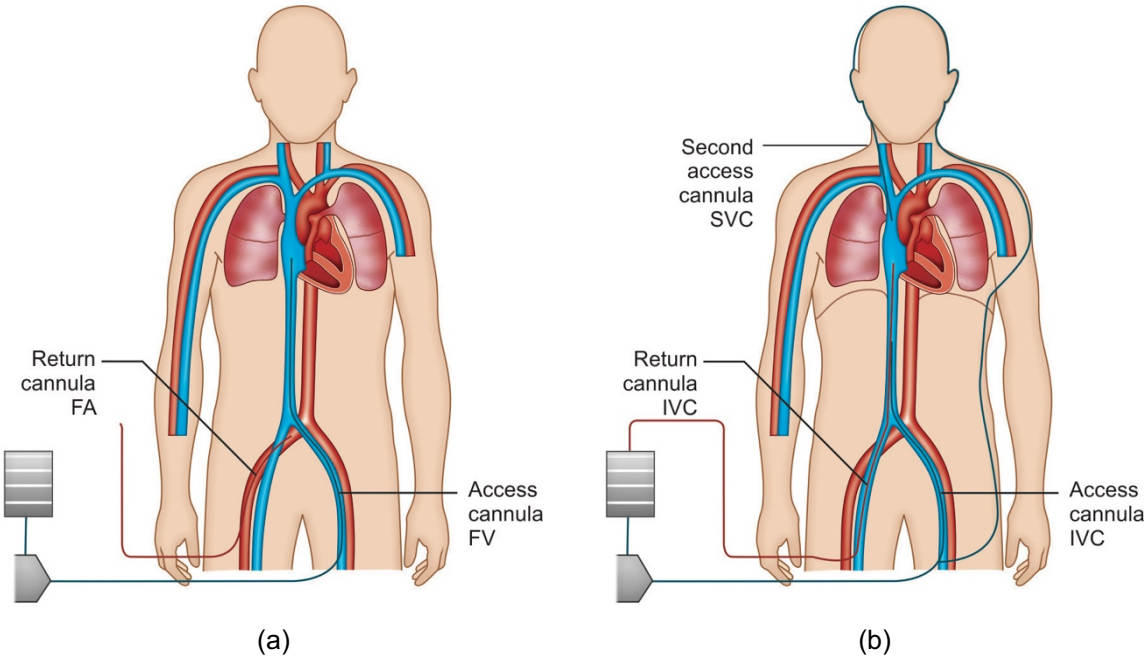


Figure 3. Schematic representation of: a) VA ECMO, b) VV ECMO. FA is the femoral artery, FV the femoral vein, SVC the superior vena cava and IVC the inferior vena cava [6].

The biggest advantage of VA over VV ECMO is the complete respiratory and hemodynamic support it delivers. However, VA ECMO is linked to greater risk of complications than VV ECMO, including maldistribution of oxygen, increased tension in the left ventricular wall, systemic thromboembolism, limb ischemia, and various neurological complications [3]. VV ECMO minimizes the potential for arterial injuries since blood is withdrawn and returned to the same side of circulation. VV ECMO also has the possibility of being performed by inserting one single cannula (called a double lumen cannula) into the jugular vein, which is more appropriate for smaller patients.

The biggest risk associated with any type of ECMO is bleeding (from where the cannulae is placed or from older puncture wounds). This is due to the use of anticoagulants (blood thinning medication), such as heparin, administered to patients in order to avoid the formation of clots inside the circuit. If clots or air bubbles make their way out of the circuit and into the patient's body, they can lead to the obstruction of important blood vessels and result in death. Additionally, an oxygenator is essentially a large intravascular foreign body that can trigger a series of septic complications. ECMO complications are more frequent in adults than in children, except for neurological complications (such as seizures, infarction and intracranial hemorrhage) which are most common among neonates. Typically, the team operating the ECMO system is specially trained to manage these risks and deal with any accompanying medical emergencies [6], [8].

## 1.4. Membranes for gas permeation processes

Membrane gas separation was developed as a cost-effective, energy efficient and ecological alternative to the traditional gas separation methods used in various industries, such as cryogenic distillation and adsorption processes [9], [10].

The first industrial membrane gas separation system was built by Monsanto in 1980 for the separation of hydrogen from the purge gas (composed of nitrogen, argon and methane) of ammonia synthesis plants. Since then, this technology has become a commercially viable and competitive solution in a wide range of applications. The two most important applications of gas permeation membranes, representing over 60% of the total market, are for the production of nitrogen ($N_2$) from air and the removal of $CO_2$ from natural gas. Other major applications include the hydrogen ($H_2$) recovery in refinery hydrotreaters, the adjustment of hydrogen/carbon monoxide ($H_2$/CO) ratio in syngas plants, and the separation of light hydrocarbons from purge gas in polyolefin plant resin degassing. Additionally, there are various emerging applications in the early stages of commercialization: $O_2$ production from air, olefin/parafin separation (in ethylene/ethane and propylene/propane mixtures for example), $H_2/CO_2$ separation in refineries, and finally, carbon capture ($CO_2/N_2$ separation) and its sequestration underground to reduce carbon emissions in electric power plants and other industrial processes [11].

Gas permeation membranes are also used in medical applications such as the case of MBOs which will be reviewed in more detail in section 1.5.

Membrane gas separation shows great promise and there are numerous opportunities for its expansion to new markets. In fact, membranes are expected to play a significant part in reducing the costs and environmental impact (both in terms of energy utilization and waste generation) of a range of industrial processes. However, further research and product development are needed in order to optimize this technology to meet the requirements of each specific potential application. Therefore, a number of factors come into play when designing membranes tailored for the separation of a particular gas-mixture:

- the properties of the membrane material (permeability, selectivity, long-term stability)
- the membrane structure and thickness
- the membrane configuration (flat sheet / hollow fiber)
- the membrane fabrication technique
- the gas separation system it will incorporate [10].

Today, most research is aimed at generating new membrane materials and structures with improved permeability (the rate at which a compound permeates through the membrane) and selectivity (the ability of a membrane to accomplish a specific separation), which in turn yields with higher product purity and recovery rate. Despite the investigation of hundreds of materials, over 90% of commercial membranes in use today are manufactured from fewer than ten materials, all of which are polymeric in nature [10], [11].

Most of the organic polymers investigated for gas separation membranes exhibit a trade-off behaviour between selectivity and permeability. In fact, polymers presenting with high selectivity usually have low permeability and vice versa. The development of novel polymeric materials capable of

overcoming this trade off, by exhibiting both high selectivity and permeability, has recently been the focus of a large number of studies [9], [12].

However, the gas permeation properties of polymeric membranes are known to deteriorate over time due to plasticization or physical ageing at specific feed conditions. Additionally, the temperature range at which polymeric materials are stable is significantly lower than the operating temperatures required for numerous industrial processes [12]. These drawbacks prompted the development of an alternative type of membranes made from inorganic materials, including metals (palladium, silver, etc.), oxides (alumina, titania, zirconia), zeolites, glass (silica) and carbon (graphene, nanotubes, molecular sieves) [13]. Inorganic membranes exhibit a number of advantages over polymeric membranes in terms of thermal and chemical stability and reduced plasticization, as well as controlled porosity (pore size and distribution), which in turn allows for better control of the permeability and selectivity. On the other hand, inorganic materials generally exhibit brittleness, low reproducibility and high costs, which greatly reduces their viability for commercial applications [10].

Overall, the progress that has been made in designing membrane materials with enhanced permeation characteristics has been relatively slow. The challenges encountered in polymer materials, namely the selectivity-permeability trade-off, have been addressed with varying degrees of success in advanced materials. Besides pure polymers, other categories of materials which have been widely studied in terms of potential for gas separation include copolymers, polymer blends and mixed-matrix materials.

### 1.4.1. Pure polymer membranes

Polymers used in membranes can be classified as rubbery or glassy, depending on whether they operate above or below the polymer glass transition temperature (Tg), respectively. Some examples of rubbery polymers are silicone rubber, neoprene, polyether, polyvinylchloride, polyurethane, and polybutadiene. Glassy polymers include cellulose acetate, perfluoropolymers, functionalized polyacetylenes, polycarbonates, polyimides, poly(phenylene oxide), and polysulfones [13].

Silicone rubbers are elastomers, and are generally inert (due to strong silicon-oxygen bonds), inexpensive, readily available, and chemically and thermally stable at temperatures ranging between −55 °C and 300 °C. In contrast, they tend to have very low tensile and fatigue strengths. One example commonly used in membranes is polydimethylsiloxane (PDMS), which exhibits high permeability but low selectivity. Occasionally, fillers are added to reduce costs and improve properties. Over the years, silicone rubber membranes have been used for olefin separation, removal of organic vapors from air, and pervaporation of multiple organic species [12].

Cellulose acetate (CA) membranes originated in reverse osmosis applications and were some of the first to be commercialized in the mid 1980s, currently representing 80% of the membrane market for the separation of natural gas [13]. Besides its abundance, renewability and low costs, CA exhibits good transport properties and allows for reduced membrane surface areas, and thus, for high recovery efficiency. One limitation of CA membranes is its plasticization in the presence of $CO_2$, which results in

decreased selectivity for carbon dioxide/methane ($CO_2/CH_4$) in mixed gas environments, and thus, reduces methane recovery from natural gas [14], [15].

Another type of material common in polymer membranes are polycarbonates (PCs). These thermoplastics have good mechanical properties and high stability under extreme temperature and pressure conditions but are not suitable for all applications due to the low gas permeability and solubility they exhibit for certain gas mixtures. One example of a commercial PC is bisphenol A (BPA) and its variants, such a tetra-bromo BPA which has been shown to increase the $O_2/N_2$ selectivity, making it a good candidate for air separation [12], [14].

Polyimides (PI) membranes have gained attention because of their excellent physiochemical properties: stability at high temperatures, low thermal expansion coefficient, dimensional stability, high mechanical strength, good radiation and chemical resistance [12]. They are seen as an alternative to cellulose acetate because of their good film-forming properties, and have also demonstrated higher selectivity and permeability than other membrane materials, such as polysulfones and polycarbonates. However, PIs are even more sensitive to plasticization than cellulose acetate. Some notable examples used in gas separation are a commercial PI named Matrimid®, and PIs based on hexafluoroispropylidene diphthalic anhydride (6FDA) and pyromellitic dianhydride (PMDA) [13]. The applications of PI membranes in gas separation include the $N_2$ separation from air, $H_2$ separation from synthesis gas, $CO_2/CH_4$ separation in natural and biogas, $CO_2$ capture, ammonia plants and olefin/paraffin separation [14].

One last important family of polymers used in gas separation membranes includes polysulfones (PSFs) and polyether sulfones (PESs). PSF and PES offer an ample range of advantageous properties: thermal and chemical stabilities, mechanical strength, rigidity, creep resistance, high critical pressure of plasticization, good permeability and selectivity, low-cost and simple manufacturing. Consequently, polysulfone membranes have been widely used for $H_2$ recovery, air separation, and $CO_2/CH_4$ separation in natural gas. PSFs show lower $CO_2$ permeability and $CO_2/CH_4$ selectivity than CA, but higher plasticization pressure. However, transport properties of PSFs can be enhanced by functionalization, for example, with bromine or butyllithium [12], [14].

### 1.4.2. Copolymer and polymer blend membranes

In addition to pure polymer membranes, which are constituted of one single type of monomer, other groups of polymeric membranes widely found in literature are copolymer and polymer blend membranes. By combining the advantages of multiple homopolymers, these membranes offer an inexpensive path to the enhancement of gas permeation characteristics and other properties such as: processability, heat distortion, impact resistance and fatigue behavior [12].

A copolymer, or heteropolymer, is constituted by two or more types of monomers linked together in the same polymer chain. Copolymers can be classified based on the arrangement of its structural units along the chain, into the following categories: statistical (or random) copolymers, periodic copolymers, alternating copolymers, block copolymers, and graft copolymers. Copolymers can also be linear, involving one single main chain, or branched, consisting in a single main chain with one or more polymeric side chains [12].

Polymer blends, on the other hand, are obtained from a physical mixture of two or more polymers through mechanical mixing [16]. The successful property enhancement of a polymer blend is contingent upon the miscibility or compatibility of the two homopolymers [12]. When blends are miscible, both polymers are dissolved together at molecular levels, constituting one homogenous single-phase. In phase-separated blends (such as immiscible or partially miscible blends), the two polymers do not dissolve, and they form two phases divided by an interface. Partially miscible blends have been expansively used in gas separation applications and their performance varies with membrane morphology, specific volume fractions, and the size and shape of each phase [17].

There are countless applications of polymer blends used in gas separation membranes. Some examples, among many others, are polyethylene glycol (PEG) blends (containing CA or a polyether block amide named Pebax®) used in $CO_2$ separation, polyimide blends (involving PSF and PES, and polybenzimidazole (PBI)) for $H_2$ recovery, $O_2/N_2$ and $CO_2/CH_4$ separations, and polyurethane blends (with poly(methyl methacrylate) (PMMA), polyetherimide (PEI), PU/poly(amide-imide) (PAI), and polyvinyl acetate (PVA)) for the transport of $H_2$, $N_2$, $O_2$, $CH_4$, and $CO_2$ gases. Polyurethane-based membranes will be further discussed in the next sections, in the context of membrane blood oxygenation [12], [17].

### 1.4.3. Mixed matrix membranes

Although polymeric membranes have economic and processing advantages, their gas separation performance is limited. On the other hand, inorganic membranes show great gas transport properties and better thermal and chemical stabilities, but as of today, their large-scale manufacturing is prohibitively expensive. A new group of hybrid composite membranes, denominated by mixed matrix membranes (MMMs), was introduced as a means of overcoming the aforementioned limitations of polymer and inorganic materials. MMMs are composed of nano or micro-sized inorganic fillers (also known as molecular sieve materials), homogenously dispersed in a continuous polymer matrix. These membranes combine the higher permeability and selectivity of the inorganic phase, with the low cost and processability of the polymeric phase [13], [14].

The selection of the proper combination of filler and matrix materials and their compatibility is decisive for the morphology and separation performance of MMMs in specific applications. Although glassy polymers are preferred because of their rigid structure and superior gas selectivity (as opposed to rubbery polymers which tend to be highly permeable but poorly selective), they generally present with poor adhesion to the surface of the filler particles, causing voids to form in the organic-inorganic interface [18]. Furthermore, the performance of MMMs is greatly influenced by the nature of the fillers used, as these can affect the crystallinity and packing of polymer chains, and potentially generate new diffusional paths and different interactions between the membrane and the permeating molecules. Fillers can either be porous, in which case they act as molecular sieves that separate gas molecules based on shape and size, or nonporous, which can disrupt the polymer chain packing in the matrix [14]. The most important porous fillers in use are zeolites, metal organic frameworks (MOFs), and carbon molecular sieves (CMSs). Common nonporous fillers include silica and various metal oxides, such as $TiO_2$ [18]. Depending on the type of inorganic filler added, the gas transport properties of the polymeric

membranes are improved through a combination of the following factors: molecular sieving effect, increased polymer chain rigidity, higher membrane free-volume, and enhanced membrane-penetrant interactions [13].

Zeolites are a class of aluminosilicate minerals with highly porous microstructures and excellent thermal and chemical stability [19]. Reported attempts at incorporating zeolites in MMMs include: silicalite/CA in $CO_2/H_2$ separation, zeolite 5A/silicone rubber for enhancement of diffusion time lag, and zeolite 4A/PES or zeolite 13X/PES in $CO_2/N_2$ separation [14], [15]. Metal organic frameworks (MOFs) are highly porous, three-dimensional nanostructures composed of metal centers and organic linkers joined by coordination bonds. The organic linkers in MOFs interact with the polymer matrix providing better filler/matrix contact than with zeolites. Other benefits of MOFs are its high porosity with customizable pore size and shape, high surface area to volume ratio, ease of functionalization, and adjustable affinity towards the gas of interest. There are hundreds of examples of MMM's containing MOFs for gas separation, such as the copper-based Cu-MOFs, chromium-based MIL-101 and zirconia-based UiO-66 MOF series, to name a few. The use of zeolitic-imidazolate frameworks (ZIFs), like ZIF-8 and ZIF 67 in a polyimide matrix (6FDA), has also been reported for the separation of propene/propane ($C_3H_6/C_3H_8$) [13]. Finally, CMSs are porous carbon structures, frequently used as fillers in MMMs, containing apertures of approximately the same dimensions as the diffusing gas molecules. Consequently, they separate gases based on differences in kinetic diameters. CSMs have been used in industry to remove carbon dioxide from landfill gases and separate air by adsorption of oxygen. Other porous carbon-based fillers extensively used in literature are carbon nanotubes and activated carbon [18].

Mixed matrix membranes have not yet been widely investigated for application in blood oxygenators, but some encouraging results have been found for other applications in terms of $CO_2$ and $O_2$ permeation. Recently, a variety of polyurethane-based MMMs have been developed for the separation of $CO_2$ using different fillers, such as: carbon nanotubes coupled with titanium oxide [20], gamma-cyclodextrin MOF [21], functionalized nanodiamonds [22] and nickel oxide nanoparticles [23]. Polyurethane-zeolite MMMs, using 3A, 4A and ZSM-5, were also investigated, and presented improved permeabilities for $CO_2$, $CH_4$, $N_2$ and $O_2$ gases [24].

All in all, MMMs show great potential for gas separation but their large-scale application presents several challenges that need to be addressed. Instead of the micro-sized fillers currently used in MMMs, it would be ideal to incorporate nano-sized fillers which increase the polymer/filler interfacial are, while simultaneously forming thinner membranes with improved transport properties. Another common challenge is avoiding the improper dispersion of the fillers which can lead to their agglomeration [14].

### 1.4.4. Membrane structure and synthesis

The membrane preparation method has a great effect on features like thickness, porosity and homo or heterogeneity, which in turn, play an important role in the membrane's transport properties, like permeability and selectivity. Therefore, the commercial value of a membrane is significantly influenced by its fabrication method and resulting configuration. There are numerous techniques for

membrane production including melt-pressing, solution casting, phase inversion, interfacial polymerization, sputtering and extruding. Generally, two types of membrane geometry can be obtained: flat sheet (used in disc, spiral wound, plate, and frame modules) and cylindrical (used in tubular, capillary and hollow-fiber modules) [12].

In laboratories, two methods are commonly used for the fabrication of polymeric membranes: phase inversion technique and precipitation by solvent evaporation. In the phase inversion technique, the polymer is first dissolved in a mixture of two solvents, one volatile and another less volatile, and the solution is cast onto an adequate support using a casting knife, forming a flat sheet. This film is exposed to air for a brief period of time to evaporate the volatile solvent at the surface, and then submerged in a coagulation bath of non-solvent (generally water) where the less volatile solvent exchanges with the non-solvent. Consequently, the polymer becomes enriched in the non-solvent and precipitates, producing a porous membrane with a thin, dense top layer (or skin), known as an asymmetric membrane. The main drawback of this technique is the frequent formation of pinholes [14].

In evaporation casting (or dry casting), the polymer is dissolved in a suitable solvent (or mix of solvents) and the solution is spread on a support using a casting knife. The solvent in the film is left to evaporate in a controlled atmosphere, inducing the precipitation of the polymer. Because the precipitation process in this case is much slower than in immersion casting, the obtained membranes are generally isotropic and less porous. This type of membrane is usually termed symmetric or dense [25].

In either technique, the final membrane structure strongly influenced by the synthesis conditions. Therefore, it is important to control parameters like the composition of the casting solution, viscosity and volatility of the solvents, composition and temperature of the coagulant bath, and finally, evaporation time, temperature and atmosphere.

## 1.5. Membranes for membrane blood oxygenators

Despite a long history of extensive use and continuous development, MBOs still need improvement in various aspects, such as the conditions for blood circulation, equipment design and membrane/blood interactions. The progress in the performance of MBOs is therefore closely tied to the development of novel gas exchange membranes [26].

The semipermeable membranes used in oxygenators are where the gas exchange normally carried out in the lungs occurs, ensuring adequate oxygenation and depletion of carbon dioxide of the blood. The two principal requirements these membranes must fulfill are:

(i) Hemocompatibility,

(ii) Suitable gas permeation properties, ensuring the delivery of approximately 250 $cm^3$ (STP)/min of $O_2$ and removal of 200 $cm^3$ (STP)/min of $CO_2$, at blood flow rates of 2–4 L/min [7].

Recent research has thus focused expressly on the development of materials compatible with blood, as well on the improvement of the flow management and mass transfer properties of the system. Over the last decades, membranes have been produced in a multitude of different polymers and

configurations. The pursuit of increasingly efficient gas exchange membranes, which consequently require smaller membrane areas, lower priming volumes and lower blood flows, could lead to a new generation of smaller, more practical MBO systems.

The first MBOs were composed of silicone rubber, which exhibits very high $O_2$ and $CO_2$ permeation rates and reasonable hemocompatibility. In an attempt to enhance the blood/membrane interactions other materials such as polypropylene (PP), polymethylpentene (PMP), polyethylene (PE), polyvinylidene fluoride (PVDF) were investigated to produce gas permeation membranes [27]. All these polymers are synthesized from one or two monomers, resulting in simple chemical structures like homopolymers or copolymers [7], [26].

Nonetheless, these materials do not exhibit permeation rates as high as silicone rubber and continue to be associated to complications such as plasma leakage, bleeding, myocardial and brain infarction caused by thrombus formation and abnormal pressure gradients generated by fibrin deposits – all of which arise from insufficient hemocompatibility of the membranes [28], [29]. It is widely accepted that the performance of polymers in blood-contacting biomedical devices is closely related to their surface topography and nature since that is where blood-polymer interactions occur. These surface interactions trigger a chain a of events involving the adsorption of proteins, activation of platelets, blood coagulation and complement activation. Strategies to overcome the low hemocompatibility have included a variety of chemical or surface modifications, such as inorganic and heparin coatings. However, coatings are limited in that they have shown to experience delamination when under shear stress from blood flow.

An alternative material showing great potential is polyurethane (PU), with distinguished characteristics such as high bio- and hemocompatibility, as well as good fatigue resistance, tear resistance and mechanical strength [30], [31]. This makes PU suitable for a wide variety of biomedical applications including medical implants, membranes, coatings and adhesives [32].

Polyurethanes are block copolymers, typically exhibiting two phases: hard segment (HS) enriched domains, comprising urethane/urea groups and low molecular weight chain extenders (isocyanates), dispersed in a soft segment (SS) matrix, made up of long flexible polyol chains (like polyester or polyether). The soft, amorphous segments provide thermoplastic elastomeric character, while the hard, crystalline segments increase mechanical strength. Since the polymer chains are mobile, they can rearrange under interfacial forces and consequently, the composition of the surface layers may be different from the bulk. Parameters like the type, length and molecular weight of the segments, hard-to-soft segment ratio and surface functionalization can be finetuned during synthesis in order to obtain tailored bulk properties, such as bio/blood compatibility and mass transfer properties [33], [34].

Additionally, a second type of SS can be introduced into the structure of polyurethane membranes, further increasing its versatility. The presence of a new chemical moiety can generate phase segregation between the HS's and SS's, which can be accompanied by different degrees of phase separation between the two SS's [35]. Several bi-soft segment poly(urethane urea) (PUU) membranes have been studied for membrane oxygenator applications, each containing first SS's made of poly(propylene oxide) (PPO), and varying second SS's, such as poly(butadienediol) (PBDO), poly(dimethylsiloxane) (PDMS) and polycaprolactone (PCL) [33].

### 1.5.1. PU/PBDO membranes

Poly(butadiene diol) (PBDO) was first used as the second SS in bi-soft segment PU membranes for pervaporation, as a means of tailoring permeation selectivity and fluxes [35], [36]. In studies by Queiroz and De Pinho [37], [38], different ratios of poly(propylene oxide) (PPO) and polybutadiene were used in order to investigate the effect of phase separation and degree of cross-linking on the gas permeability of the membranes. They found that membranes containing 20wt% PBDO exhibited phase separation between the two SS's, and high $CO_2$ permeability of 150-950 Barrer. However, no phase segregation was observed between the two SS's of the membranes containing 67wt% PBDO, which presented with lower $CO_2$ permeability of 90-550 Barrer. Consequently, it was determined that increasing the PBDO content in the membrane promoted higher degrees of mixing between the microphases and less urethane/urea aggregation, in turn leading to lower $CO_2$ permeabilities.

### 1.5.2. PU/PDMS membranes

Poly(dimethylsiloxane) (PDMS) polymers possess a unique set of properties which makes them suitable for a wide range of applications. These properties are due in part to the nature of the siloxane bonds, and include high thermal stability, low glass-transition temperature, low surface energy, and high permeability to gases. Nevertheless, PDMS performs poorly in terms of mechanical properties. One solution is to add PDMS to PU, thus combining the attributes of both polymers. The obtained material exhibits higher mechanical strength and abrasion resistance than PDMS, as well as lower temperature flexibility and better heat resistance than PU.

In another study by Queiroz and De Pinho [32], novel bi-soft segment PU membranes were synthesized using PDMS as the second SSs. Subsequently, the effect of the membrane's structural characteristics on its gas permeation properties was evaluated. In membranes with PDMS content ranging from 25 to 75%, evidence was discovered of phase separation between the two SSs. The short HSs formed small aggregates and could be found within any of these two phases. The increase in PDMS content was shown to decrease the formation of aggregates. Furthermore, the increase in PDMS fraction from 25 to 75 wt% was also associated with the increase of the CO2 permeability from 200 to 800 Barrer, and of the O2 permeability from 30 to 120 Barrer. The greater permeability of the 75 wt% PDMS membrane was attributed to the higher content of siloxane groups, lower degree of cross-linking and lower formation of urethane/urea aggregates.

### 1.5.3. PU/PCL membranes

Despite having satisfactory gas permeation properties, PU/PBDO and PU/PDMS membranes exhibit poor blood compatibility properties. This led to the introduction of polycaprolactone-diol (PCL-diol) as a second SS because it has shown, through extensive use in vascular tissue engineering, to contribute to the improvement of the blood compatibility, specifically trough the control of platelet adhesion and activation. Characterization studies by Besteiro et al. [34] of nonporous symmetric PU/PCL membranes revealed that multiple factors had an impact on their hemocompatibility:

topography, phase morphology near the membrane surface, degree of hard segment aggregation, surface energy, and PU/PCL weight ratio. Another study by Faria and De Pinho [29] showed a strong correlation between platelet deposition and top surface roughness in asymmetric PU/PCL membranes.

The same group studied the structure and microphase segregation in symmetric PU/PCL membranes (with varying PCL fractions) and their correlation with the $O_2$ and $CO_2$ permeability measurements obtained from a photoacoustic gas detection system. The increase in PCL content was found to increase the formation of HS aggregates dispersed in the SS phase. Moreover, the $CO_2$ permeability of the PU/PCL membranes exhibits a non-monotonous behavior: it increases from 188 to 337 with increasing PCL content between 0 to 10wt% but reaches its lowest value of 113 Barrer for 15wt% PCL. The O2 permeability, varying between 10 and 11 Barrer, did not change significantly with PCL content [33].

Faria et al. further investigated the relationship between the surface characteristics and hemocompatibility by using integrally skinned asymmetric PU/PCL membranes. These membranes are composed of a bottom porous surface with enhanced permeability, and a thin dense top surface (the active layer) which prevents the blood from contacting with the porous surface, in turn avoiding platelet deposition and plasma leakage. Membranes with higher PCL concentrations exhibited smoother and denser top layers, as well as lower platelet adhesion and inhibition of extreme stages of platelet activation [31].

Another study from the same team addressed the effect of casting conditions on the morphological features and permeability properties of integrally skinned asymmetric PU/PCL membranes. They found that the increase in solvent concentration (in this case diethyl ether (DEE)) was accompanied by a decrease of the active layer thickness as well as an increase in the porosity of the sublayer. Moreover, higher DEE concentrations and lowest evaporation times yielded higher permeabilities. The membrane containing 10wt% PCL, which had showed good hemocompatibility in previous research, exhibited a $CO_2$ permeance of $0.27 \times 10^{-5}$ $cm^3/cm^2s.cmHg$, rising above the required $CO_2$ permeance for blood oxygenators. The experimental results obtained for all the membranes support the assumption that the resistance to $CO_2$ permeation lies in a diffusive layer equivalent in thickness to the active layer. In contrast, the $O_2$ permeances remained below the desirable threshold for MBOs, suggesting that additional investigation is needed to optimize the $O_2$ permeation properties of this type of membrane [39].

Lastly, in work by Eusébio et al., a new gas permeation experimental setup was designed to record the evolution of the permeate pressure of a single gas ($N_2$, $O_2$ and $CO_2$) with time, for a given feed pressure. This system allows for the measurement of transient and steady state permeation regimes, and consequently, for the decoupling of the solubility and diffusion contributions to the gas permeance. To validate the new set-up, both nonporous symmetric and integral asymmetric PU/PCL membranes were synthesized, with PCL contents varying from 0 to 15wt%. The permeability coefficients for the nonporous symmetric membranes ranged from 172 to 227 Barrer for $CO_2$, 17 to 24 Barrer for $O_2$ and 7 to 9 Barrer for $N_2$, which were comparable to the values obtained for the current commercial membranes used in MBOs. The gas permeation through PU/PCL membranes was lower for higher PCL contents, and was shown to be controlled by solubility. In the integral asymmetric set of

membranes, lower evaporation times yielded higher permeabilities. However, the asymmetric membranes showed no clear improvement over the symmetric membranes [26].

All the membranes synthesized in the aforementioned studies demonstrated great potential for application in blood oxygenators. However, their gas exchange rates remain unsatisfactory and must be improved [30].

# 2. Framework and Thesis Objectives

A review of previous studies reveals that, although polyurethane membranes exhibit great potential for applications in biomedical devices due to their high hemocompatibility, improvements are required in terms of their permeation properties. Thus, this work aims at developing novel gas permeation membranes from different materials for more efficient blood oxygenators.

The main objectives of this thesis are:

1. The design and synthesis of various groups of polyurethane-based membranes towards high carbon dioxide and oxygen permeabilities, namely pure polymer, polymer-based and mixed matrix membranes.
2. The characterization of the membranes in terms of surface morphology and cross-section structure, chemical composition, mechanical properties and gas permeation performance.

# 4. Experimental

## 4.1. Materials

### 4.1.1. Materials for membrane synthesis

All of the membranes in this work were prepared using a poly(propylene oxide) (PPO) based polyurethane prepolymer (PU) containing three isocyanate terminal groups and a molecular weight (MW) of approximately 3500 Da. This prepolymer was supplied by Fabrires - Produtos Químicos S.A. (Vendas Novas, Portugal). The solvent used was dimethylformamide (DMF) (p.a. grade, 99.8%) provided by Panreac (Barcelona, Spain).

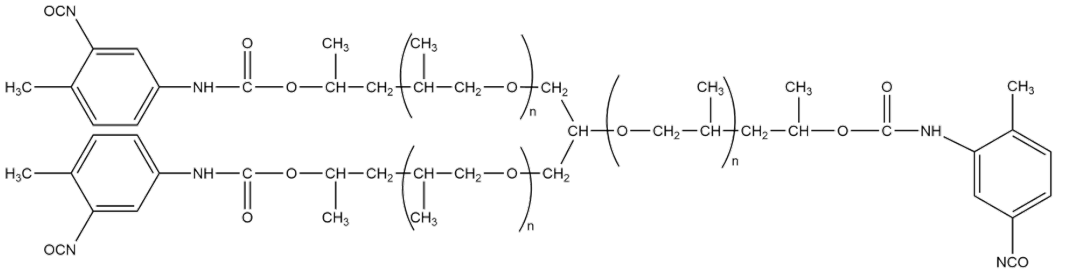

(a)

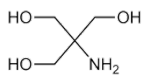

(b)

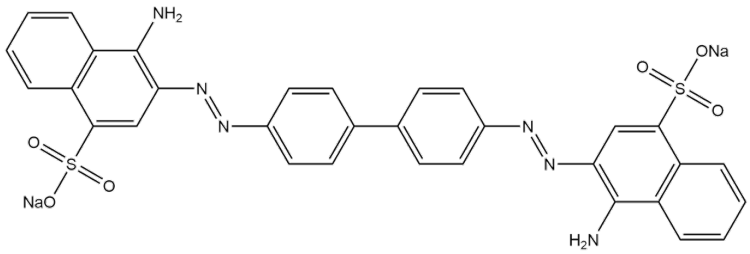

(c)

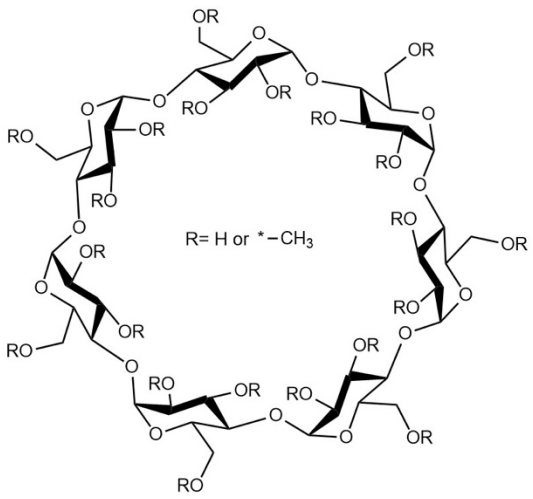


(d)

Figure 4. Chemical structures of: a) polyurethane prepolymer (PU), b) tris(hydroxymethyl) aminomethane (TRIS) , c) Congo red (CR), and d) methyl-beta-cyclodextrin (MBCD).

In addition to the polyurethane, three reagents were used: tris(hydroxymethyl)aminomethane (TRIS), Congo red (CR), and methyl-beta-cyclodextrin (MBCD). TRIS (purity ≥ 99.8%) was provided by Sigma-Aldrich (St. Louis, MO, USA). CR (purity > 98.0%) was provided by Tokyo Chemical Industry Co., Ltd. (Tokyo, Japan). MBCD, with a MW of 1303.3 Da, was provided by Sigma-Aldrich (St. Louis, MO, USA). The chemical structures of the PU, TRIS, CR and MBCD can be found in Figure 4.

Lastly, two metal-organic frameworks (MOFs) were kindly provided by Dr. Anirban Karmakar from the Center of Structural Chemistry at Instituto Superior Técnico. The first MOF, Zn-$NH_2$-BDC (also referred to as IRMOF-3), is built from the reaction of zinc nitrate with amine-functionalized terephthalic acid ($NH_2$-BDC) [40], [41]. The second MOF is Cu-BTC (alternatively known as HKUST-1), obtained from the reaction of copper (II) nitrate and 1,3,5-benzene tricarboxylic acid (BTC). Both MOFs were synthesized according to previously reported methods [42]. Figure 5 illustrates the structures of Zn-$NH_2$-BDC and Cu-BTC.

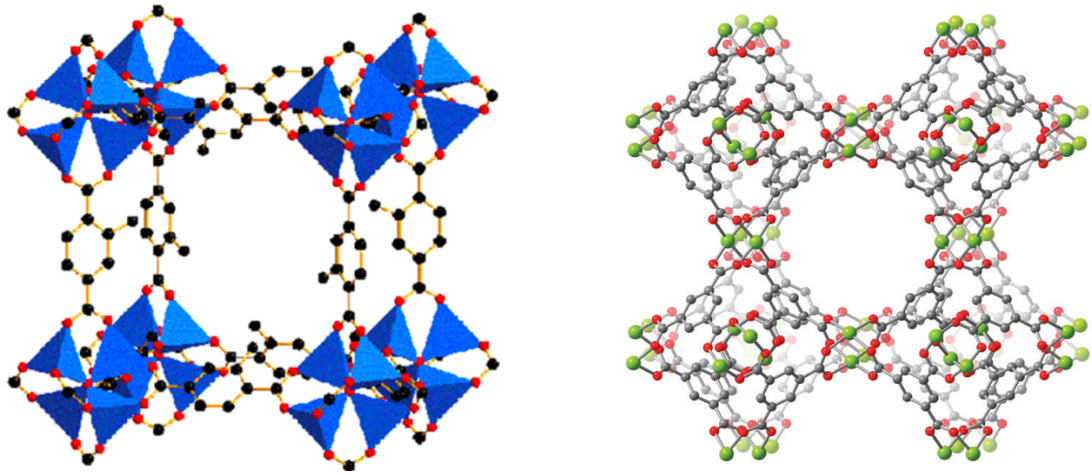

(a) (b)

Figure 5. Crystal structures of: a) Zn-$NH_2$-BDC [43] and b) Cu-BTC [44]. The blue tetrahedra represent the Zn atoms while the red, black, blue and green spheres represent the O, C, N and Cu atoms, respectively.

The reagents used in other formulations which did not result in successful membrane formation can be found in appendix A.

### 4.1.2. Commercial membrane

A sample of a commercial membrane from a model 0600 MBO marketed by Avecor/Medtronics, was tested in the experimental gas permeation set-up used in this work. It is a silicon rubber nonporous symmetric membrane with a webbed support structure which acts as a spacer between the folds of the spiral wound membrane module. Scanning electron microscopy (SEM) images of the top surface, bottom support surface and cross-section, previously obtained by Eusebio [45] for the same type of membrane, are presented in Figure 6. The average thickness of the membrane (excluding the woven support), determined from the SEM images of the cross-section using the ImageJ software, is equal to 66 ± 1.2 μm.

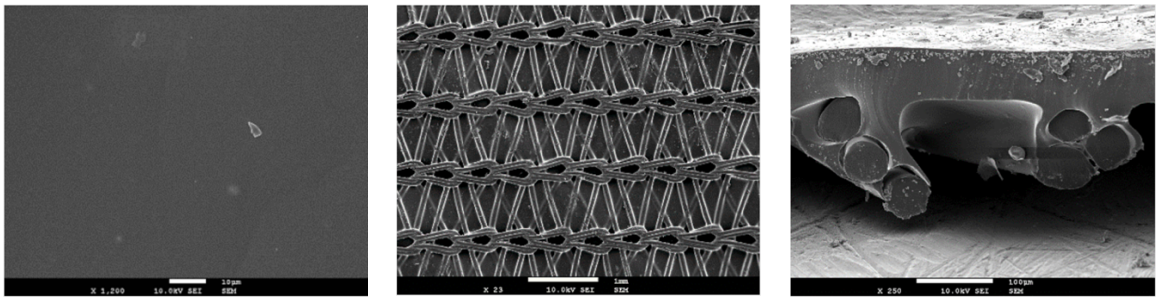

(a) (b) (c)

Figure 6. Scanning electron microscopy (SEM) images of the commercial membrane: (a) upper surface, (b) bottom support surface and (c) cross-section [44].

#### 4.1.3. Gases for permeation tests

The gas permeation experiments were performed using carbon dioxide (purity ≥ 99.98%) and oxygen (purity ≥ 99.5%), both provided by Air Liquide (Lisbon, Portugal).

## 4.2. Membrane synthesis

#### 4.2.1. Group 1: Pure polyurethane membranes

Two types of nonporous symmetric membranes of pure polyurethane were synthesized, one using no solvent and one using DMF as solvent, labeled PU and PU-s respectively. The PU membrane was prepared by pouring PU prepolymer directly into a 250 μm casting knife and spreading it onto a glass plate. The film was then left to cure for 24 to 48 hours at room temperature. The chemical structure obtained is seen in Figure 7. Lastly, the membrane was detached from the glass plate in a deionized water bath and placed on a sheet of paper to dry.

For the PU-s membrane, a casting solution of PU prepolymer and DMF was prepared using a prepolymer to solvent wt.% ratio of 65/35. After 2 hours of magnetic agitation and 10 minutes in an ultrasound bath to eliminate any air bubbles created during stirring, the solution was cast and cured using the same procedure previously described for the PU membrane.

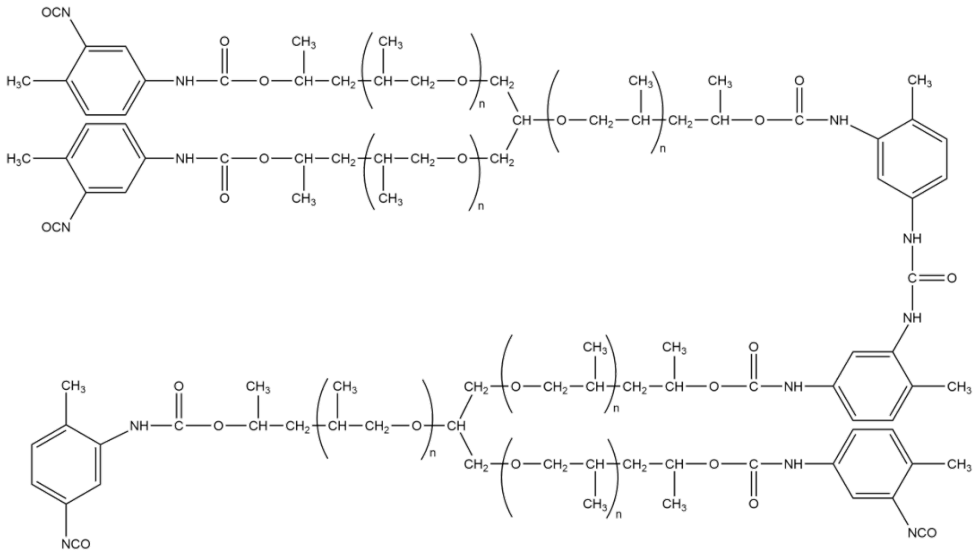

Figure 7. Chemical structure of two conjugated PU prepolymer units.

### 4.2.2. Group 2: Polyurethane-based membranes

Three components, tris(hydroxymethyl)aminomethane (TRIS), Congo red (CR), and methyl-beta-cyclodextrin (MBCD), were used in the preparation of polyurethane-based dense membranes designated by PU/TRIS, PU/CR and PU/MBCD, respectively. Figures 8, 9 and 10 illustrate the possible outcomes of the reactions between PU and TRIS, CR and MBCD respectively.

The casting solutions were prepared by first dissolving each powder component (TRIS, CR and MBCD) in DMF and then adding them to the PU-prepolymer. The total solid to solvent wt.% ratio used was always 65/35. The wt.% ratio of PU to the second component was 99.2/0.8 for the PU/TRIS solution and 99.6/0.4 for both PU/CR and PU/MBCD solutions.

Each casting solution was subjected to magnetic agitation for 2 hours, and 10 minutes in an ultrasound bath, before being cast onto glass plates using a 250 µm casting knife. Then, the membranes were left to cure at room temperature for 24 to 48 hours and, finally, they were detached from the glass plates in a deionized water bath.

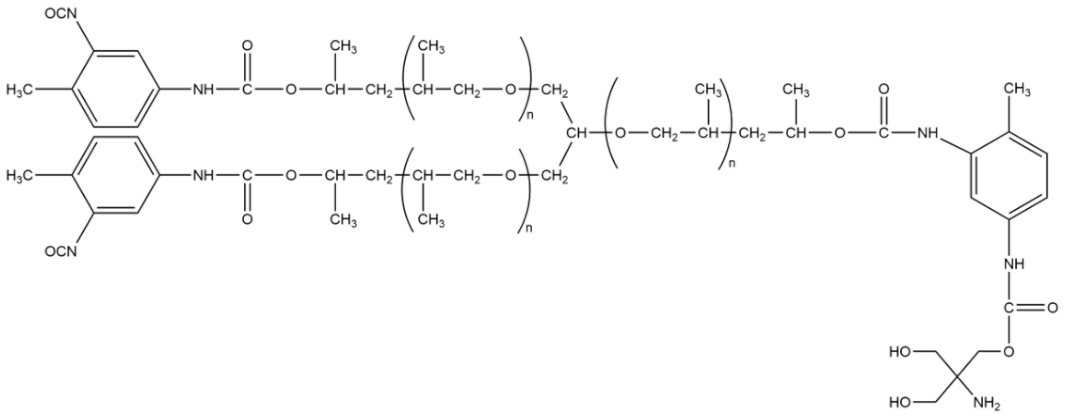

(a)

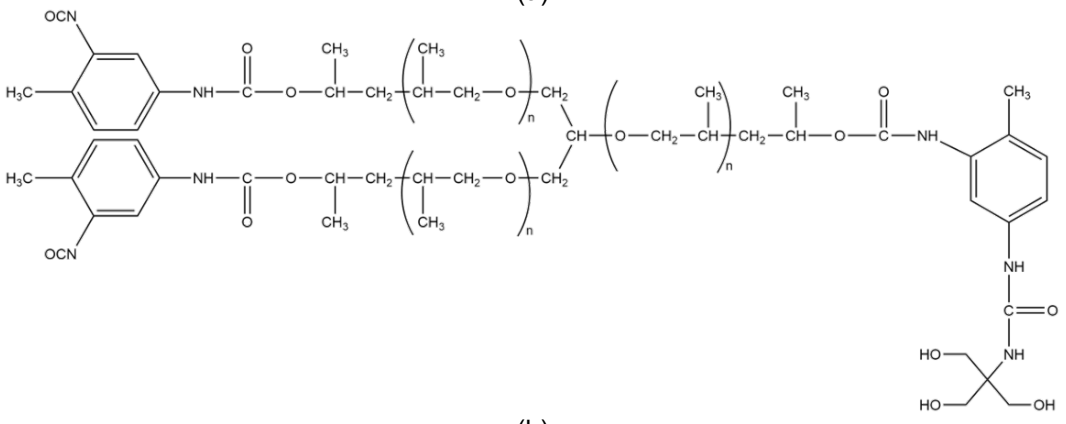

(b)

Figure 8. Possible chemical structures obtained from the reaction of PU and TRIS when the reaction occurs between the NCO group of PU and a) the OH group of TRIS, or b) the $NH_2$ group of TRIS.

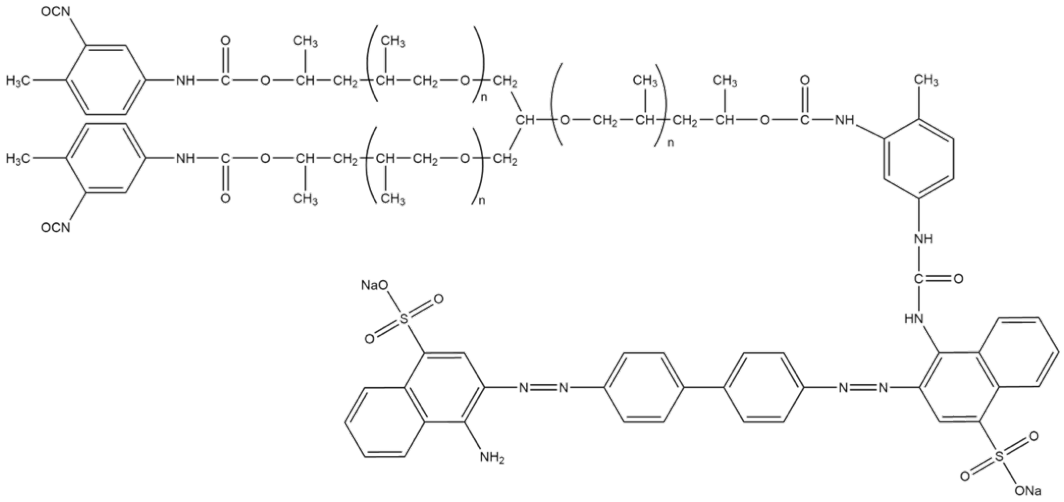

Figure 9. Possible chemical structure obtained from the reaction between the NCO group of PU and the $NH_2$ group of CR.

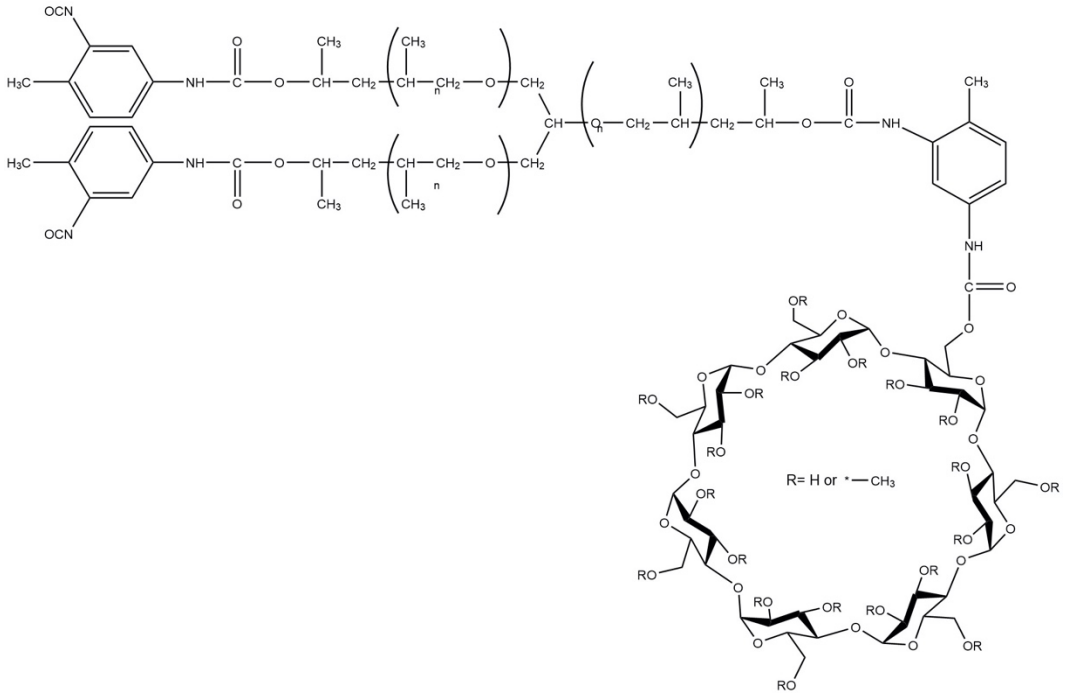


Figure 10. Possible chemical structure obtained from the reaction between the NCO group of PU and the OH group of MBCD.

### 4.2.3. Group 3: Mixed Matrix Membrane

Two types of mixed matrix membranes (MMMs) were synthesized by adding metal organic frameworks (MOFs), namely Cu-BTC or Zn-$NH_2$-BDC, to polyurethane. These nonporous symmetric membranes are designated by PU/Cu-BTC and PU/Zn-$NH_2$-BDC, respectively.

The casting solutions were prepared using a total solid to DMF wt.% ratio of 90/10. Each MOF is first dissolved in half of the solvent and introduced in an ultrasound bath for 15 minutes. Then, the dispersion is added to PU-prepolymer. The unused second half of the solvent is used to recover and wash out any remaining MOFs from the suspension into the casting solution. Two wt.% ratios of PU to

Cu-BTC were used, 99.9/0.1 and 99.0/1.0, forming PU/Cu-BTC-0.1 and PU/Cu-BTC-1.0 membranes, respectively. Only one polyurethane to Zn-$NH_2$-BDC wt.% ratio of 99.9/0.1 was used to form the PU/Zn-$NH_2$-BDC membrane.

Similarly to the procedure described in the previous sections, the casting solutions were magnetically stirred for 2 hours and sonicated for 10 minutes to eliminate any existing gas bubbles. The solutions were then cast using a 250 µm casting knife, and left exposed to the atmosphere at room temperature, for 24 to 48 hours. Once cured, the membranes were removed from the glass plate in a deionized water bath and laid to dry on sheets of paper.

## 4.3. Membrane characterization

### 4.3.1. Scanning Electron Microscopy and Energy-dispersive X-ray spectroscopy

Samples of the synthesized membranes were observed by Scanning Electron Microscopy (SEM) using a Thermo Scientific™ Phenom™ ProX G6 desktop SEM (Waltham, MA, USA). Part of the membrane samples were cut into small pieces and laid-out on a stub with the surface facing up, while other samples were fractured into pieces using liquid nitrogen to obtain a clean cut and then mounted on a stub with the cross-section facing up. Lastly, all the samples were sputter-coated with gold before being observed. For each membrane, pictures of the cross-section, top surface and, in some cases, bottom surface were taken. The average thickness of the cross-sections and respective standard deviations were determined from measurements on five different regions of the SEM images of the cross-sections, using the software ImageJ2 version 2.3.0 developed by NIH (Bethesda, MD, USA) [46]. Additionally, energy-dispersive X-Ray spectroscopy (EDS) was used to detect the presence of metallic elements in the membranes containing MOFs.

### 4.3.2. Attenuated Total Reflectance - Fourier Transform Infrared Spectroscopy

Attenuated Total Reflectance - Fourier Transform Infrared (ATR – FTIR) spectroscopy was used to analyze the active layer of each polyurethane-based membrane. The equipment used was a Nicolet 5700 FT-IR spectrometer (Thermo Electron Scientific Instruments, Madison, WI, USA) with a Golden Gate MKII ATR accessory with a Ge crystal (Graseby Specac, Smyrna; sampling depth: 0.2–1.1 µm at 4000–400 cm-1), both shown in Figure 11. FTIR spectra were obtained from one sample of each composition by averaging 264 scans with a resolution of 4$cm^{-1}$, and processed using the OMNIC™ software (Thermo Fisher Scientific, Waltham, MA, USA).

Figure 11. Photograph of the Nicolet 5700 FT-IR spectrometer with Golden Gate MKII ATR accessory.

### 4.3.3. Mechanical Tests

Uniaxial tensile tests were performed on five types of polyurethane-based membranes, namely PU, PU-s, PU/TRIS, PU/CR and PU/MBCD, using an Instron® 5544 universal testing machine (Norwood, MA, USA) coupled with an Instron® model 2663-822 standard video extensometer (Norwood, MA, USA), and a load cell of 100N. The experimental set-up is shown in Figure 12. All the tests were performed with the help of Dr. Sérgio Gonçalves in the Laboratory of Tissue Biomechanics at Instituto Superior Técnico, on the same day to reduce the variability of the testing conditions.

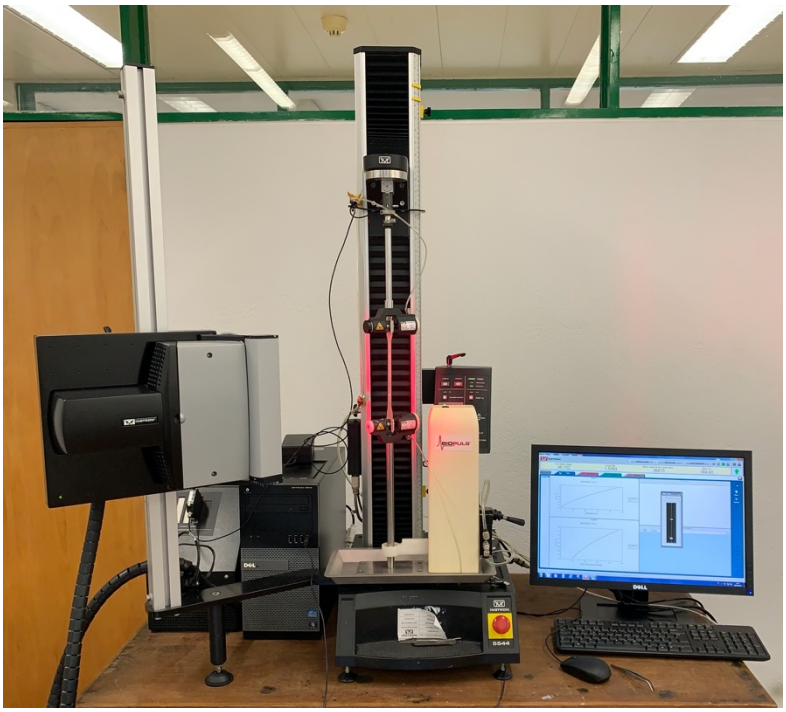

Figure 12. Photograph of the Instron® 5544 universal testing machine and Instron® model 2663-822 standard video extensometer.

For each composition, multiple specimens were cut from pre-cast membranes, using a 3D-printed cutting cast (placed always in the same direction to avoid the effects of anisotropy) and scissors.

Any specimens exhibiting irregular edges from the cutting process were discarded. Prior to testing, each specimen was marked with two white dots that delimit the gauge length (of 60 mm). These marks act as reference points for the video extensometer, which uses them to calculate the strain. Figure 13 shows the reference marks and the dimensions used for the tensile specimens.

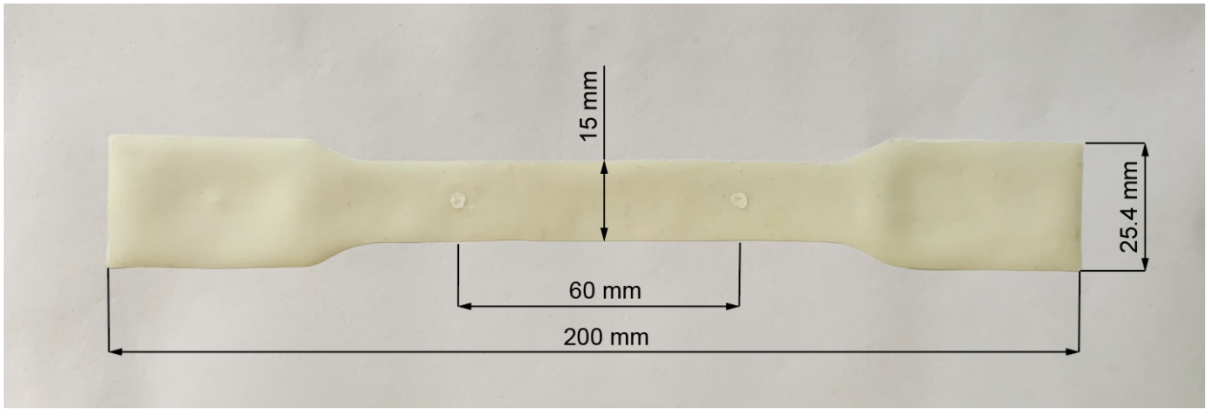


Figure 13. Dimensions of a tensile test specimen.

The thickness of all the individual specimens was measured using a Dexter® digital caliper with 0.01 mm precision (Lezennes, France). The average thickness values obtained for each formulation can be found in appendix B. The cross-sectional area of each specimen was then calculated by multiplying the measured thickness by the specimen's width (15mm).

Before the start of the test, each specimen was carefully placed in between the pneumatic grips of the testing machine. A pre-tension of approximately 0.15 MPa (or 0.2 N) was applied to ensure that the tension was evenly distributed along the cross section of the specimen. Finally, the specimens were tested until rupture, at ambient conditions, with a uniform elongation rate of 15mm/min (0.0041 $s^{-1}$) [47]. The evolution of the extension, load and video axial strain over time were recorded by a computer using the Instron® Blue Hill version 3 software (Norwood, MA, USA). The data collected was used to plot the stress-strain curves of each specimen. Additionally, the average values of the Young's modulus (E), yield point, ultimate tensile point and fracture point, were calculated from the results obtained for five specimens of each composition. Only specimens which ruptured in the neck region were selected for further analysis [48].

## 4.4. Gas permeation experiments

### 4.4.1. Theory

#### 4.4.1.1. Solution-Diffusion Model

When a pressure difference is applied across a dense membrane, it acts as the driving force for the transport of gas, a process which is commonly described by the solution-diffusion model. Figure 14 schematically shows the transport of a gas across a membrane which can be described by three

main steps: the permeating gas dissolves into the polymer at the feed side, diffuses through the membrane down a concentration gradient, and is then desorbed at the permeate side.

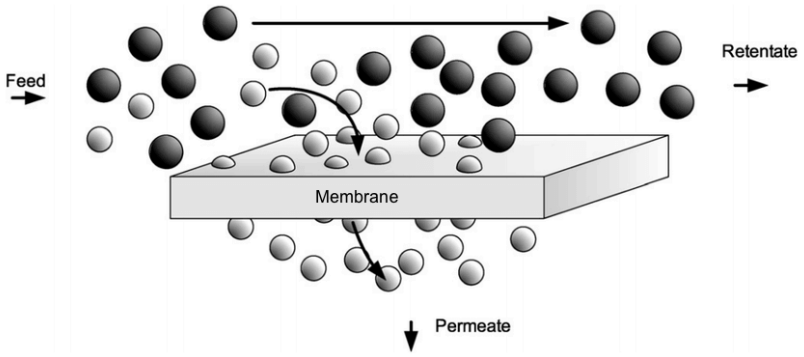


Figure 14. Schematic of gas separation through a membrane [49].

Figure 15 exemplifies the typical permeation curve (permeate pressure vs. time) obtained for the transport of a gas across a polymeric membrane. The curve typically exhibits three different regions: the penetration state, in which the permeate pressure remains constant through time, the transient state, during which the permeation rate gradually increases with time, and finally, the steady state, marked by a constant flux of gas across the membrane [50].

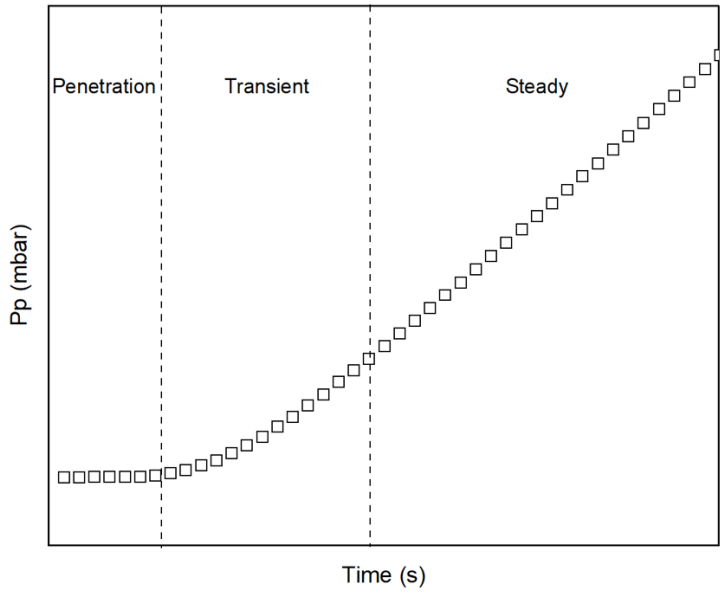


Figure 15. Plot of the permeate pressure versus time, showing the penetration, transient and steady regions.

In the solution-diffusion model, the permeability, $P$, of a gas through a membrane is controlled by its solubility coefficient, $S$, and diffusion coefficient, $D$[12]:

$$P = SD \tag{1}$$

In the steady state, the unidimensional diffusive flux is described by the Fick's first law of diffusion:

$$J_i = -D_i \frac{dC_i}{dx} \tag{2}$$

where $J_i$ is the flux of species $i$ in the $x$ direction and is proportional to the concentration gradient $\frac{dC_i}{dx}$, $C_i$ is the concentration of species $i$ in the membrane, and $D_i$ is a proportionality constant defined as the diffusion coefficient, which is independent from the concentration at low pressure ranges [51].

The integration of Fick's first law across the total thickness, $\ell$, of the membrane gives:

$$J_i = \frac{D_i}{\ell}(C_{i0} - C_{i\ell}) \tag{3}$$

where $C_{i0}$ and $C_{i\ell}$ are the concentrations of species $i$ in the membrane on the feed side and permeate side respectively.

In elastomers, the solubility of gases tends to be very low and can be described by Henry's Law:

$$C = Sp \tag{4}$$

where $C$ is the concentration inside the polymer and is proportional to the applied pressure, $p$ [52].

By applying Henry's Law, the relations below can be established:

$$S_i = \frac{C_{i0}}{p_f} = \frac{C_{i\ell}}{p_p} \tag{5}$$

where $S_i$ is the solubility coefficient of species $i$, $p_f$ is the pressure on the feed side and $p_p$ is the pressure on the permeate side.

By combining expressions (3) and (5), the following expression is obtained:

$$J_i = \frac{D_i S_i}{\ell}(p_f - p_p) \tag{6}$$

Equation (1) gives us that the product $D_i S_i$ is equal to the permeability coefficient of species $i$, $P_i$, and thus, expression (6) can be written as follows:

$$J_i = \frac{P_i}{\ell}(p_f - p_p) \tag{7}$$

The permeability coefficient is commonly expressed in Barrer, with:

$$1\ Barrer = 10^{-10}\left(\frac{cm^3(STP)cm}{cm^2 s\ cmHg}\right)$$

When the thickness is difficult to determine, the pressure normalized flux or permeance may be used instead:

$$Perm = \frac{P_i}{\ell} \tag{8}$$

For a mixture of gases $A$ and $B$, the ideal selectivity of the membrane, $\alpha_{A/B}$, can be described as the ratio between the permeabilities or permeances of the individual gases [12]:

$$\alpha_{A/B} = \frac{P_A}{P_B} = \frac{Perm_A}{Perm_B} \tag{9}$$

#### 4.4.1.2. Time-Lag Method

The mass balance of the unidimensional diffusive transport of species $i$ across a nonporous polymeric membrane in the transient state is given by:

$$-\frac{dC_i}{dt} = \frac{dJ_i}{dx} \tag{10}$$

By combining this expression with Fick's First Law from equation (2), Fick's Second Law is obtained:

$$\frac{dC_i}{dt} = D_i \frac{d^2C_i}{dx^2} \tag{11}$$

In a system where the membrane is initially free of diffusing species, the following initial and boundary conditions can be considered:

$$C_i(x, 0) = 0 \tag{12.a}$$

$$C_i(0, t) = C_{i0} \tag{12.b}$$

$$C_i(\ell, t) = C_{i\ell} \approx 0 \tag{12.c}$$

meaning that the upstream concentration, $C_{i0}$, remains constant and, in comparison, the downstream concentration, $C_{i\ell}$, is negligible. The solution of equation (10) is obtained by satisfying the boundary conditions listed above, and either through Laplace transform or separation of variables [53], [54]:

$$C_i = C_{i0}\left(1 - \frac{x}{\ell}\right) + \frac{2C_{i0}}{\ell} \times \sum_{n=1}^{\infty} \frac{1}{n} \sin\left(\frac{n\pi x}{\ell}\right) \exp\left(-\frac{D_i n^2 \pi^2 t}{\ell^2}\right) \tag{13}$$

The diffusive flux, $J_i$, results from substituting equation (13) in Fick's First Law:

$$J_i(x, t) = \frac{D_i C_{i0}}{\ell} + \frac{2D_i C_{i0}}{\ell} \times \sum_{n=1}^{\infty} \cos\left(\frac{n\pi x}{\ell}\right) \exp\left(-\frac{D_i n^2 \pi^2 t}{\ell^2}\right) \tag{14}$$

where the first and second terms represent the steady state and transient state contributions of the flux, respectively. This expression is a function of time, $t$, and displacement in the direction of diffusion, $x$, which can easily be solved for the fluxes entering ($x$ = 0) and leaving ($x$ = $l$) the membrane.

A time-dependent expression for the flux at the downstream end of the membrane can be obtained by setting $x$ = $\ell$. Its integration with respect to time results in the quantity of species $i$ permeating out of the membrane, $Q_{i\ell}$:

$$Q_{i\ell}(t) = -A \int_0^t J_i(t)dt = \frac{AD_i C_{i0}}{\ell}\left[t - \frac{\ell^2}{6D_i} + \frac{2\ell^2}{\pi^2 D_i} \times \sum_{n=1}^{\infty} \frac{(-1)^{n+1}}{n^2} \exp\left(-\frac{D_i n^2 \pi^2 t}{\ell^2}\right)\right] \tag{15}$$

An expression for the permeate pressure can then be obtained from equation (15):

$$p_p(t) = \frac{AD_i p_f}{V\ell}\left[t - \frac{\ell^2}{6D_i} + \frac{2\ell^2}{\pi^2 D_i} \times \sum_{n=1}^{\infty} \frac{(-1)^{n+1}}{n^2} \exp\left(-\frac{D_i n^2 \pi^2 t}{\ell^2}\right)\right] \quad (16)$$

where $A$ is the area of the cross-section (perpendicular to the direction of diffusion) through which the gas permeates, and $V$ is the volume of the receiving chamber. The transient term of equation (16) can be reduced to zero by calculating the limit as $t \rightarrow \infty$, resulting in the following expression for the permeate pressure:

$$\lim_{t\to\infty} p_p(t) = \frac{AD_i p_f}{V\ell}\left[t - \frac{\ell^2}{6D_i}\right] \quad (17)$$

In the plot of the permeate pressure versus time, the time value at which the steady state asymptote intercepts the time axis is defined as the time lag, $t_{lag}$. An example of the application of this method is shown in Figure 16.

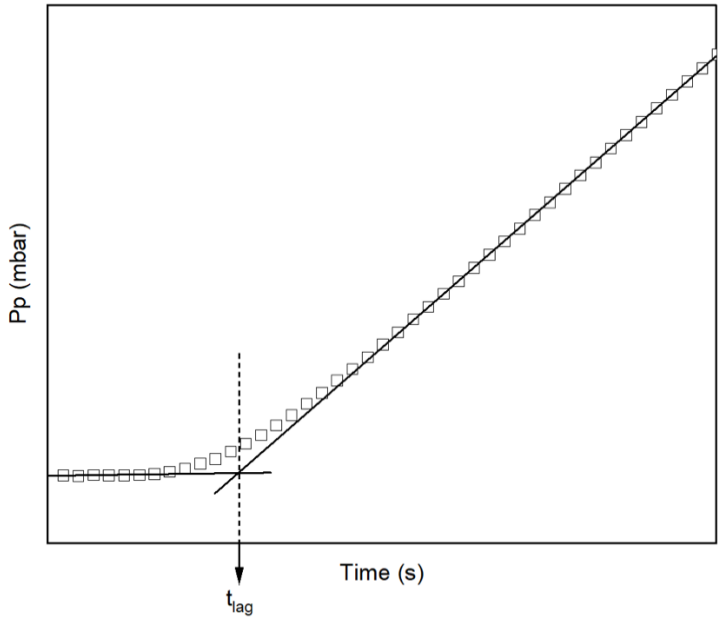


Figure 16. Plot of the permeate pressure versus time showing the time lag value, $t_{lag}$, at the interception of the x axis ($p_p$=0) and the steady state asymptote.

Knowing the time lag value and the membrane thickness, the diffusion coefficient can be obtained by:

$$t_{lag} = \frac{\ell^2}{6D_i} \quad (18)$$

### 4.4.2. Experimental set-up

In this work, the gas permeation properties of the PU membranes were determined using the optimized set-up shown in Figure 17, by the constant volume method. This method studies the gas flux through a membrane, by the application of gas at constant pressure to the feed side of the membrane, and the subsequent measurement of the variation of pressure in the receiving chamber (of constant volume) as a function of time.

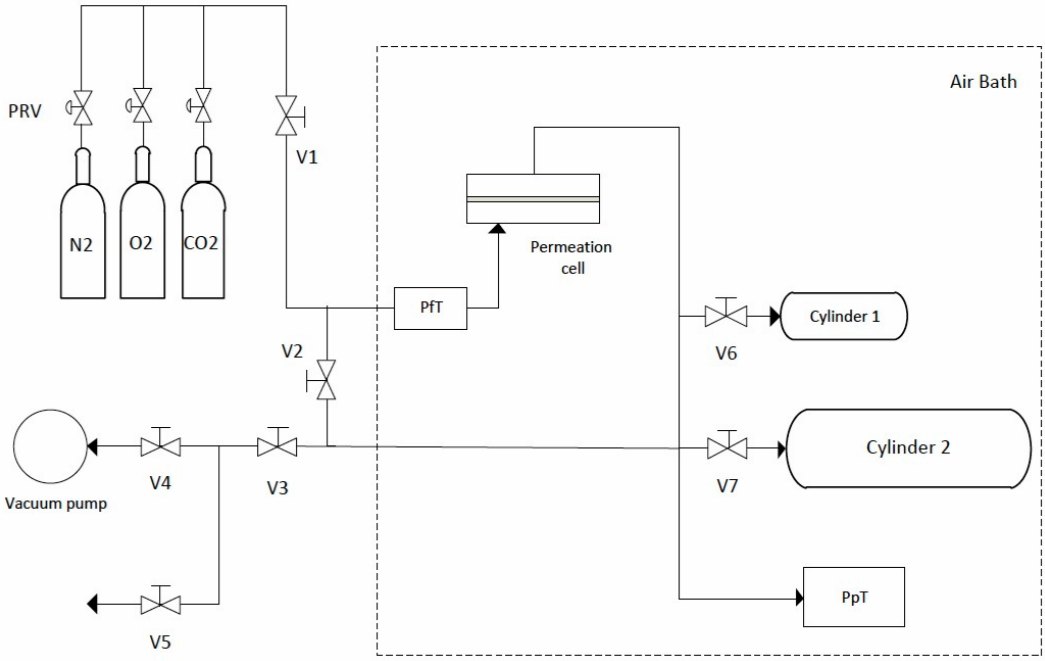


Figure 17. Schematic representation of the gas permeation set-up [43].

The permeation cell consists of two detachable flat plates made of stainless steel. Between the plates, there is a porous support with an effective surface area of 9.62 $cm^2$, on which a membrane sample is placed to be tested. Figure 18 shows a schematic representation of the permeation cell.

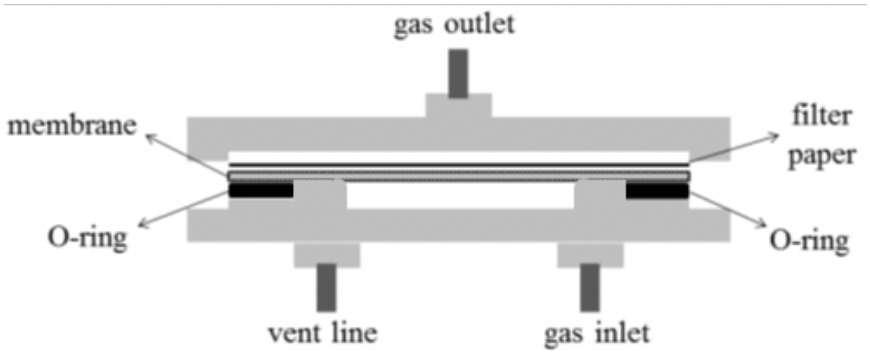


Figure 18. Schematic representation of the permeation cell [44].

The feed gas cylinder, coupled to a pressure regulating valve (PRV), is connected to the feed side of the permeation cell through a valve (V1) and a Setra model 205-2 (Boxborough, MA, USA) feed pressure sensor (PfT). The receiving chamber on the permeate side of the cell is made up of two cylinders of different sizes, cylinder 1 with 12.6 ± 0.1 $cm^3$ and cylinder 2 with 167.2 ± 0.2 $cm^3$, connected through valves V6 and V7 respectively, and tubing with a volume of 13.5 ± 0.01 $cm^3$. The total volume of the receiving chamber is 193.3 ± 0.3$cm^3$. Connected to the permeate side is a Paroscientific Inc. model 6100A-CE (Redmond, WA, USA) permeate pressure transmitter (PpT) which, in turn, is connected to a Paroscientific Inc. model 710 display unit, and to a computer. The computer automatically records the permeate pressure as a function of time using the Digiquartz Interactive DQ13 ® version 1.0.1.0 software from Paroscientific Inc [55].

Both sides of the permeation set-up are linked through a series of valves (V2 to V5) to an Edwards model E2M2 vacuum pump (Burgess Hill, UK) and to the atmosphere. Lastly, the connections between the components of the system were made using Hoke® stainless steel 316 tubes with 1/8-inch outer diameter, Hoke® 3700 series needle valves, and Gyrolok® tube fittings of several materials (stainless steel, titanium and brass).

The set-up is installed inside a glass door refrigerator (wine cellar) that functions as a thermostatic air bath. The temperature inside the air bath is homogenized using a Hart Scientific model 2100 temperature controller (Everett, WA, USA) connected to a heater and two fans, and to a platinum resistance thermometer. Figure 19 shows the experimental set-up used for the permeation measurements, including the feed gas cylinders, vacuum pump, air bath and various pressure and temperature sensors.

It should be noted that, prior to the experiments, cylinder 1 had been calibrated by gravimetry [45], allowing for the calibration of cylinder 2 and of the tubes by gas expansion [56].

Figure 19. Photograph of the experimental set-up used for permeation measurements.

The experimental set-up just described was developed by Pon [56] as an optimized version of the set-up built by Eusébio [45].The original configuration presented problems such as low reproducibility and significant uncertainty associated with highly permeable membranes. Moreover, in measurements using $N_2$ and $O_2$, a transient state was not observed making it impossible to use the timelag method to determine the solubility and diffusion coefficients for these gasses.

One of the main updates made by Pon [56] was the addition of vacuum pump, which allows the system to be degassed prior to each measurement, obeying the initial and boundary conditions employed in Fick's second law. Other modifications were made to the configuration of the permeate side, by optimizing the relative positions of the PpT manometer and of the buffer cylinders, as well as their respective volumes, in order to minimize the resistance to gas transport exhibited because of Knudsen flow at low pressures, which was affecting the experimental results.

### 4.4.3. Procedure

A circular excerpt of 5cm diameter is cut out of the membrane obtained from the casting. Before starting, the average thickness of each sample is determined through measurements on 5 sampling points using a manual caliper with 0.02mm precision from Magnusson (Longpont-sur-Orge, France). This sample is introduced into the permeation cell, which is then closed.

Before beginning the measurements, the system is thermostated until the temperature stabilizes at approximately 37ºC ± 0.3. Simultaneously, the membrane is degassed using the vacuum pump, keeping all the valves opened except for valves V1 and V5.

Once the system has been properly degassed and the temperature has stabilized, valves V2 and V3 are closed, and one single gas is fed (either $CO_2$ or $O_2$) by regulating the pressure reducing valve (PRV) on the gas cylinder to feed pressures between 1.5 and 4 bar. The permeation measurement starts when valve V1 is opened and the permeate pressure, detected by the PpT sensor in the receiving chamber, begins being recorded as a function of time, in intervals of approximately 1.3 seconds with milibar precision. Throughout the test, the feed pressure is monitored by the pressure transmitter PfT, ensuring that it remains constant.

At the end of the measurement, valve V1 is closed, and valves V2 and V3 are reopened. The system is allowed to degass for at least 10 minutes before the next measurement. Each sample is tested at five to six different feed pressures and is then switched for the next sample.

Valve V5 remains closed during each set of permeation tests and is only opened when it is necessary to return to atmospheric pressure, namely when switching samples inside the permeation cell. Valves V6 and V7 can be manipulated to open or close cylinders 1 and 2 respectively, allowing for the total volume of the receiving chamber to be tailored to the permeance of the measured gas through the membrane sample, optimizing the accuracy of the measurements. In permeation measurements using carbon dioxide, only valve V6 was kept open making the total receiving volume 26.1 $cm^3$, while for oxygen, both valves remained closed, corresponding to a receiving volume of 13.5 $cm^3$.

The average permeability, diffusion and solubility coefficients were calculated using the data obtained from permeation measurements performed on three to six samples of each membrane.

# 5. Results and Discussion

## 5.1. Scanning Electron Microscopy

Nonporous symmetric pure polyurethane membranes PU and PU-s were synthesized using no solvent and polymer to solvent wt% ratio of 65/35, respectively. Figure 20 shows the SEM images of the top surface and cross-section of the pure polyurethane membrane (without any solvents). The PU membrane appears to be completely dense with no observable porosity.

| Membrane | Top surface | Cross-section |
|---|---|---|
| PU | 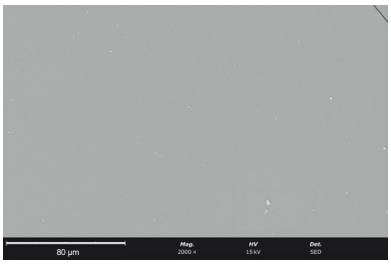 (a) | 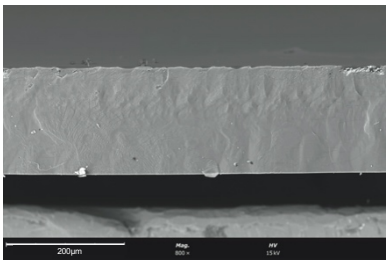 (b) |

Figure 20. SEM images of the nonporous symmetric PU membrane: (a) top surface (2000×), (b) cross-section (800x).

Two different types of structure were observed for the pure polyurethane membrane synthesized using 35% wt% solvent. SEM images of the top surface and cross-section for both PU-s structures are shown in Figure 21.

| Membrane | Top surface | Cross-section |
|---|---|---|
| PU-s* | 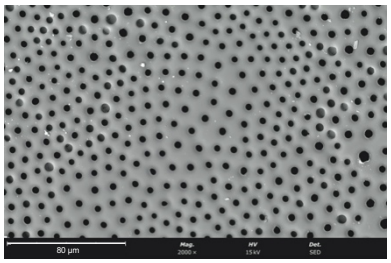 (a) | 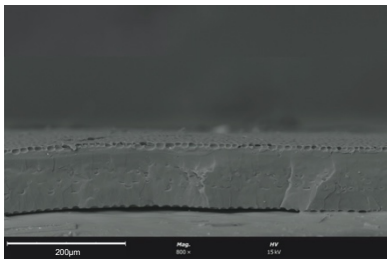 (b) |
| PU-s | 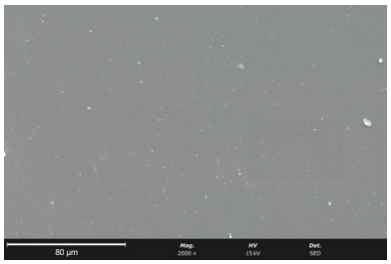 (c) | 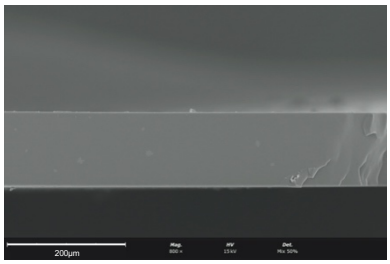 (d) |

Figure 21. SEM images of the nonporous symmetric PU-s* and PU-s membranes: (a) top surface of PU-s* (2000x), (b) cross-section of the of PU-s* (800x); (c) top surface of PU-s (2000x), (d) cross-section of PU-s (800x).

The first set of membranes, PU-s*, exhibits a dense, almost nonporous core, with porous top and bottom surfaces. The second set of membranes, PU-s, appears to be entirely dense with no visible pores on the surfaces or core. Both membranes were synthesized using the same materials, polymer to solvent ratio, agitation time and curing time. However, because they were prepared on different days, the variation in the composition of the atmosphere and of the room temperature could have affected the solvent evaporation process, thus resulting in different structures.

Nonporous symmetric polyurethane-based membranes, PU/TRIS, PU/CR and PU/MBCD, were prepared using a polymer to solvent wt% ratio of 65/35, and PU to second reagent wt% ratios of 99.2/0.8 for the PU/TRIS membrane and 99.6/0.4 for both PU/CR and PU/MBCD membranes.

SEM images of the top surfaces and cross-sections of the polyurethane-based membranes from group 2 are presented in Figure 22. All the polyurethane-based membranes have a dense, homogenous appearance with no discernable porosity. The addition of TRIS, CR and MBCD does not seem to have any influence on membrane morphology when compared to the dense PU-s membrane, which is synthesized using an analogous polymer to solvent ratio. Lastly, the PU/MBCD membrane contained small fissures sparsely distributed on its surface, which are thought to have originated during the removal of the membrane from the glass plate or from the sputter coating process of the SEM samples.

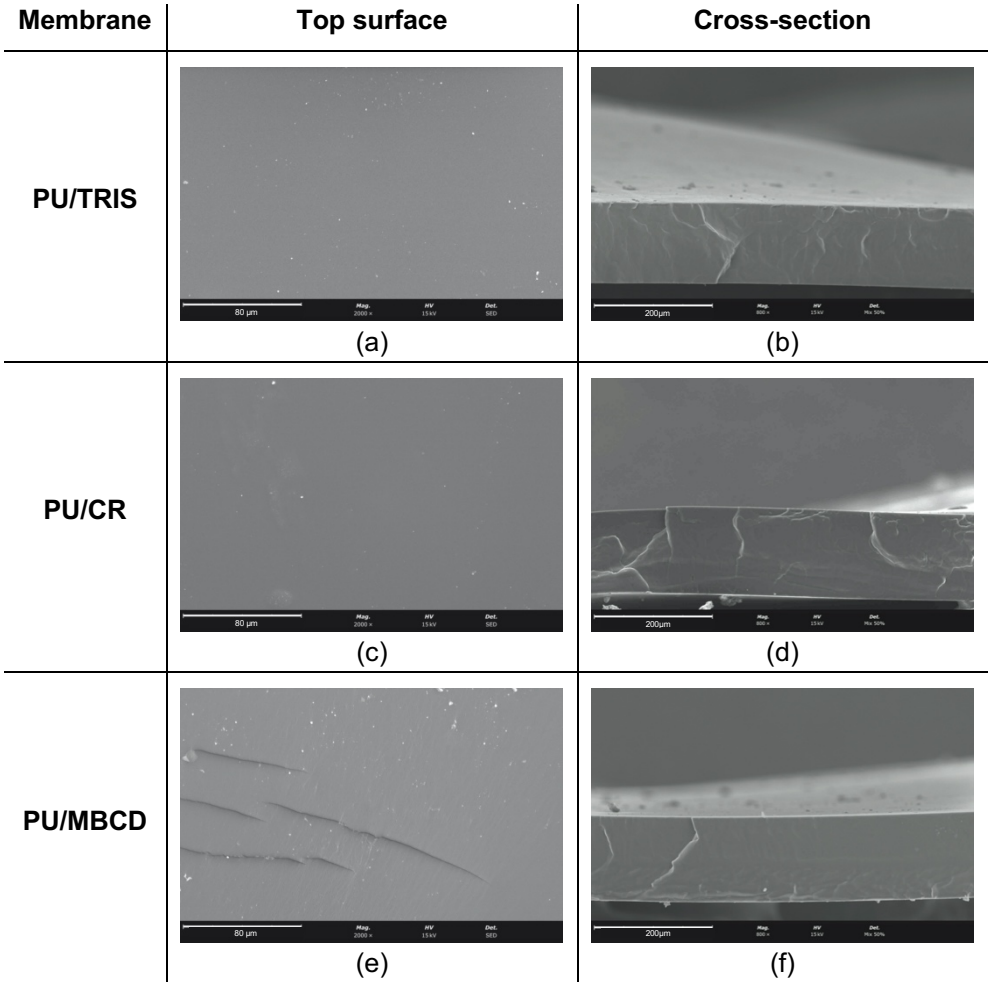


Figure 22. SEM images of the nonporous symmetric PU/TRIS, PU/CR and PU/MBCD membranes: (a) top surface of PU/TRIS (2000x), (b) cross-section of PU/TRIS (800x); (c) top surface of PU/CR (2000x), (d) cross-section of PU/CR (800x); (e) top surface of PU/MBCD (2000x), (f) cross-section of PU/MBCD (800x).

A third group of nonporous symmetric mixed matrix membranes, PU/Zn-$NH_2$-BDC, PU/Cu-BTC-0.1 and PU/Cu-BTC-1.0, were synthesized using polymer to solvent wt% ratio of 65/35, and PU to MOF wt% ratios of 99.9/0.1 for the PU/Zn-$NH_2$-BDC and PU/Cu-BTC-0.1 membranes, and 99/1 for the PU/Cu-BTC-1.0 membrane. SEM micrographs of the top surface and cross-section of the MMMs from group 3 are shown in Figure 23.

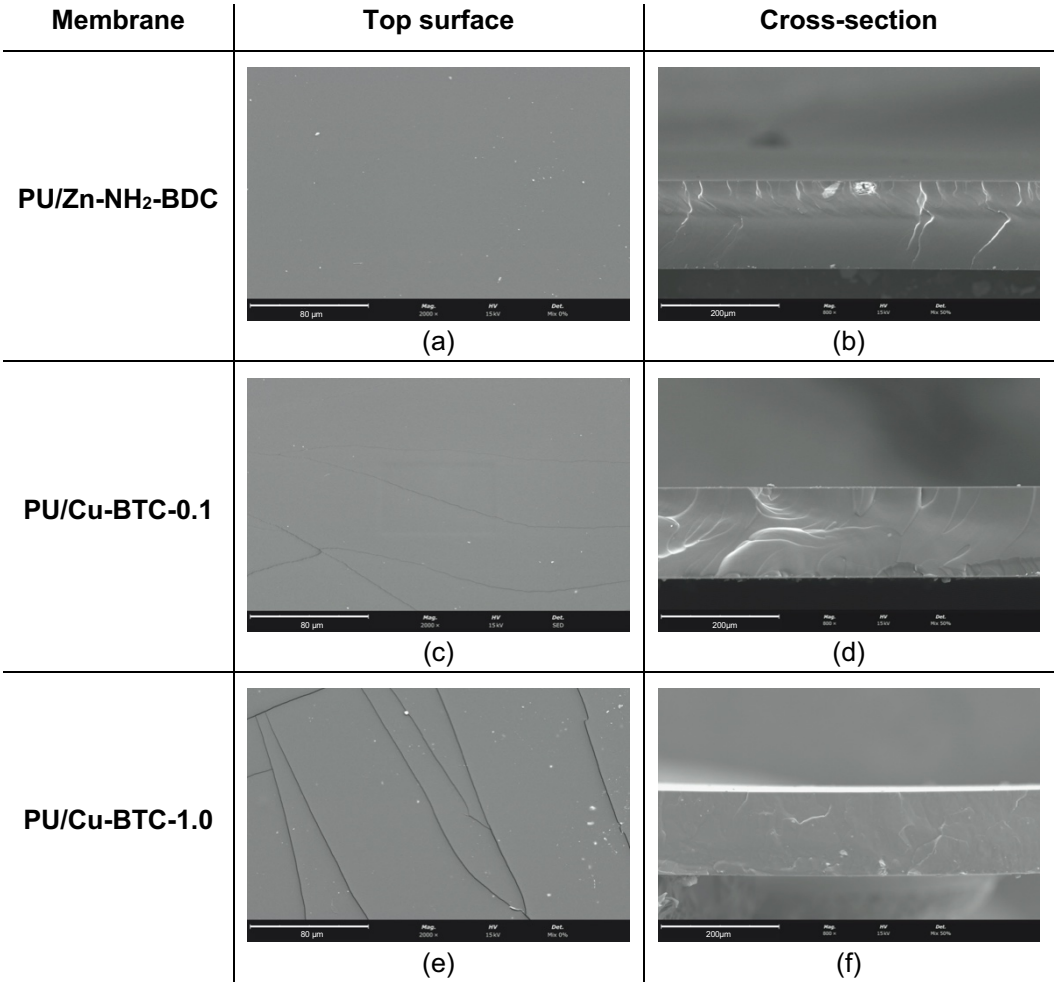


Figure 23. SEM images of the nonporous symmetric PU/Zn-NH2-BDC, PU/Cu-BTC-0.1 and PU/Cu-BTC-1.0 membranes: (a) top surface of PU/Zn-NH2-BDC (2000x), (b) cross-section of PU/Zn-NH2-BDC (800x); (c) top surface of PU/Cu-BTC-0.1 (2000x), (d) cross-section of PU/Cu-BTC-0.1 (800x); (e) top surface of PU/Cu-BTC-1.0 (2000x), (f) cross-section of PU/Cu-BTC-1.0 (800x).

All the MMMs exhibit dense matrices with no observable pores, similarly to the pure PU membrane. The cross-section images of the PU/Zn-$NH_2$-BDC (Figure 23.b) and PU/Cu-BTC-1.0 (Figure 23.f) membranes revealed the existence of small masses, presumably Zn-$NH_2$-BDC and Cu-BTC respectively, distributed throughout the polyurethane matrix. No fillers were found in the cross-section images of the PU/Cu-BTC-0.1 membrane (Figure 23.d), likely because the proportion of filler is so small that, coincidentally, no Cu-BTC was intercepted by the specific cross-sectional plane obtained during sample preparation.

The surfaces of each sample were examined using a backscattered electron (BSE) SEM signal, which is highly sensitive to differences in atomic number. The higher the material's atomic number, the brighter it appears on the image [57]. All three MMM samples contained discernable brighter, diffuse

spots dispersed through their surfaces, confirming the localized presence of MOFs within the membranes.

Once again, the observable cracks on the surfaces of the PU/Cu-BTC-0.1 and PU/Cu-BTC-1.0 membranes were likely created during the removal of the membranes from the glass plates or during the sputtering of the membrane samples. In any case, the fissures are not deep as they are not visible in any of the cross-section images.

The total thickness ($\ell$) of each studied membrane was measured on five points of the cross-section SEM micrographs using the ImageJ2 software [46]. Table 1 shows the average values and respective standard deviations obtained for each composition. The pure PU membrane synthesized with no solvent exhibits the highest thickness, while the PU-s membrane produced with 35 wt% solvent has the lowest thickness, suggesting that the introduction of solvent reduces the thickness of the membrane. All PU-based membranes and MMMs, from groups 2 and 3 respectively, exhibit intermediate values of thickness. Moreover, on average, the PU-based membranes synthesized with 35 wt% solvent are thinner than the MMMs prepared with 10 wt% solvent, which supports the premise that casting solutions with higher solvent content result in membranes with lower thickness.

Table 1. Average thickness ($\ell$) and respective standard deviation of the nonporous symmetric PU membranes from groups 1, 2 and 3, obtained from the SEM cross-sectional images.

| | **Membrane** | **Thickness, $\ell$ (μm)** |
|---|---|---|
| Group 1 | PU | 181 ± 0.9 |
| | PU-s* | 111 ± 0.6 |
| | PU-s | 125 ± 0.3 |
| Group 2 | PU/TRIS | 137 ± 1.0 |
| | PU/CR | 149 ± 0.3 |
| | PU/MBCD | 144 ± 0.4 |
| Group 3 | PU/ Zn-$NH_2$-BDC | 152 ± 0.9 |
| | PU/Cu-BTC-0.1 | 154 ± 0.9 |
| | PU/Cu-BTC-1.0 | 143 ± 0.7 |

The thickness of each membrane sample was also measured with a manual caliper and a digital caliper, and the obtained values can be found in appendix B. The thickness values used in all the work moving forward are the ones measured from the SEM images.

## 5.2. Energy-Dispersive X-ray Spectroscopy

During the scanning electron microscopy (SEM) session (and using the same equipment), energy-dispersive X-ray spectroscopy (EDS) was performed on the samples of the membranes containing MOFs (group 3), to analyze the composition of the masses observed in their cross-sections. Since no fillers could be distinguished in the cross-section of the PU/Cu-BTC-0.1 membrane, only the analysis of the PU/Zn-$NH_2$-BDC and PU/Cu-BTC-1.0 compositions provided useful information.

An example of an EDS spectrum obtained for the PU/Zn-$NH_2$-BDC membrane sample is displayed in Figure 24, and the weight percentages of each element detected are summarized in Table 2. The data shows that the masses visible in the cross-section of the membrane contained a significant amount of zinc (Zn), strongly suggesting that they were in fact Zn-$NH_2$-BDC particles. The high amounts of carbon (C) and oxygen (O) found were expected, as these elements constitute a large part of the PU's chemical structure. A small amount of aluminum (Al) was also revealed because the membrane samples were mounted on an aluminum support. Finally, the vestigial traces of silicon (Si) detected are most likely due to impurities.

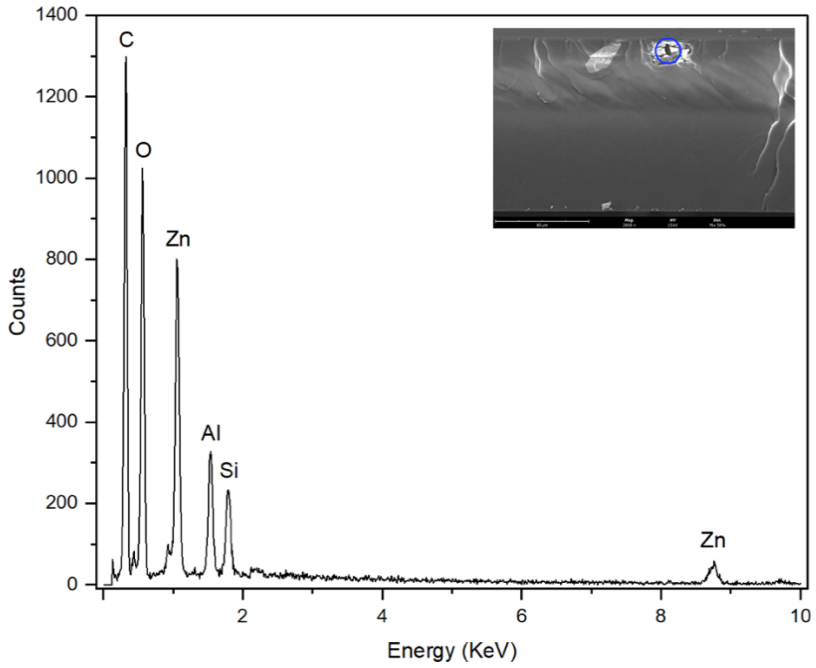


Figure 24. Energy-dispersive X-ray spectrum of the PU/Zn-$NH_2$-BDC membrane. The inset image shows the region of the SEM sample that was analyzed (circled in blue).

Table 2. Summary of the elements detected in the PU/Zn-$NH_2$-BDC membrane through Energy-dispersive X-ray Spectroscopy, with its respective atomic numbers and weight percentages.

| Element name | Element symbol | Atomic number | Weight percentage |
|---|---|---|---|
| Carbon | C | 6 | 46.5 |
| Oxygen | O | 8 | 30.9 |
| Aluminum | Al | 13 | 5.8 |
| Silicon | Si | 14 | 2.9 |
| Zinc | Zn | 30 | 13.9 |

Figure 25 shows an EDS spectrum for the PU/Cu-BTC-1.0 membrane and Table 3 gathers the weight percentages of each element detected. Once again, large percentages of carbon (C) and oxygen (O) were found owing to the PU's chemical structure. A significant amount of copper (Cu) was also verified, confirming that the mass observed in the membrane's cross-section corresponds to a Cu-BTC particle. Lastly, the gold (Au) and aluminum (Al) traces detected are due, respectively, to the support material and sputter coating used in the preparation of the SEM samples. Similar results were obtained for all the other masses observed in the cross-section of the PU/Cu-BTC-1.0 membrane.

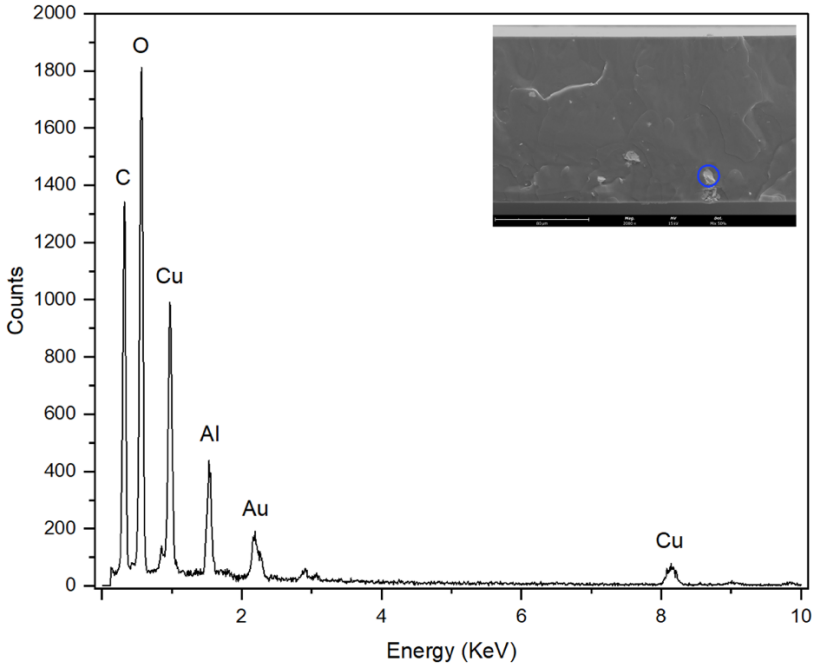


Figure 25. Energy-dispersive X-ray spectrum of the PU/Cu-BTC-1.0 membrane. The inset image shows the region of the SEM sample that was analyzed (circled in blue).

Table 3. Summary of the elements detected in the PU/Cu-BTC-1.0 membrane through Energy-dispersive X-ray Spectroscopy, with its respective atomic numbers and weight percentages.

| Element Name | Element Symbol | Atomic Number | Weight Percentage |
|---|---|---|---|
| Carbon | C | 6 | 32.3 |
| Oxygen | O | 8 | 32.8 |
| Aluminum | Al | 13 | 5.9 |
| Copper | Cu | 29 | 23.2 |
| Gold | Au | 79 | 5.8 |

## 5.3. Attenuated Total Reflectance – Fourier Transform Infrared Spectroscopy

The active layers of all the studied membranes and of the PU prepolymer were analyzed via attenuated total reflectance – Fourier transform infrared spectroscopy (ATR-FTIR). Figures 26 and 27 show the ATR-FTIR spectra (4000-500 $cm^{-1}$) obtained for the pure polyurethane and polyurethane-based membranes, and for the mixed matrix membranes, respectively. The spectrum for the PU prepolymer is displayed for reference in both figures.

Several bands can be identified on the ATR-FTIR spectra of the PU, PU-s, PU/TRIS, PU/CR and PU/MBCD membranes as well as the PU prepolymer: the urethane/urea carbonyl stretching region ($\upsilon$C=O) centered at approximately 1725 $cm^{-1}$, and both urethane C-O-C and ether aliphatic C-O-C asymmetric stretching regions ($\upsilon_{as}$COC) at about 1085 $cm^{-1}$ [33], [34]. However, while all membranes showed the urethane/urea carbonyl stretching band (ca. 1730 $cm^{-1}$), none exhibited a peak for the asymmetric isocyanate stretching mode ($\upsilon_{as}$NCO) centered at 2278 $cm^{-1}$, which is clearly present in the PU prepolymer spectrum (top of Figure 26) [34]. This indicates that all the isocyanate groups are likely to have reacted with the functional groups of other components present in the PU-based compositions (TRIS, CR and MBCD), and with the water present in ambient air (particularly in the PU and PU-s membranes). Consequently, when the reaction occurs with the amine groups, urethane and urea linkages are formed. The wavelengths of the aforementioned bands and of other characteristic peaks observed in PU-based membranes are presented in Table 11 in Appendix C.

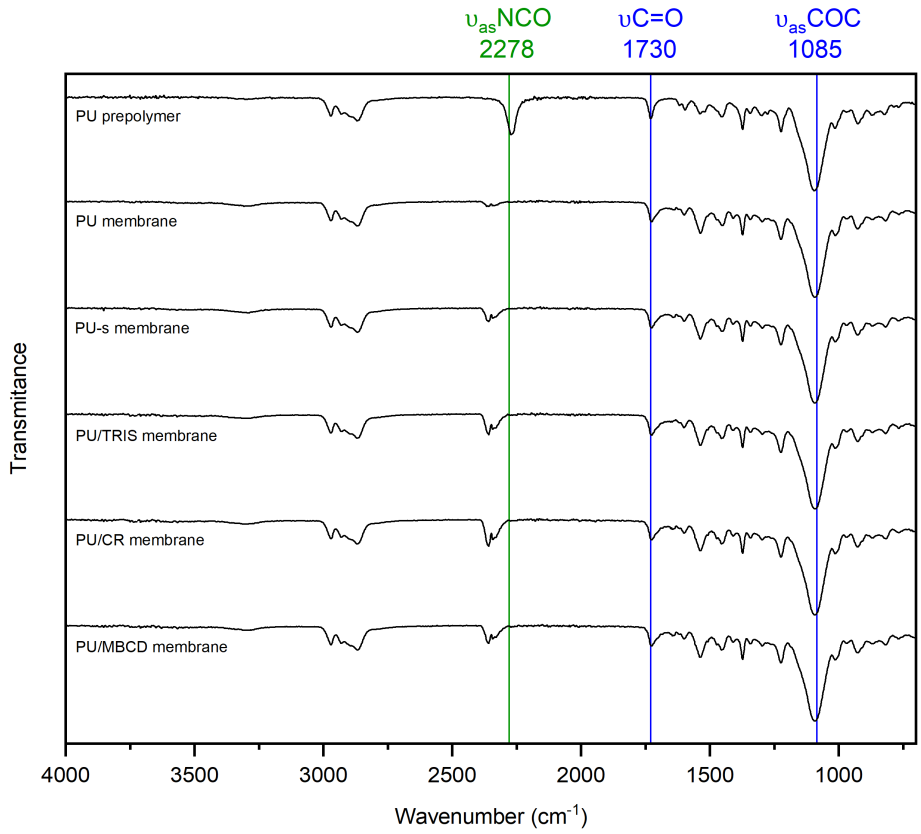


Figure 26. ATR-FTIR spectra of the uncured PU prepolymer and the PU, PU-s, PU/TRIS, PU/CR and PU/MBCD membranes.

It is important to note that the peaks observed at about 2300-2400 $cm^{-1}$ are most likely due to a growing concentration of respiratory $CO_2$ in the room where the FTIR characterization occurred [58].

All the same observations made for the spectra of the PU-based membranes can also be made for the spectra obtained for the MMMs, shown in Figure 27, although, in this case, it is expected that the reactions occur mainly among the PU prepolymer chains themselves or with the water from the atmosphere, rather than between the prepolymer and the MOFs.

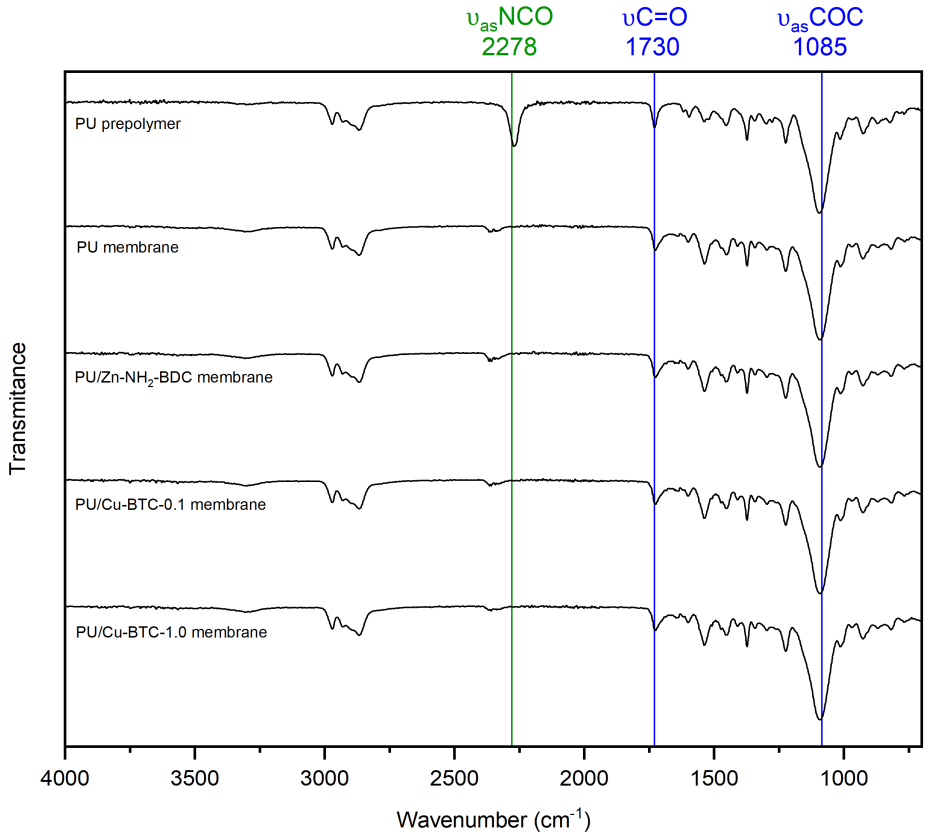


Figure 27. ATR-FTIR spectra of the uncured PU prepolymer and of the PU, PU/Zn-NH2-BDC, PU/Cu-BTC-0.1 and PU/Cu-BTC-1.0 membranes.

A more detailed analysis was performed on the spectra of the PU/TRIS membrane. The spectra obtained for the PU prepolymer, pure TRIS compound and PU/TRIS membrane are displayed in Figure 28. In the spectrum of pure TRIS, a hydroxyl stretching band ($\upsilon$OH) centered at about 3350 $cm^{-1}$ is visible. Additionally, the spectrum of the uncured PU prepolymer shows a strong peak centered at 2278 $cm^{-1}$ corresponding to $\upsilon_{as}$NCO, as seen previously in Figure 26. However, the peaks assigned to $\upsilon$OH and $\upsilon_{as}$NCO are not present in the spectrum of the PU/TRIS membrane, which suggests that all the TRIS hydroxyl groups are likely to have reacted with the isocyanate groups in the prepolymer, forming new urethane groups.

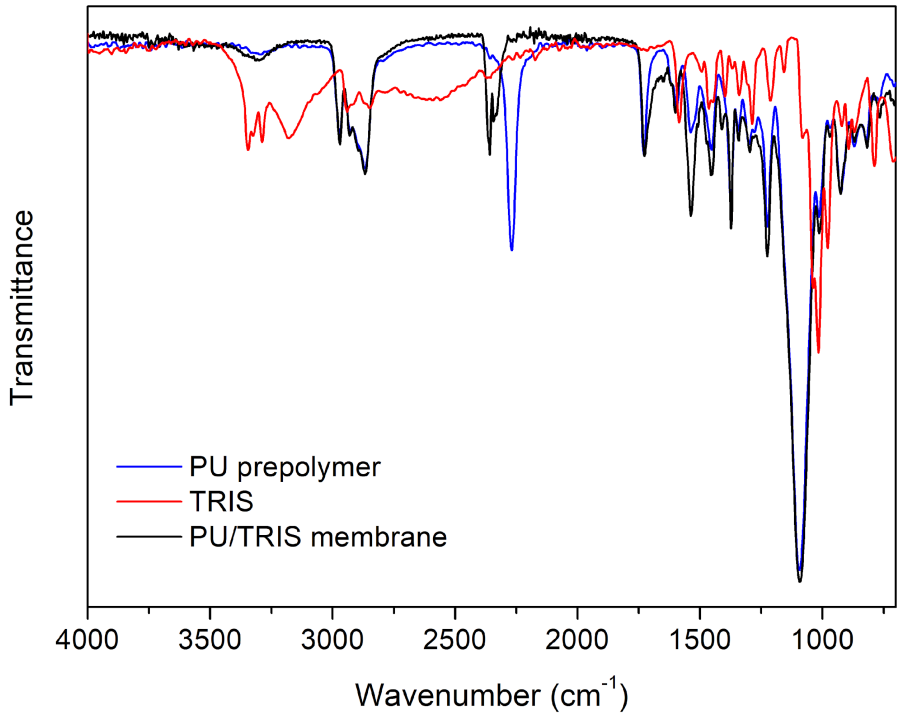


Figure 28. ATR-FTIR spectra of the PU prepolymer, TRIS compound and PU/TRIS membrane.

Although FTIR spectra of the pure CR, MBCD, Zn-NH2-BDC and Cu-BTC were also obtained, no immediate conclusions could be drawn from their comparison with the respective polyurethane-based membranes.

## 5.4. Mechanical Tests

When membranes are held by a supporting material, their mechanical behavior under applied force is not critical. However, in hollow fiber or capillary configurations, the membrane is self-supporting, so when high pressures are applied during gas separation, the mechanical performance becomes important [52]. Therefore, to determine and compare the mechanical properties, uniaxial tensile tests were performed on all the pure polyurethane and polyurethane-based membranes, using a uniform elongation rate of 15 mm/min (0.0041 $s^{-1}$) and specimen gauge length of 60 mm.

Images of the PU, PU-s, PU/TRIS, PU/CR and PU/MBCD test specimens after failure are displayed in Figure 29. All of the specimens included in the analysis ruptured in the neck region and presented clean breaks with no signs of significant permanent deformation before rupture.

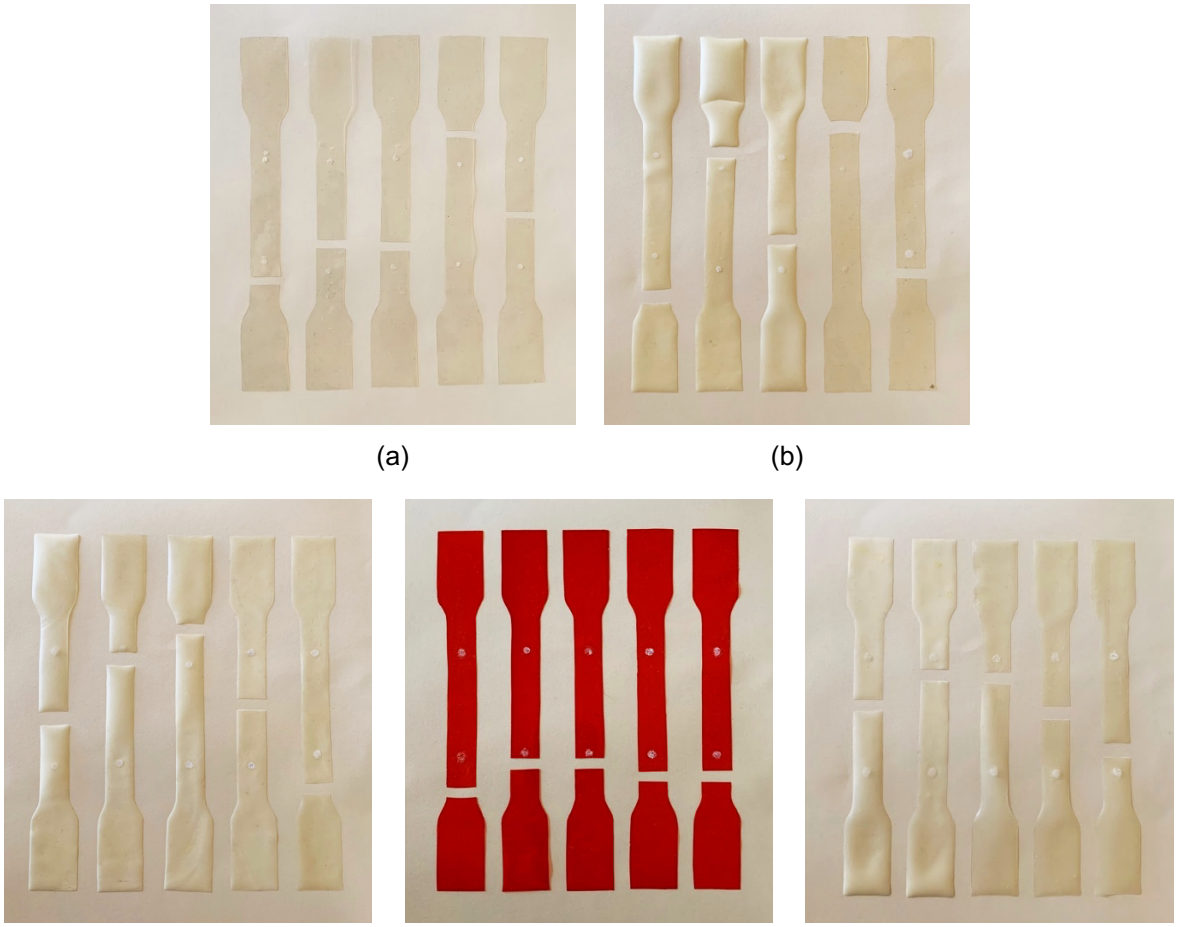


Figure 29. Photographs of the mechanical test specimens after rupture for the following compositions: (a) PU, (b) PU-s, (c) PU/TRIS, (d) PU/CR and (e) PU/MBCD.

Figure 30 shows the engineering stress-strain diagrams obtained for five selected specimens of each tested formulation. All membranes display similar stress-strain behaviors, typical of elastomers, with the initial slope of the curves steadily decreasing as the strain increases, finally reaching a steady slope region. None of the curves present a well-defined yield point, and no clear transition between elastic and plastic regimes can be observed. Again, this is characteristic of rubber-like materials which are known to exhibit high elasticity [59].

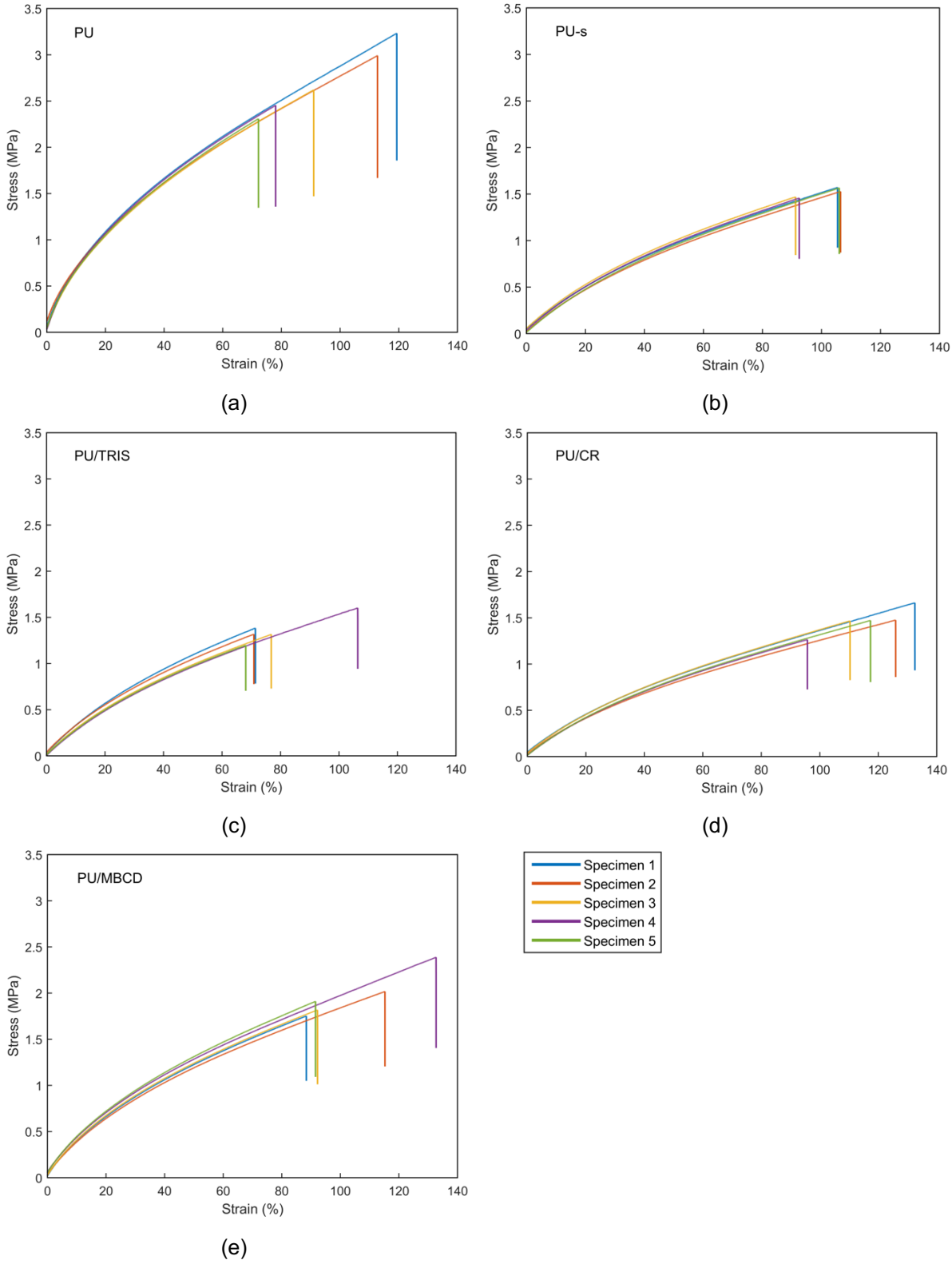


Figure 30. Stress-strain curves obtained for the pure polyurethane and polyurethane-based membranes: (a) PU, (b) PU-s, (c) PU/TRIS, (d) PU/CR and (e) PU/MBCD. Multiple specimens are shown for each composition.

The average values of the Young's modulus (E), tensile strength and elongation at break obtained for each tested formulation are presented in Table 4.

Table 4. Mechanical properties of the pure polyurethane and polyurethane-based membranes, obtained from the tensile tests.

| Membrane | | E (MPa) | Tensile Strength (MPa) | Elongation at Break (%) |
|---|---|---|---|---|
| Group 1 | PU | 8.0 ± 0.4 | 2.7 ± 0.4 | 94.65 ± 20.80 |
| | PU-s | 2.6 ± 0.1 | 1.5 ± 0.1 | 100.31 ± 7.76 |
| Group 2 | PU/TRIS | 3.0 ± 0.2 | 1.4 ± 0.1 | 78.70 ± 15.79 |
| | PU/CR | 2.3 ± 0.1 | 1.5 ± 0.1 | 116.35 ± 14.29 |
| | PU/MBCD | 4.2 ± 0.1 | 2.0 ± 0.3 | 103.99 ± 19.28 |

The Young's modulus, or elastic modulus, is given by the initial slope of the stress-strain curve. It is a measure of the material's stiffness. Generally, elastomers such as polyurethanes are said to be soft materials which sustain large deformations under relatively small forces, as opposed to glassy polymers which are stiffer and require large forces to reach small deformations [52]. Although all the E values presented in Table 4 are relatively low, some differences can be observed for the various compositions. A representation of the E values and respective standard deviations can be found in Figure 31.

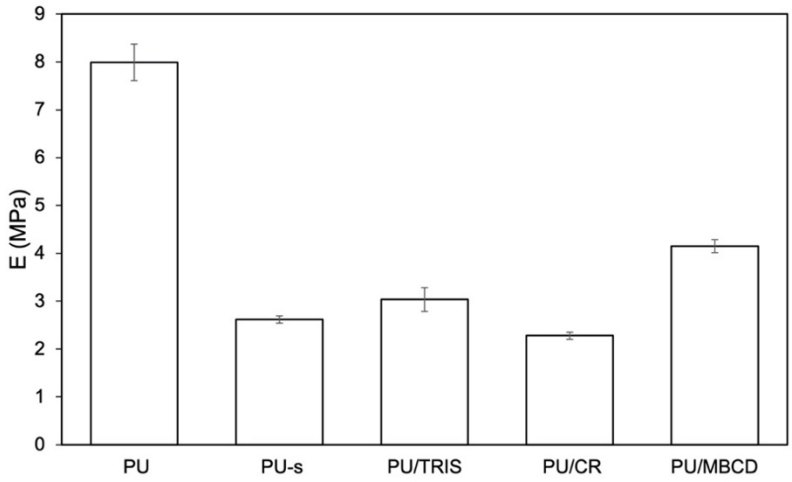


Figure 31. Average Young's moduli (E) and respective standard deviations for the pure polyurethane and polyurethane-based membranes.

Of all compositions, the PU membrane exhibits the highest young's modulus. The lowest E values, obtained for the PU-s, PU/TRIS and PU/CR membranes, are approximately three times lower than the one found for the PU membrane. The PU/MBCD composition presents an intermediate E value, but still significantly lower than the pure PU membrane. This data shows that the loads required to achieve a given level of strain are higher for the PU membrane than for the PU-s membrane and PU-based membranes. It is also important to notice the consistency in the elastic moduli across the different specimens of each membrane, which results in low standard deviations.

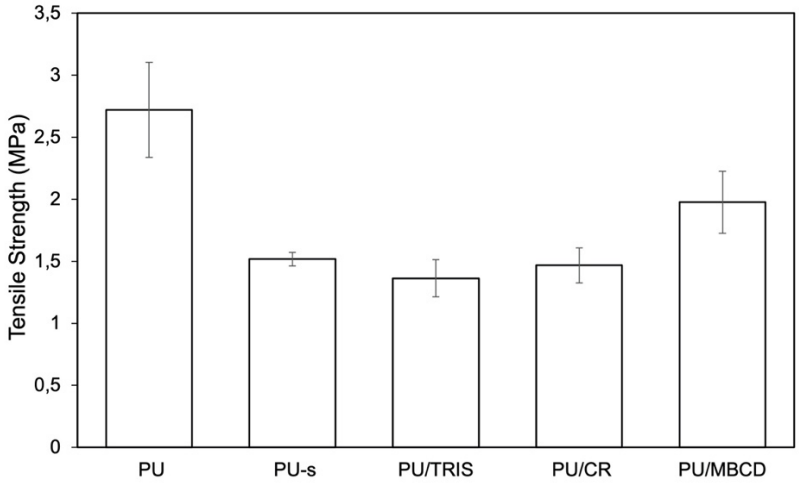


Figure 32. Average tensile strengths and respective standard deviations for the pure polyurethane and polyurethane-based membranes.

The ultimate tensile strength (UTS), or simply tensile strength, is the maximum stress that can be applied to a material [60]. In this case, it coincides with the stress at failure. The UTS results represented in Figure 32 are all within the same order of magnitude, and once again, the PU membrane has the highest tensile strength, followed by the PU/MBCD, and finally the PU-s, PU/TRIS and PU/CR compositions exhibiting similar, lower values.

One factor conceivably contributing towards the reduced E and UTS values observed in the PU-s and PU-based compositions, when compared to the PU membrane, is the preparation method, since their casting solutions undergo two hours of agitation with large proportions of solvent, while the PU membrane is cast directly from the prepolymer. It has been shown that higher degrees of cross-linking in elastomers lead to higher stiffness (and Young's modulus) in deformation [47]. It is possible that the use of solvent in the synthesis of the membranes may have had an impact on the packing of the polymer chains during the cure, causing lower degrees of entanglement and cross-linking, and consequently, lower values of E, than in the PU membrane synthesized without solvent.

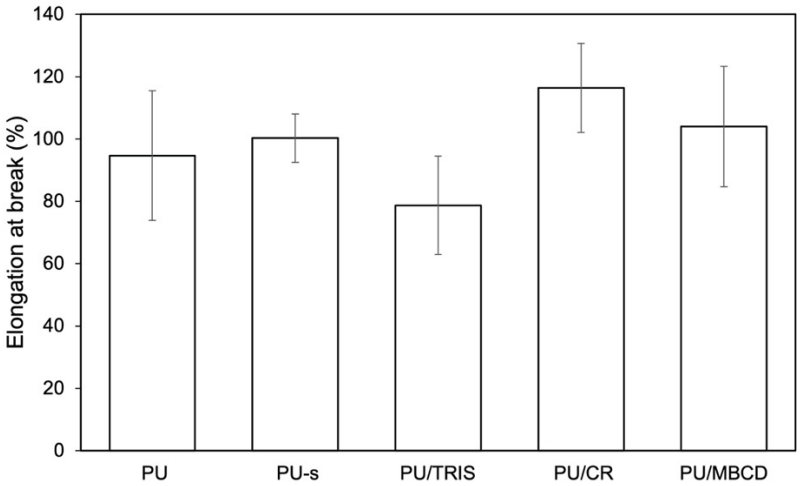


Figure 33. Average elongations at break and respective standard deviations for the pure polyurethane and polyurethane-based membranes.

Another important parameter that can be obtained from the stress-strain diagram is the elongation at break, or the amount of strain (%) under which the material ruptures. The values obtained for the tested formulations are represented in Figure 33. The highest average value was found for the PU/CR composition at 116%. The PU, PU-s and PU/MBCD membranes ruptured at intermediate elongations of 94%, 100% and 103% respectively. Finally, the PU/TRIS specimens ruptured at a significantly lower average elongation of 78%.

Moreover, the elongation at break gives information about the toughness (or brittleness) of the material. A material is said to be brittle if it breaks under a small deformation (about 1 to 2%), or tough if it breaks for big deformations. The relatively high elongations observed for the tested membranes are coherent with the behavior observed in elastomers, which are typically tough. Factors such as the molecular weight, crystallinity and intermolecular forces influence the toughness of the material [52].

## 5.5. Gas permeation experiments

### 5.5.1. Permeate pressure as a function of time

A series of gas permeation experiments were conducted on all the synthesized membranes using the set-up described in section 4.4.2. In each test, pure $CO_2$ or $O_2$ gas was fed through a 9.62cm$^2$ membrane sample and the variation of permeate pressure in the receiving chamber was recorded as a function of time.

Figure 34 shows an example of the $CO_2$ and $O_2$ permeation curves, recorded at a feed pressure ($p_f$) of 3 bar, for the pure PU and PU-s membranes. Similar curves were obtained for both compositions at multiple feed pressures, varying between 1.5 and 4 bar.

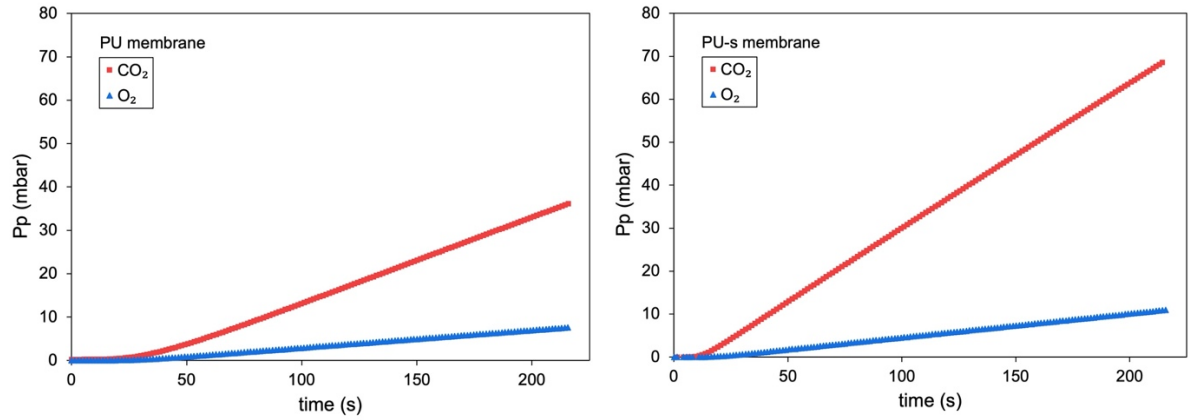


(a) (b)

Figure 34. Permeate pressure ($p_p$) vs. time (t) of $CO_2$ and $O_2$ gases ($p_f$=3 bar) for the pure polyurethane membranes: a) PU and b) PU-s.

It is important to note that, while both PU-s* and PU-s membranes were tested for $CO_2$ permeation, only the PU-s could be tested for $O_2$ permeation, due an insufficient number of samples of PU-s* (from a lack of reproducibility). However, the results obtained for the $CO_2$ permeation through the PU-s* were very similar to the ones obtained through the PU-s. For this reason, it is assumed that they have similar behaviors when it comes to $O_2$ permeation as well, and only the PU-s membrane was considered for the remainder of the discussion in this work.

Two distinct regions can be identified in the permeation curves presented in Figure 34. The first region, usually under 40s, corresponds to the transient state, in which the permeate pressure remains constant through time. The second region, known as the steady state region, is marked by a gradual increase of the permeate pressure with time. For both pure PU membranes from group 1, and at similar feed pressures, the slope of the steady state region of the curves is steeper for $CO_2$ than for $O_2$, which is typical in this type of membrane. Furthermore, higher $CO_2$ and $O_2$ permeate pressures are achieved for the PU-s membrane than for the PU membrane.

Similar permeation curves were also obtained for all the PU-based membranes (group 2) at multiple feed pressures. An example of these permeation curves at a feed pressure of 3 bar is displayed in Figure 35.

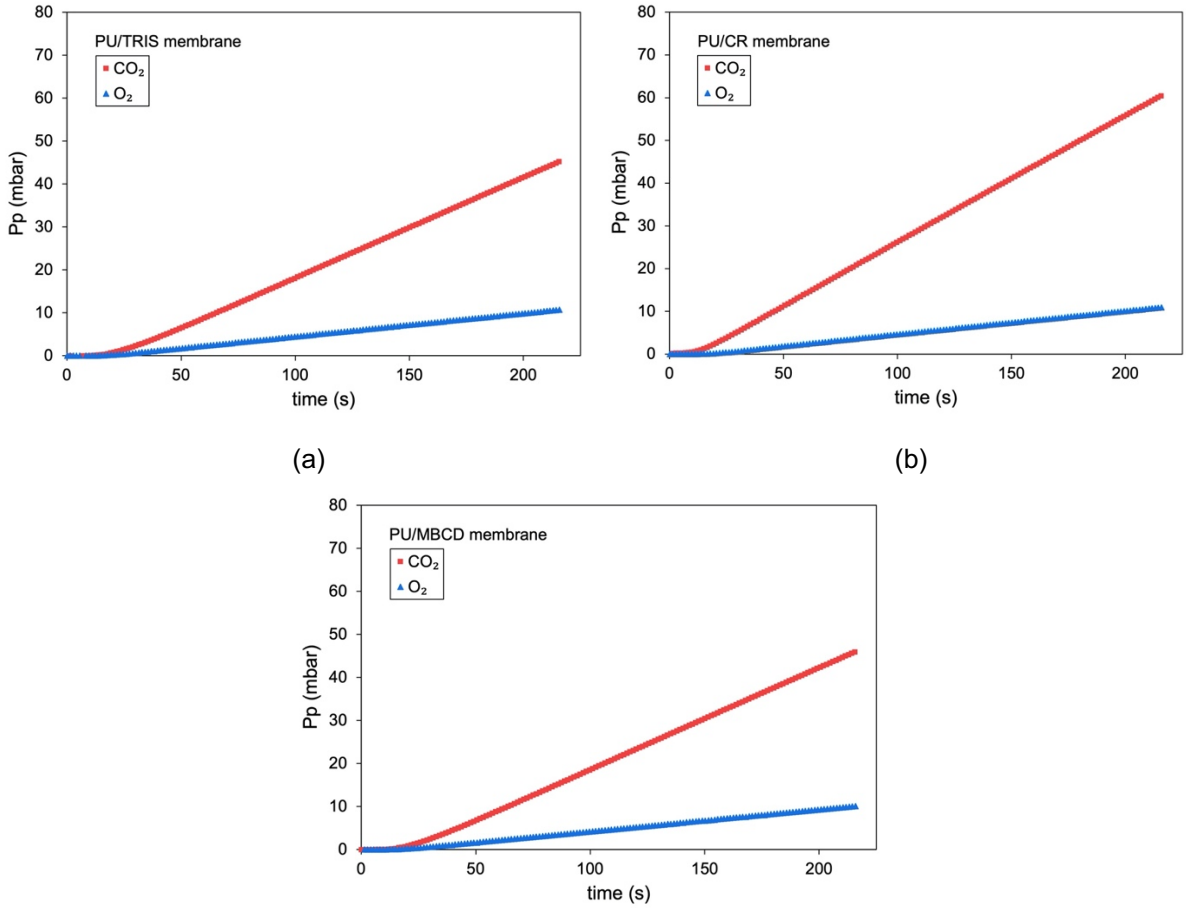


Figure 35. Permeate pressure ($p_p$) vs. time (t) of $CO_2$ and $O_2$ gases (at $p_f$=3 bar) for the polyurethane-based membranes: a) PU/TRIS, b) PU/CR, and c) PU/MBCD.

Once more, the permeate pressures achieved are higher for $CO_2$ than for $O_2$ in every PU-based membrane. The slopes of the steady state region for all PU-based formulations fall between the slopes obtained for the PU and PU-s membranes, with PU/CR presenting a significantly higher slope than the PU/TRIS and PU/MBCD membranes.

Finally, Figure 36 shows the evolution of the permeate pressure of $CO_2$ and $O_2$ with time for all the mixed matrix membranes (group 3), once again at a feed pressure of 3 bar. All compositions demonstrated similar permeation behaviors at multiple feed pressures.

The same conclusions can be drawn from the permeation curves of the MMMs as for the PU-based membranes, regarding their behavior in comparison with the PU and PU-s membranes. However, no significant differences can be observed among the steady state slopes of the three MMMs.

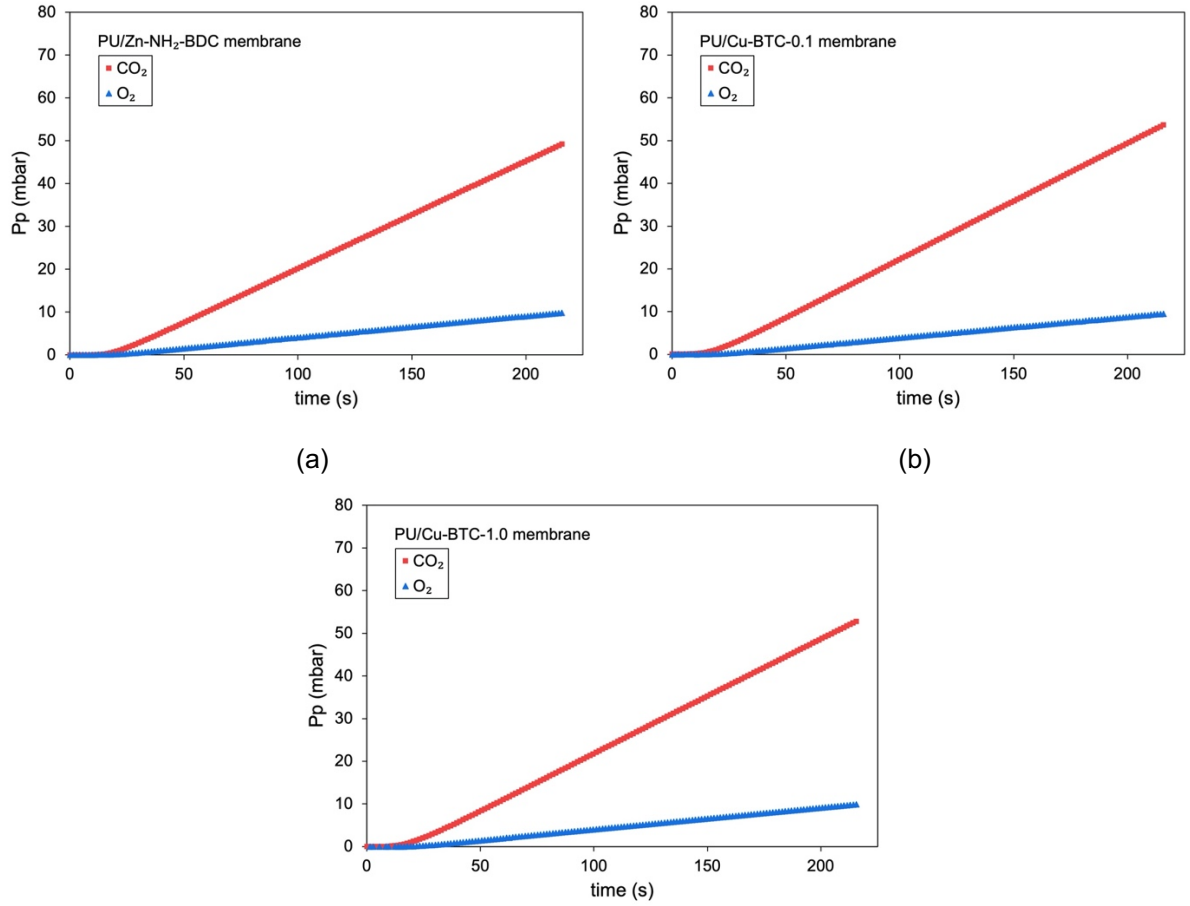


Figure 36. Permeate pressure ($p_p$) vs. time (t) of $CO_2$ and $O_2$ gases (at $p_f$=3 bar) for the mixed matrix membranes: a) PU/Zn-NH2-BDC, b) PU/Cu-BTC-0.1, c) PU/Cu-BTC-1.0.

### 5.5.2. Volumetric flux as a function of the transmembrane pressure

The curves obtained from permeation experiments are commonly used to determine the volumetric flux of gas through the studied membrane. First, the Ideal Gas Law is used to convert the steady state region's slope, $\frac{dp_p}{dt}$, of each permeation curve into molar flow, $\frac{dn}{dt}$:

$$\frac{dn}{dt} = \frac{dp_p}{dt} \cdot \frac{V_s}{RT} \tag{19}$$

where $V_s$ is the receiving chamber's volume, $R$ is the ideal gas constant and $T$ is the absolute temperature at which the tests were carried out. The Ideal Gas Law was found to be a reasonable approximation to the behavior of gases in the experimental conditions used (low pressure and moderately high temperature).

The obtained molar flow is subsequently transformed to volumetric flow, $\frac{dV}{dt}$, at STP conditions:

$$\frac{dV}{dt} = \frac{dn}{dt} \cdot \frac{RT_{STP}}{p_{STP}} \tag{20}$$

where $T_{STP}$ and $p_{STP}$ are the temperature and pressure in STP conditions, which correspond to 273.15 K and 1 atm respectively. Equation (19) is then substituted in equation (20), resulting in the following expression:

$$\frac{dV}{dt} = \frac{dp_p}{dt} \cdot \frac{V_s T_{STP}}{T p_{STP}} \tag{21}$$

Finally, the volumetric flow is divided by the effective membrane area, $A$, to calculate the volumetric flux, $J$ [26]:

$$J = \frac{dV}{dt} \cdot \frac{1}{A} \tag{22}$$

Since the permeation curves of $CO_2$ and $O_2$ were obtained at several feed pressures for each membrane sample, it was possible to plot the evolution of the volumetric flux with the transmembrane pressure, TMP. In each experiment, the TMP was calculated by subtracting the initial permeate pressure, $p_{pi}$, from the average feed pressure, $p_f$:

$$TMP = p_f - p_{pi} \tag{23}$$

Figure 37 shows the steady-state volumetric flux, $J$, of $CO_2$ and $O_2$ as a function of the TMP for all pure PU and PU-based membranes. The results for the PU-based membranes are displayed together with the PU-s membrane because all of them were synthesized using the same solvent content of 35wt%. The pure PU membrane (with no solvent) is also included for comparison.

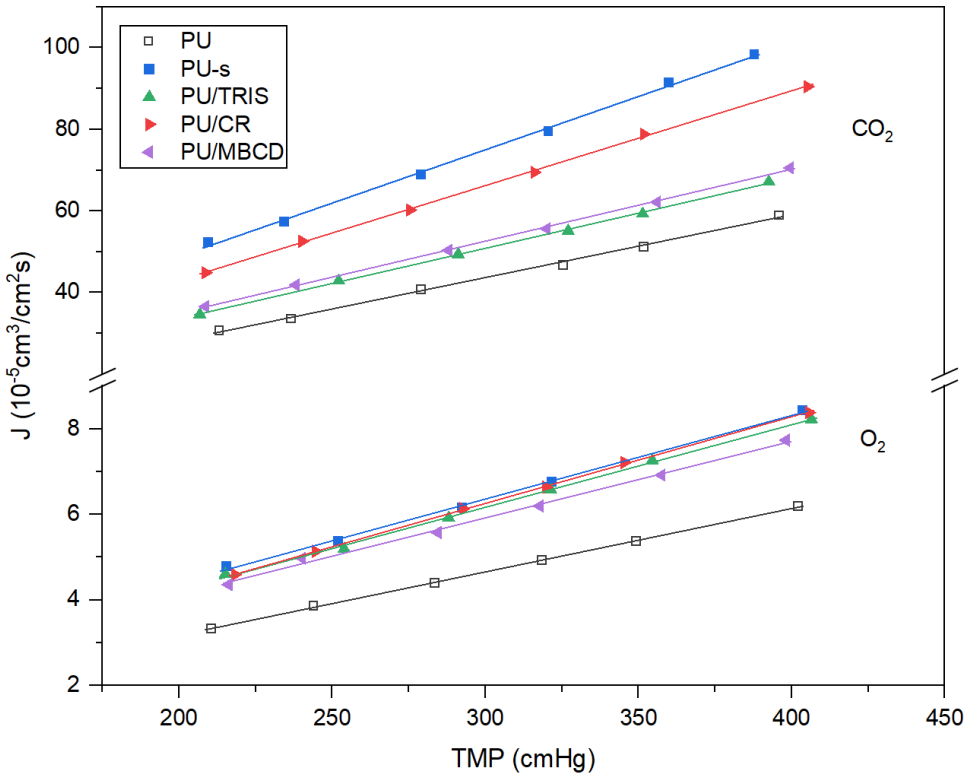


Figure 37. $CO_2$ and $O_2$ volumetric fluxes (J) versus the transmembrane pressure (TMP) for the pure polyurethane and polyurethane-based membranes: a) PU, b) PU-s, c) PU/TRIS, d) PU/CR, e) PU/MBCD.

In every composition, the volumetric flux increases linearly with the TMP and is one order of magnitude greater for $CO_2$ than for $O_2$. For both gases, the lowest fluxes were always measured for the

pure PU membrane (with no solvent) and the highest fluxes for the PU-s membrane. All the polyurethane-based membranes present with intermediate flux values, always falling in between the PU and PU-s plots for $CO_2$ and $O_2$. When comparing the results obtained within the PU-based membranes, the $CO_2$ flux through the PU/CR membrane is significantly higher than for the PU/TRIS and PU/MBCD membranes. The same tendency is also observed for $O_2$, albeit to a lesser extent.

One important comment to make is that the flux values are heavily dependent on the membrane thickness: the thinner the membrane, the larger the flux of gas through it. The membranes just described have significantly different thicknesses, as demonstrated by the SEM images, increasing in the following order: PU-s, PU-based and pure PU membranes. This is coherent with the tendency previously observed for the flux values of these membranes.

The same analysis was implemented on the data from the permeation curves of $CO_2$ and $O_2$ through the mixed matrix membranes. The plots of the volumetric fluxes as a function of the TMP for the PU/Zn-$NH_2$-BDC, PU/Cu-BTC-0.1 and PU/ Cu-BTC-1.0. are shown in Figure 38. The pure PU membrane is also included in this figure as a reference, since the solvent content in the MMMs is low (10wt%).

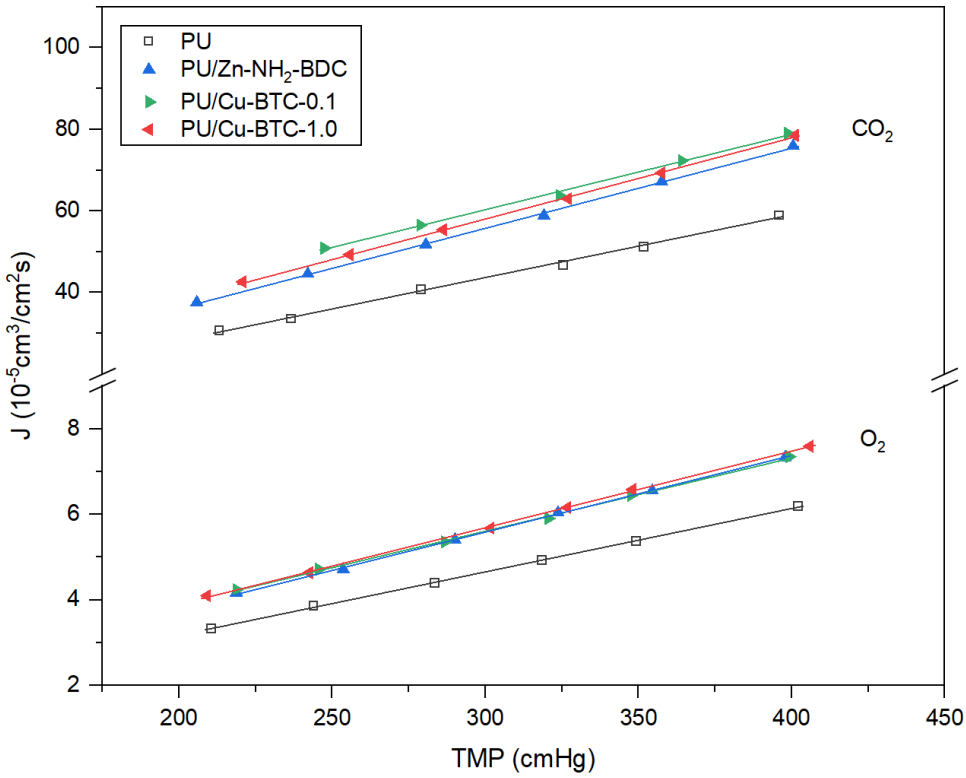


Figure 38. $CO_2$ and $O_2$ volumetric fluxes (J) versus the transmembrane pressure (TMP) for the pure polyurethane and mixed matrix membranes: a) PU, b) PU/Zn-$NH_2$-BDC, c) PU/Cu-BTC-0.1, d) PU/ Cu-BTC-1.0.

The trends observed in this graph are similar to the ones previously described for the other membrane groups. For each composition, the flux values are higher for $CO_2$ than for $O_2$ and they increase with the TMP in a linear fashion. All three MMMs present higher fluxes for both gases than the pure PU membrane. For $CO_2$, the highest flux is seen for the PU/Cu-BTC-0.1 composition, followed by the PU/ Cu-BTC-1.0 and PU/Zn-$NH_2$-BDC compositions. For $O_2$, the plots of all three MMMs seem to overlap, and no particular order can be distinguished among them. Once again, these results do not

account for the differences in thickness, so further data analysis is necessary to draw meaningful conclusions.

### 5.5.3. Permeances and permeability coefficients

For every membrane sample, the permeance of each single pure gas, $perm$, can be determined from the slope of its volumetric flux vs. TMP plot:

$$perm = \frac{dJ}{d(TMP)}\left[\frac{cm^3(STP)}{cm^2 s\ cmHg}\right] \quad (24)$$

Since the permeance values depend greatly on the thickness of the membrane, for comparison purposes, it is common to convert them to permeability coefficients, $P$, which are determined by:

$$P = perm \times \ell \times 10^{10}\ [Barrer] \quad (25)$$

where $\ell$ is the membrane's thickness.

Several (up to six) samples of each composition were tested for each pure gas. The average values, and respective standard deviations, obtained for the permeances and permeability coefficients of $CO_2$ and $O_2$ through each studied membrane are reported in Table 5. A visual representation of the permeability coefficients can be found in Figure 39.

Table 5. Average $CO_2$ and $O_2$ permeances (Perm) and permeability coefficients (P) with respective standard deviations for all the studied membranes.

| | | **$CO_2$** | | **$O_2$** | |
|---|---|---|---|---|---|
| **Membrane** | | **Perm** $\left(\frac{10^{-5}cm^3(STP)}{cm^2\ s\ cmHg}\right)$ | **P (Barrer)** | **Perm** $\left(\frac{10^{-5}cm^3(STP)}{cm^2\ s\ cmHg}\right)$ | **P (Barrer)** |
| Group 1 | PU | 0.151 | 273 ± 8.5 | 0.0148 | 27 ± 1.3 |
| | PU-s | 0.251 | 278 ± 21.4 | 0.0191 | 24 ± 2.9 |
| Group 2 | PU/TRIS | 0.173 | 237 ± 22.6 | 0.0193 | 26 ± 1.2 |
| | PU/CR | 0.232 | 346 ± 25.9 | 0.0200 | 30 ± 2.5 |
| | PU/MBCD | 0.174 | 251 ± 17.5 | 0.0181 | 26 ± 1.7 |
| Group 3 | PU/ Zn-$NH_2$-BDC | 0.196 | 297 ± 6.5 | 0.0180 | 27 ± 0.7 |
| | PU/Cu-BTC-0.1 | 0.187 | 287 ± 25.4 | 0.0171 | 26 ± 0.7 |
| | PU/Cu-BTC-1.0 | 0.196 | 280 ± 4.1 | 0.0179 | 26 ± 1.6 |

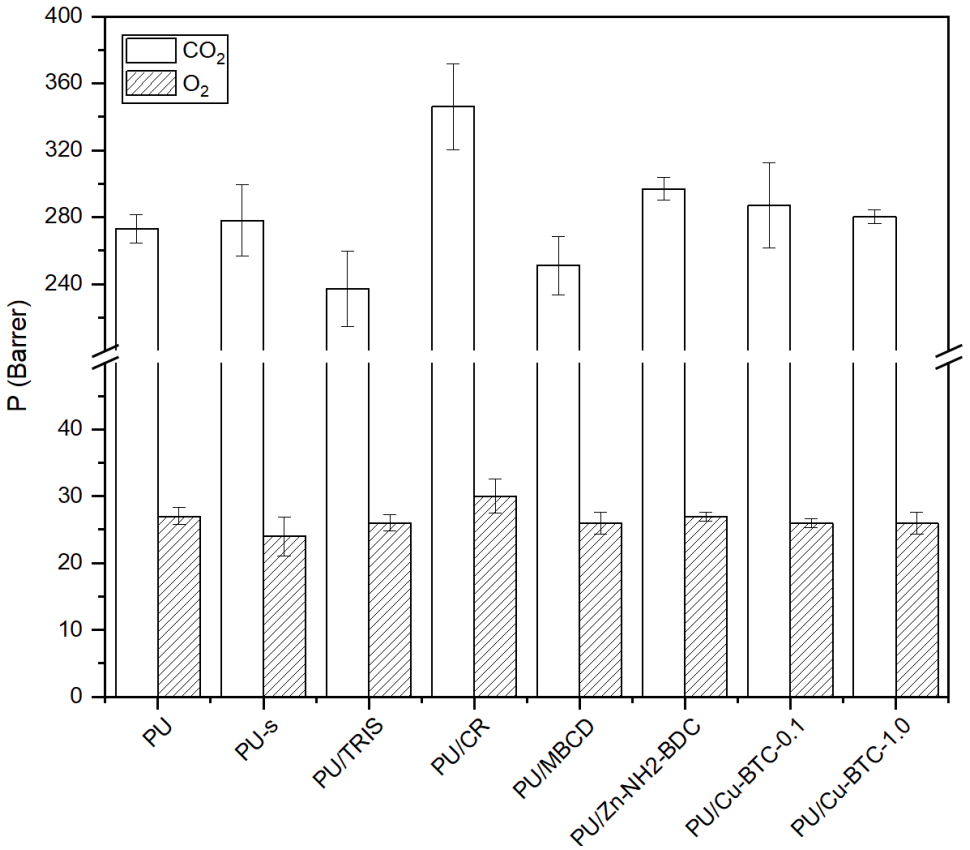


Figure 39. Average permeability coefficients (P) towards $CO_2$ and $O_2$, and respective standard deviations, for all the studied membranes.

From the data shown in Table 5 and Figure 39, the same trend can be observed as for the parameters discussed previously, with the permeances and permeability coefficients for all compositions being approximately 10 times higher towards $CO_2$ than towards $O_2$. In general, the tendencies observed amongst the permeances of the various compositions are sometimes different from the tendencies observed between the permeability coefficients. This is because the permeability coefficient takes into account the thickness of the membrane and the permeance does not. Since all the membranes have different thicknesses, the P values are more useful for comparison.

Concerning the pure polyurethane membranes from group 1, the P values for $CO_2$ ($P_{CO2}$) are higher for the PU-s membrane (278 Barrer) than for the PU membrane (273 Barrer), although the difference is not substantial. However, in the case of $O_2$, the P values ($P_{O2}$) are lower for the PU-s membrane (24 Barrer) than for than for the PU membrane (27 Barrer). In terms of oxygen permeation, it seems that the use of solvent during the synthesis of the nonporous PU-s membranes did not provide any advantage.

A composition similar to the PU-s membrane was studied by Eusebio et. al [26] and the $P_{CO2}$ and $P_{O2}$ values found were 227 and 24 Barrer, respectively. Martins [61] also reported $P_{CO2}$ and $P_{O2}$ values of 230 and 22.9 Barrer for pure polyurethane nonporous symmetric membranes synthesized with 35 wt% solvent. Although the $P_{O2}$ values obtained for PU-s in this work were similar to the ones found in previous studies, the $P_{CO2}$ values are considerably higher.

Among the polyurethane-based compositions from group 2, the PU/CR membrane presents the highest values of both $P_{CO2}$ and $P_{O2}$, at 346 Barrer and 30 Barrer respectively. These values are

significantly higher than the ones obtained for the pure polyurethane membranes. On the other hand, the PU/TRIS and PU/MBCD membranes demonstrated lower $P_{CO2}$ values (of 237 and 251 Barrer respectively) than the pure PU membranes. The same $P_{O2}$ value of 26 Barrer was obtained for both these compositions, which in terms of $O_2$ permeability rank below the PU membrane, but above the PU-s membrane.

In previous research, polyurethane-based membranes with varying quantities (0-15wt%) of polycaprolactone (PCL) were extensively investigated. The $P_{CO2}$ results reported by Faria et. al [33] for PU/PCL membranes, between 113 and 337 Barrer, were comparable to the PU-based formulations studied in this work, but the $P_{O2}$ results were significantly lower, at 10 to 11 Barrer. Improved $P_{O2}$ values of 21 Barrer were obtained by Pon [56] for similar nonporous symmetric membranes PU/PCL membranes, even though the $P_{CO2}$ values were not as high, between 202 and 208 Barrer. Still, all the polyurethane-based membranes investigated in this work presented better $O_2$ permeability coefficients than in the mentioned previous studies.

All the mixed matrix membranes from group 3 exhibit higher $P_{CO2}$ values than the pure polyurethane membranes, with the PU/Zn-$NH_2$-BDC membrane (which has 0.1% MOF content) having the highest value of the group (297 Barrer). Within the PU/Cu-BTC membranes, the increase in MOF content from 0.1 wt% to 1.0wt% is accompanied by a decrease of the $P_{CO2}$ value from 287 to 280 Barrer. The highest $P_{O2}$ among the MMM group is found, once again, for the PU/Zn-$NH_2$-BDC membrane at 27 Barrer, which is approximately the same as the value measured in the PU membrane. A lower $P_{O2}$ value of 26 Barrer was obtained for both PU/Cu-BTC-0.1 and PU/Cu-BTC-1.0 membranes, suggesting that the increase in Cu-BTC content had no impact on its $O_2$ permeability.

Some studies concerning mixed matrix membranes have found that incompatibilities between the filler and matrix materials, such as voids or rigidification of the polymer chains in the interfacial region, have a profound effect on their permeation properties [62], [63]. It is possible that the increase in Cu-BTC content (from 0.1 to 1.0 wt%) may have contributed to a higher degree of incompatibility between the MOFs and the polyurethane matrix, creating a resistance to the diffusion of permeating species, thus resulting in lower (or unimproved) permeability values for the PU/Cu-BTC-1.0 membrane.

Overall, the novel composition showing the most promising results for the permeation of both $CO_2$ and $O_2$ gases is the PU/CR membrane. The PU/TRIS and PU/MBCD membranes seem to provide no improvement to the permeation of either of the studied gases when compared to the pure PU membrane. Regarding the MMMs, although no significant improvement was achieved for the permeation of $O_2$, the enhanced permeability coefficients found for $CO_2$ are encouraging.

Furthermore, the results obtained for all the PU membranes in this work represent an improvement when compared to other membrane materials used in current artificial lungs, including polypropylene (PP) and polymethylpentene (PMP), which present respective permeability coefficients of 9 and 90 Barrer for $CO_2$, and 2 and 30 Barrer for $O_2$ [64]. However, the measurements just mentioned were obtained in a gas/membrane/liquid system, while the experiments in this work were carried out on a gas/membrane/gas system, in which the resistance to gas transport is lower. A more direct comparison could therefore be achieved by repeating the permeation tests done in this work on a gas/membrane/liquid system.

### 5.5.4. Commercial membrane

A sample of the commercial membrane (CM) was subjected to gas permeation experiments in order to compare its performance to the one of the studied membranes. Figure 40 shows an example of the permeate curves obtained of $CO_2$ and $O_2$ through the CM, at a feed pressure of 3 bar. Similar curves were obtained at various other feed pressures, ranging from 1.5 to 4 bar.

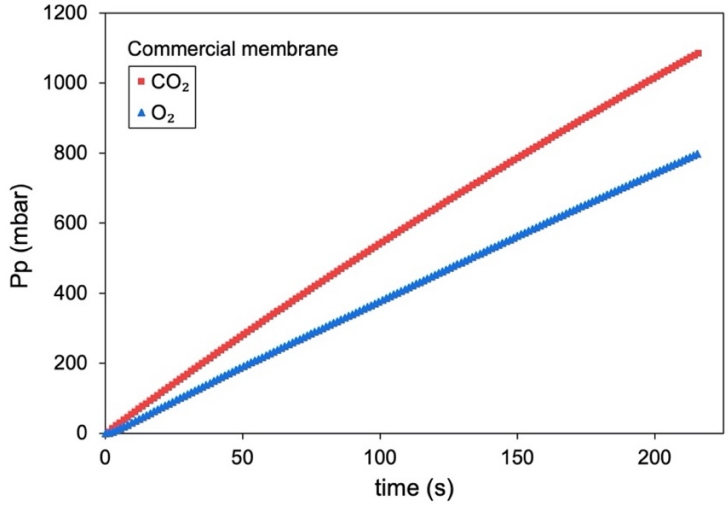


Figure 40. Permeate pressure (pp) vs. time (t) of $CO_2$ and $O_2$ gases (pf=3 bar) for the commercial membrane.

The plots of the $CO_2$ and $O_2$ volumetric fluxes as a function of the TMP for the commercial membrane are exhibited in Figure 41, and the resulting permeances and permeability coefficients for both gases are presented in Table 6.

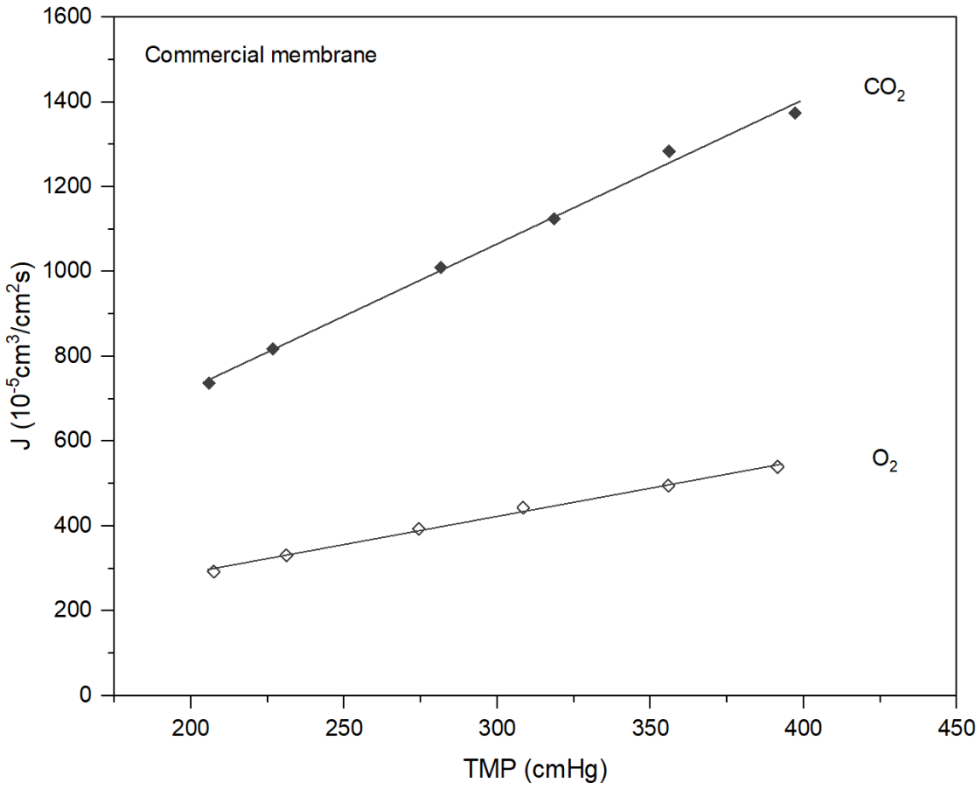


Figure 41. $CO_2$ and $O_2$ volumetric fluxes (J) versus the transmembrane pressure (TMP) for the commercial membrane.

Table 6. Membrane thickness ($\ell$) with respective standard deviation, permeance (Perm) and permeability coefficient (P) values obtained for $CO_2$ and $O_2$ through a sample of the commercial membrane.

| | **Thickness, $\ell$ (μm)** | **Perm** $\left(\frac{10^{-5} cm^3 (STP)}{cm^2\ s\ cmHg}\right)$ | **P (Barrer)** |
|---|---|---|---|
| $CO_2$ | 66 ± 1.2 | 3.40 | 2245 |
| $O_2$ | 66 ± 1.2 | 1.33 | 881 |

The permeance values obtained for the CM were 3.40x10$^{-5}$ cm$^3$/cm$^2$s.cmHg for $CO_2$ and 1.33x10$^{-5}$ cm$^3$/cm$^2$s.cmHg for $O_2$, which are an order of magnitude greater than the values necessary for an efficient MBO (0.22x10$^{-5}$ cm$^3$/cm$^2$s.cmHg for $CO_2$ and 0.27x10$^{-5}$ cm$^3$/cm$^2$s.cmHg for $O_2$) [45]. The permeability coefficients presented for the CM (2245 and 881 Barrer for $CO_2$ and $O_2$, respectively) are also significantly higher than the ranges obtained for the novel membranes studied in this work (237-346 Barrer for $CO_2$ and 24-30 Barrer for $O_2$). It is important to note that even though the commercial membrane exhibits better permeation properties, polyurethane-based membranes have demonstrated superior hemocompatibility in past studies [65].

One important point to make is that, while the results presented in Table 6 were obtained in a gas/membrane/gas set-up, the commercial MBO is a gas/membrane/liquid system, in which the presence of blood represents an additional resistance to gas transport. It is therefore plausible to consider that the permeance values obtained for the CM in this work are equivalent to the values reported by the membrane manufacturer, without taking into consideration the additional resistance to gas permeation posed by the blood.

### 5.5.5. $CO_2/O_2$ selectivities

By substituting the obtained $CO_2$ and $O_2$ average permeability coefficients in equation (9), it was possible to calculate the $CO_2/O_2$ selectivity of each membrane. The results obtained are presented in Table 7.

Table 7. $CO_2/O_2$ selectivity ($\alpha$) for all the studied membranes.

| | **Membrane** | **α $CO_2/O_2$** |
|---|---|---|
| Group 1 | PU | 10.2 |
| | PU-s | 11.6 |
| Group 2 | PU/TRIS | 9.0 |
| | PU/CR | 11.6 |
| | PU/MBCD | 9.6 |
| Group 3 | PU/Zn-$NH_2$-BDC | 10.9 |
| | PU/Cu-BTC-0.1 | 10.9 |
| | PU/Cu-BTC-1.0 | 11.0 |

Typically, for a given gas, a high permeability coefficient corresponds to a low selectivity [11]. This is not the tendency observed when comparing the results from Table 5Table 7. The membranes with the lowest $P_{CO2}$ values, PU/TRIS and PU/MBCD, are also the ones with lowest $CO_2/O_2$ selectivity. The PU/CR membrane has both the highest $P_{CO2}$ and highest $\alpha$ values. Finally, the PU membrane and all the MMMs from group 3 have intermediate permeabilities and selectivities. The only outlier is the PU-s membrane which presents one of the highest selectivities, but just an intermediate permeability coefficient. Generally, this data suggests that, for the studied formulations, improved permeabilities are accompanied by enhanced $CO_2/O_2$ selectivities.

### 5.5.6. Total Surface Area required

As described in section 1.2, the efficient gas exchange in an MBO involves the removal of $CO_2$ at about 200 $cm^3$ (STP)/min and delivery of $O_2$ at approximately 250 $cm^3$ (STP)/min [7]. The membranes currently used in blood oxygenators commonly have a surface area between 2 to 6 $m^2$ [64]. Estimations for the surface area required of each membrane to meet these specifications were calculated from the linear flux versus TMP plots like the ones exhibited in Figure 37 and 38 (for a feed pressure of 2.0 bar). The values obtained are presented in Table 8.

Table 8. Volumetric fluxes and estimated required membrane surface areas for all formulations.

| | | **$CO_2$** | | **$O_2$** | |
|---|---|---|---|---|---|
| **Membrane** | | **J** $\left(\frac{10^{-5} cm^3}{cm^2\ s}\right)$ | **A** $(m^2)$ | **J** $\left(\frac{10^{-5} cm^3}{cm^2\ s}\right)$ | **A** $(m^2)$ |
| Group 1 | PU | 33.6 | 1.0 | 3.9 | 10.8 |
| | PU-s | 57.4 | 0.6 | 5.4 | 7.8 |
| Group 2 | PU/TRIS | 42.9 | 0.8 | 5.2 | 8.0 |
| | PU/CR | 52.6 | 0.6 | 5.1 | 8.1 |
| | PU/MBCD | 41.9 | 0.8 | 5.0 | 8.4 |
| Group 3 | PU/ Zn-$NH_2$-BDC | 44.6 | 0.7 | 4.7 | 8.8 |
| | PU/Cu-BTC-0.1 | 50.9 | 0.7 | 4.7 | 8.8 |
| | PU/Cu-BTC-1.0 | 49.3 | 0.7 | 4.6 | 9.0 |

As anticipated, higher fluxes of gas across the membranes are correlated to lower required surface areas. In fact, because the fluxes are significantly higher for $CO_2$ than for $O_2$, the necessary transfer areas for $CO_2$ are much lower than for $O_2$.

The required surface areas obtained in this work ranged from 0.6 to 1.0 $m^2$ for $CO^2$ and from 7.8 to 10.8 $m^2$ for $O^2$, which represent an improvement when compared to the values reported by Martins [61] for PU/PCL membranes, of 1.2-1.7 $m^2$ for $CO^2$ and 13.5-17.5 $m^2$ for $O^2$. This is consistent with the enhanced permeability coefficients achieved for $CO_2$ and $O_2$ in this work. Nonetheless, the minimum surface areas obtained for oxygen still exceed the range found in membranes for commercial blood oxygenators.

### 5.5.7. Diffusion and Solubility Coefficients

Further analysis of the gas permeation measurements, through the time lag method described in section 4.4.1.2, allowed for the estimation of the diffusion and solubility coefficients for all the studied membranes.

First, the asymptote of the steady state region of the permeation curve is traced. The value at which the steady state asymptote intercepts the $x$ axis (time axis) is defined as the time lag ($t_{lag}$). The time lag value and permeability coefficient obtained are then used to determine the D and S coefficients of the membrane, through equations (18) and (1) respectively. This same procedure was applied for all compositions. The values of $t_{lag}$, $D$ and $S$ obtained for each membrane towards $O_2$ and $CO_2$ are displayed in Table 9.

Table 9. Time lag values ($t_{lag}$) diffusion coefficients (D) and solubility coefficients (S) obtained from the $O_2$ and $CO_2$ permeation curves for all the studied membranes.

| | | $CO_2$ | | | $O_2$ | | |
|---|---|---|---|---|---|---|---|
| **Membrane** | | **$t_{lag}$ (s)** | **D** $\left(\frac{10^{-6}cm^2}{s}\right)$ | **S** $\left(\frac{10^{-4}cm^3}{cm^3cmHg}\right)$ | **$t_{lag}$ (s)** | **D** $\left(\frac{10^{-6}cm^2}{s}\right)$ | **S** $\left(\frac{10^{-4}cm^3}{cm^3cmHg}\right)$ |
| Group 1 | PU | 37.2 | 1.5 ± 0.1 | 185.5 ± 9.6 | 27.4 | 2.0 ± 0.2 | 13.4 ± 1.0 |
| | PU-s | 11.5 | 1.8 ± 0.4 | 154.6 ± 26.9 | 18.2 | 1.5 ± 0.3 | 16.6 ± 3.2 |
| Group 2 | PU/TRIS | 22.2 | 1.4 ± 0.2 | 168.3 ± 22.8 | 14.7 | 2.2 ± 0.4 | 12.3 ± 1.7 |
| | PU/CR | 12.4 | 3.1 ± 0.6 | 114.5 ± 15.2 | 14.7 | 2.6 ± 0.6 | 11.7 ± 1.8 |
| | PU/MBCD | 25.6 | 1.5 ± 0.4 | 183.0 ± 50.9 | 15.3 | 2.3 ± 0.4 | 11.4 ± 1.6 |
| Group 3 | PU/ Zn-$NH_2$-BDC | 18.6 | 2.1 ± 0.1 | 144.3 ± 4.7 | 212 | 1.8 ± 0.1 | 15.0 ± 0.3 |
| | PU/Cu-BTC-0.1 | 21.0 | 1.9 ± 0.2 | 153.6 ± 25.2 | 20.4 | 1.9 ± 0.1 | 13.6 ± 0.4 |
| | PU/Cu-BTC-1.0 | 18.1 | 1.9 ± 0.2 | 149.6 ± 16.8 | 19.9 | 1.7 ± 0.2 | 14.9 ± 0.9 |

Visual comparisons of the $D$ and $S$ values obtained for each membrane are shown in Figure 42 and Figure 43 respectively.

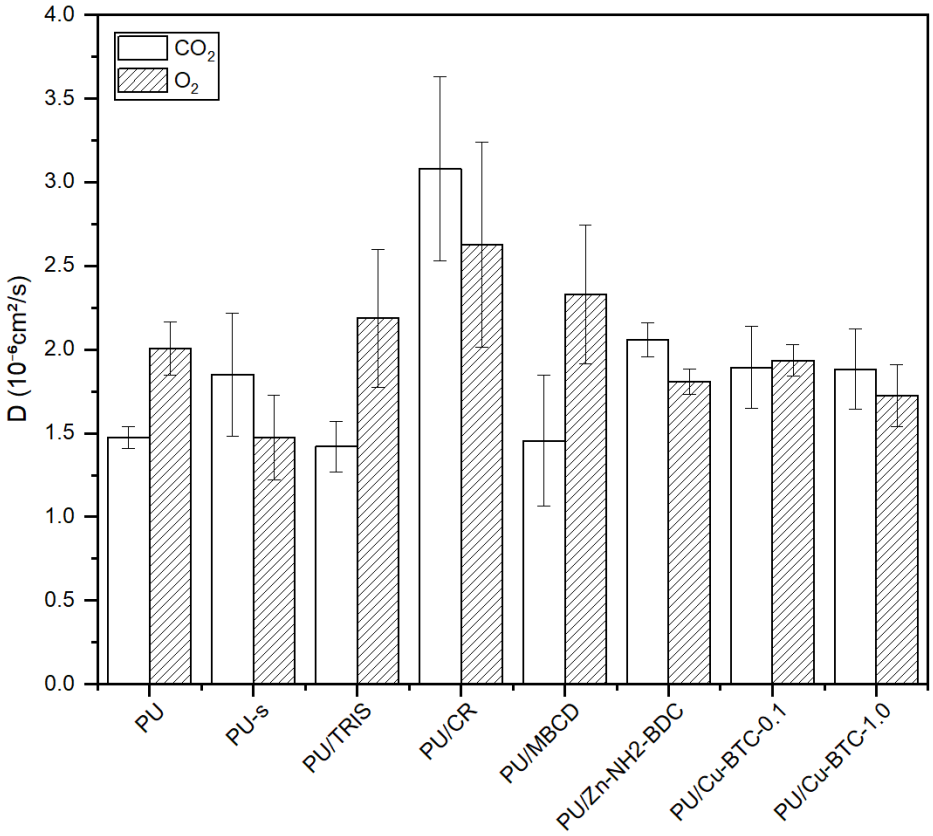


Figure 42. Average diffusion coefficients (D) towards $CO_2$ and $O_2$, and respective standard deviations for all the studied membranes.

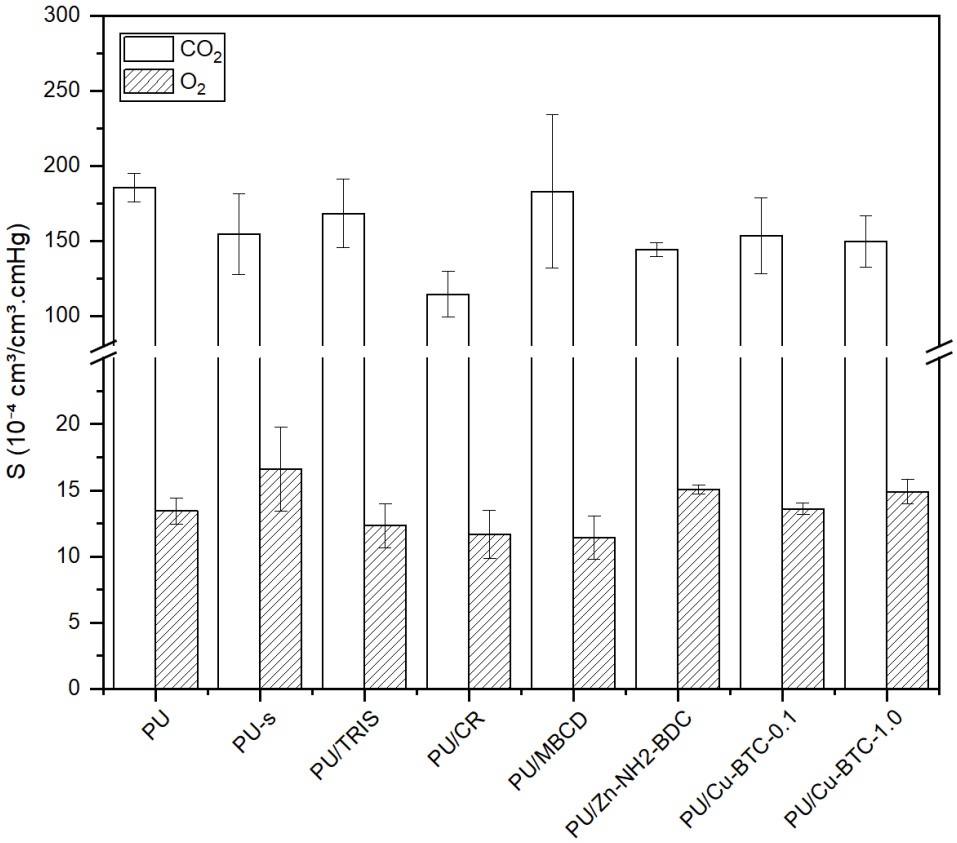


Figure 43. Average solubility coefficients (S) towards $CO_2$ and $O_2$, and respective standard deviations for all the studied membranes.

The diffusion coefficients of $CO_2$ and $O_2$ presented in Table 9 and Figure 42 all have the same order of magnitude and are comparable to the results found in previous studies for PU/PCL membranes, of $1.4x10^{-6}$ to $1.7\ x10^{-6}$ $cm^2/s$ for $CO_2$, and $1.6x10^{-6}$ to $2.1x10^{-6}$ $cm^2/s$ for $O_2$ [61]. In work by Eusebio et al. [26], higher diffusion coefficients were reported for $O_2$ than for $CO_2$, and these findings were justified by the polar character of $CO_2$ which promotes interactions with the matrix, thus hindering its mobility. However, no clear tendency can be observed in this work regarding which of the two gases presents the highest D values.

When compared to the pure PU and PU-s membranes, the PU/CR membrane shows the highest values of D for both gases. The remaining PU-based membranes, PU/TRIS and PU/MBCD, represent no improvement in the D values for $CO_2$ but a significant enhancement for the diffusion of $O_2$ when compared to the pure PU membranes. The MMMs present the most consistent results of all membranes, with slightly higher diffusion coefficients for both gases than the pure PU membranes.

When it comes to the solubility coefficients, the values found for $CO_2$ are one order of magnitude higher than for $O_2$ in all membranes. The main parameter influencing the solubility is the ease of condensation [52]. Since carbon dioxide has a higher boiling point than oxygen (-78.5°C and -183 °C, respectively), it is the most likely to condensate. Additionally, the solubility can be correlated to the critical temperature [11]. While the critical point of $CO_2$ (31.1 °C) is close to the temperature used during the gas permeation experiments (37 °C), $O_2$ has a negative critical temperature (-118.6 °C) implying that its condensation would not be possible even if the pressure was greatly increased.

Nevertheless, no clear trends can be observed among the solubility values of either gas across the various membranes. In terms of $CO_2$ solubility, all the pure PU and PU-based membranes exhibit comparable, except for the PU/CR composition which stands out with a lower S value. The $O_2$ solubility of all PU-based membranes is slightly lower than for the pure PU and PU-s membranes. Once again, the most consistent results are found across the MMMs which present intermediate solubilities values for $CO_2$ and $O_2$, with some of the smallest standard deviations. Overall, the solubility coefficients presented in Table 9 are comparable, and even represent a slight improvement, to the values previously reported by Martins [61] for PU/PCL membranes, which ranged from $119.2x10^{-4}$ to $160.0x10^{-4}$ $cm^3/cm^3.cmHg$ for $CO_2$ and from $9.6x10^{-4}$ to $11.9x10^{-4}$ $cm^3/cm^3.cmHg$ for $O_2$.

Finally, a combined examination of the coefficients presented in Table 5 and Table 9 suggests that the gas permeation through the studied compositions is a diffusion-controlled process, because while no significant trends can be detected among the solubility coefficients, the tendencies observed among the diffusion coefficients are identical to the ones observed in the permeability coefficients.

# 6. Conclusions

The gas permeation properties of novel polyurethane-based nonporous symmetric membranes were studied in this work. The experiments were carried out by the constant volume method at 37°C in an in-house built gas permeation set-up, which recorded the variation of permeate pressure over time, for a single gas through a membrane sample at a given constant feed pressure. Measurements were made for two main respiratory gases, carbon dioxide ($CO_2$) and oxygen ($O_2$), using receiving volumes of 26.1 $cm^3$ and 13.5 $cm^3$, respectively. From the permeate pressure vs. time curves, obtained at multiple feed pressures (ranging from 1.5 to 4 bar), it was possible to plot the steady state gas flux ($J$) as a function of the transmembrane pressure (TMP), thus determining the permeance and permeability coefficients of each membrane. Estimations of the diffusion and solubility coefficients were also calculated from the transient regions of the permeate pressure vs. time curves, through the time-lag method.

Three groups of nonporous symmetric membranes were prepared by the solvent evaporation technique: pure polyurethane, polyurethane-based and mixed matrix membranes (MMMs). The pure polyurethane membranes, PU and PU-s, were obtained from casting solutions of polyurethane (PU) with and without dimethylformamide (DMF) as the solvent. The polyurethane-based membranes, PU/TRIS, PU/CR and PU/MBCD, were prepared from casting solutions of PU and DMF with tris(hydroxymethyl) aminomethane (TRIS), Congo red (CR) and methyl-beta-cyclodextrin (MBCD). Finally, the MMMs, PU/Zn-$NH_2$-BDC, PU/Cu-BTC-0.1 and PU/Cu-BTC-1.0, were synthesized by incorporating Zn-$NH_2$-BDC and Cu-BTC metal organic frameworks (MOFs) into casting solutions of PU and DMF. The polymer to solvent ratios used were 65/35 for the PU-s and PU-based membranes, and 90/10 for the MMMs. The polyurethane to second reagent ratios used were 99.2/0.8 for PU/TRIS, 99.6/0.4 for PU/CR and PU/MBCD, 99.9/0.1 for PU/Zn-$NH_2$-BDC and PU/Cu-BTC-0.1, and 99/1 for PU/Cu-BTC-1.0. Other reagents, such as first generation polyurea dendrimers (PURE-G1), branched polyethylenimine (PEI), tris(2-aminoethyl)amine (TREN) and tannic acid (TA), were explored for the synthesis of other PU based membranes, but the casting operation could not be completed successfully.

The SEM images revealed that all membranes present a homogenous, dense cross-section with no visible pores. It appears that the addition of TRIS, CR and MBCD did not have any effect on the membrane morphology when compared to the pure PU membranes. The cross-section images of the PU/Zn-$NH_2$-BDC and PU/Cu-BTC-1.0 membranes showed the presence of small features which distinguished themselves from the polyurethane matrix. An EDS analysis of these membranes confirmed that the observed features were in fact Zn-$NH_2$-BDC and Cu-BTC (MOFs), respectively.

The average thickness of each membrane was obtained from the cross-sectional SEM images. The highest thickness (181 μm) was obtained for the PU membrane, and the lowest for the PU-s membrane (125 μm). All of the PU-based and MMMs exhibited intermediate thickness ranging from 137 to 149 μm and 143 to 152 μm, respectively. It was found that casting solutions with higher solvent content resulted in membranes of lower thickness.

All the studied membranes, as well as the PU prepolymer, were analyzed through ATR – FTIR spectroscopy. The spectra of all membranes exhibited the urethane/urea carbonyl stretching band at about 1730 $cm^{-1}$, but none presented a peak centered at 2278 $cm^{-1}$, corresponding to the asymmetric isocyanate stretching mode ($\upsilon_{as}$NCO), which is observable in the PU prepolymer spectrum. This implies that all the isocyanate groups probably reacted with the functional groups of the components present in the PU-based compositions (TRIS, CR and MBCD).

All the stress-strain curves obtained from the tensile tests carried out on the pure polyurethane and polyurethane-based membranes were similar in shape, exhibiting a behavior typical of elastomers. The initial Young's modulus, tensile strength and elongation at break were in the ranges of 2.3-8.0 MPa, 1.5-2.7 MPa, and 78.70-116.35 %, respectively. The pure PU membrane presented the highest elasticity modulus and tensile strength, and the PU/CR membrane had the highest elongation at break.

The pure PU and PU-s membranes exhibited permeability coefficients of 273 and 278 Barrer towards $CO_2$, and 27 and 24 Barrer towards $O_2$, respectively, For the PU-based membranes, $CO_2$ permeabilities of 237, 346, and 251 Barrer and $O_2$ permeabilities of 26, 30 and 26 Barrer were obtained for PU/TRIS, PU/CR and PU/MBCD, respectively. Regarding the MMMs, P values of 297, 287, 280 Barrer towards $CO_2$ and 27, 26 and 26 Barrer towards $O_2$ were found for PU/Zn-$NH_2$-BDC, PU/Cu-BTC-0.1 and PU/Cu-BTC-1.0, respectively.

All the $P_{CO2}$ values are one order of magnitude greater than the $P_{O2}$ values. When compared to the pure PU membranes, the composition that represents the biggest improvements in terms of $CO_2$ and $O_2$ permeabilities was PU/CR, followed by PU/Zn-$NH_2$-BDC and PU/Cu-BTC-0.1. The PU/TRIS and PU/MBCD membranes present some of the lowest permeability values, particularly for $CO_2$, suggesting that the addition of TRIS and MBCD does not bring any enhancement to the performance of the pure PU membrane. Furthermore, the increased MOF content in the PU/Cu-BTC-1.0 membrane does not yield improved permeation of either gas in relation to the PU/Cu-BTC-0.1 membrane. The great fluxes of $CO_2$ observed through the studied membranes resulted in estimated minimum membrane surface areas ranging from 0.6 to 1.0 $m^2$, which compares favorably to the membrane areas used in current commercial MBO of approximately 2$m^2$. However, the surface area requirements estimated from the $O_2$ fluxes, 7.8 to 10.8 $m^2$, still exceed the areas found in commercial MBOs. This indicates that the $O_2$ permeation properties are a limiting factor.

The diffusion coefficient ranges calculated through the time-lag method were $1.4x10^{-6}$-$3.1x10^{-6}$ $cm^2/s$ for $CO_2$, and $1.5x10^{-6}$-$2.6x10^{-6}$ $cm^2/s$ for $O_2$. These results followed the same trends observed for the permeability coefficients, with PU/CR having the highest value, followed by the MMMs, and with PU/TRIS and PU/MBCD exhibiting the lowest values. On the other hand, the solubility coefficients found ranged from $114.5x10^{-4}$ to $185.5x10^{-4}$ $cm^3/cm^3.cmHg$ for $CO_2$, and 11.4 $x10^{-4}$ to $16.6x10^{-4}$ $cm^3/cm^3.cmHg$ for $O_2$. All the solubility values were within the same order of magnitude and no significant tendencies could be observed among them. From these results, the permeation process of the respiratory gases through the studied membranes appears to be controlled by diffusion.

# 7. Perspectives of Future Work

Even though advances were made in the present work regarding the $O_2$ permeability coefficients of polyurethane-based membranes, further improvement is still needed. Therefore, a suggested next step for the continuation of this work is to study the effect of the reagent ratio on the gas permeation performance of the formulations that showed the most potential, namely the PU/CR, PU/Zn-$NH_2$-BDC and PU/Cu-BTC.

Another suggestion is to synthesize the new compositions in the form of integral asymmetric membranes (instead of nonporous symmetric membranes) with varying evaporation times, and to test them in the existing permeation set-up. In the past, the reduced thicknesses of the dense layer achieved for this type of membrane have resulted in improved gas permeation.

Since the gas exchange in an ECMO system takes place through a membrane that's placed in between blood and gas, all the membranes should be tested in a gas/membrane/liquid permeation set-up to evaluate if the results are consistent with the ones obtained in the existing gas/membrane/gas set-up.

Additionally, because these are novel membranes, hemocompatibility studies are recommended to determine their suitability for biomedical applications.

Lastly, the permeability to $N_2$, as well as to any other useful gases, of the membranes developed throughout this work should also be measured, to facilitate their adaptation to other gas separation applications.

# 8. Bibliography


[1] S. I. Fox, *Human physiology*, 14th Edition. New York, USA: McGraw-Hill Education, 2016.

[2] "The top 10 causes of death." https://www.who.int/news-room/fact-sheets/detail/the-top-10-causes-of-death (accessed Apr. 04, 2022).

[3] G. MacLaren, A. Combes, and R. H. Bartlett, "Contemporary extracorporeal membrane oxygenation for adult respiratory failure: life support in the new era," *Intensive Care Medicine*, vol. 38, no. 2, pp. 210–220, Feb. 2012.

[4] R. P. Barbaro *et al.*, "Extracorporeal membrane oxygenation support in COVID-19: an international cohort study of the Extracorporeal Life Support Organization registry," *The Lancet*, vol. 396, no. 10257, pp. 1071–1078, Oct. 2020.

[5] H. Iwahashi, K. Yuri, and Y. Nosé, "Development of the oxygenator: Past, present, and future," *Journal of Artificial Organs*, vol. 7, no. 3. pp. 111–120, Sep. 2004.

[6] P. M. Kapoor and Navin C Nanda, *Manual of Extracorporeal Membrane Oxygenation (ECMO) in the ICU*, First edition. Jaypee Brothers Medical Publishers (P) Ltd., 2014.

[7] D. F. Stamatialis *et al.*, "Medical applications of membranes: Drug delivery, artificial organs and tissue engineering," *Journal of Membrane Science*, vol. 308, no. 1–2. pp. 1–34, Feb. 01, 2008.

[8] G. Makdisi and I. W. Wang, "Extra Corporeal Membrane Oxygenation (ECMO) review of a lifesaving technology," *Journal of Thoracic Disease*, vol. 7, no. 7. Pioneer Bioscience Publishing, pp. E166–E176, 2015.

[9] P. M. Budd and N. B. McKeown, "Highly permeable polymers for gas separation membranes," *Polymer Chemistry*, vol. 1, no. 1. pp. 63–68, Mar. 2010.

[10] P. Bernardo, E. Drioli, and G. Golemme, "Membrane gas separation: A review/state of the art," *Industrial and Engineering Chemistry Research*, vol. 48, no. 10, pp. 4638–4663, May 2009.

[11] R. W. Baker and B. T. Low, "Gas separation membrane materials: A perspective," *Macromolecules*, vol. 47, no. 20, pp. 6999–7013, Oct. 2014.

[12] A. F. Ismail, K. Chandra Khulbe, and T. Matsuura, *Gas Separation Membranes: Polymeric and Inorganic*. Cham: Springer International Publishing, 2015.

[13] M. R. A. Hamid and H. K. Jeong, "Recent advances on mixed-matrix membranes for gas separation: Opportunities and engineering challenges," *Korean Journal of Chemical Engineering*, vol. 35, no. 8. Springer New York LLC, pp. 1577–1600, Aug. 01, 2018.

[14] R. Sidhikku Kandath Valappil, N. Ghasem, and M. Al-Marzouqi, "Current and future trends in polymer membrane-based gas separation technology: A comprehensive review," *Journal of Industrial and Engineering Chemistry*, vol. 98. Korean Society of Industrial Engineering Chemistry, pp. 103–129, Jun. 25, 2021.

[15] K.-V. Peinemann, "Membrane Based Gas Separation - past, presence and future," *Membrane*, vol. 31, no. 3, pp. 165–169, 2006.

[16] A. Kumar and R. K. Gupta, *Fundamentals of polymer engineering*, 2nd Edition. New York: Marcel Dekker, Inc., 2003.

[17] H. A. Mannan, H. Mukhtar, T. Murugesan, R. Nasir, D. F. Mohshim, and A. Mushtaq, "Recent applications of polymer blends in gas separation membranes," *Chemical Engineering and Technology*, vol. 36, no. 11. pp. 1838–1846, Nov. 2013.

[18] M. A. Aroon, A. F. Ismail, T. Matsuura, and M. M. Montazer-Rahmati, “Performance studies of mixed matrix membranes for gas separation: A review,” *Separation and Purification Technology*, vol. 75, no. 3. Elsevier B.V., pp. 229–242, Nov. 20, 2010.

[19] N. Kosinov, J. Gascon, F. Kapteijn, and E. J. M. Hensen, “Recent developments in zeolite membranes for gas separation,” *Journal of Membrane Science*, vol. 499. Elsevier, pp. 65–79, Feb. 01, 2016.

[20] A. M. Norouzi, M. Elyasi Kojabad, M. Chapalaghi, A. Hosseinkhani, A. Arabloo nareh, and E. Nemati Lay, “Polyester-based polyurethane mixed-matrix membranes incorporating carbon nanotube-titanium oxide coupled nanohybrid for carbon dioxide capture enhancement: Molecular simulation and experimental study,” *Journal of Molecular Liquids*, vol. 360, p. 119540, Aug. 2022.

[21] O. Mehmood *et al.*, “Optimization analysis of polyurethane based mixed matrix gas separation membranes by incorporation of gamma-cyclodextrin metal organic frame work,” *Chemical Papers*, vol. 74, no. 10, pp. 3527–3543, Oct. 2020.

[22] A. M. Norouzi, E. Nemati Lay, A. Arabloo nareh, A. Hosseinkhani, and M. Chapalaghi, “Functionalized nanodiamonds in polyurethane mixed matrix membranes for carbon dioxide separation,” *Results in Materials*, vol. 13, Mar. 2022.

[23] B. Molki, W. M. Aframehr, R. Bagheri, and J. Salimi, “Mixed matrix membranes of polyurethane with nickel oxide nanoparticles for CO2 gas separation,” *Journal of Membrane Science*, vol. 549, pp. 588–601, Mar. 2018.

[24] H. T. Afarani, M. Sadeghi, and A. Moheb, “The Gas Separation Performance of Polyurethane–Zeolite Mixed Matrix Membranes,” *Advances in Polymer Technology*, vol. 37, no. 2, pp. 339–348, Mar. 2018.

[25] R. W. Baker, *Membrane Technology and Applications*, 3rd ed. West Sussex, England: Wiley, 2012.

[26] T. M. Eusébio *et al.*, “Sorption/diffusion contributions to the gas permeation properties of bi-soft segment polyurethane/polycaprolactone membranes for membrane blood oxygenators,” *Membranes (Basel)*, vol. 10, no. 1, Jan. 2020.

[27] F. Wiese, “Membranes for Artificial Lungs,” in *Membranes for the Life Sciences*, Weinheim, Germany: Wiley-VCH Verlag GmbH & Co. KGaA, 2010, pp. 49–68.

[28] B. Meyns, L. Vercaemst, E. Vandezande, H. Bollen, and D. Vlasselaers, “Plasma Leakage of Oxygenators in ECMO Depends on the Type of Oxygenator and on Patient Variables,” *The International Journal of Artificial Organs*, vol. 28, no. 1, pp. 30–34, Jan. 2005.

[29] M. Faria, P. Brogueira, and M. N. de Pinho, “Sub-micron tailoring of bi-soft segment asymmetric polyurethane membrane surfaces with enhanced hemocompatibility properties,” *Colloids and Surfaces B: Biointerfaces*, vol. 86, no. 1, pp. 21–27, Aug. 2011.

[30] B. Applications, A. H. Mostafavi, A. Kumar Mishra, M. Ulbricht, J. F. M. Denayer, and S. S. Hosseini, “Oxygenation and Membrane Oxygenators: Emergence, Evolution and Progress in Material Development and Process Enhancement for Article info,” *Journal of Membrane Science and Research*, vol. 7, pp. 230–259, 2021.

[31] M. Faria, V. Geraldes, and M. N. de Pinho, “Surface characterization of asymmetric Bi-soft segment poly(ester urethane urea) membranes for blood-oxygenation medical devices,” *International Journal of Biomaterials*, vol. 2012, no. 6, Nov. 2011.

[32] D. P. Queiroz and M. N. de Pinho, “Structural characteristics and gas permeation properties of polydimethylsiloxane/poly(propylene oxide) urethane/urea bi-soft segment membranes,” *Polymer (Guildf)*, vol. 46, no. 7, pp. 2346–2353, Mar. 2005.

[33] M. Faria and M. N. de Pinho, “Phase segregation and gas permeation properties of poly(urethane urea) bi-soft segment membranes,” *European Polymer Journal*, vol. 82, pp. 260–276, Sep. 2016.

[34] M. C. Besteiro, A. J. Guiomar, C. A. Gonçalves, V. A. Bairos, M. N. de Pinho, and M. H. Gil, “Characterization and in vitro hemocompatibility of bi-soft segment, polycaprolactone-based poly(ester urethane urea) membranes,” *Journal of Biomedical Materials Research - Part A*, vol. 93, no. 3, pp. 954–964, Jun. 2010.

[35] C.-T. Zhao and M. Norberta De Pinho, “Design of polypropylene oxide/polybutadiene bi-soft segment urethane/ urea polymer for pervaporation membranes,” *Polymer (Guildf)*, vol. 40, no. 22, pp. 6089–6097, 1998.

[36] M. M. Cipriano, A. Diogo, and M. Norberta De Pinho, “Polyurethane structure design for pervaporation membranes*,” *Journal of Membrane Science*, vol. 61, pp. 65–72, 1991.

[37] D. P. Queiroz and M. N. Pinho, “Gas permeability of polypropylene oxide/polybutadiene bi-soft segment urethane/urea membranes,” *Desalination*, vol. 145, no. 1, pp. 379–383, 2002.

[38] D. P. Queiroz, M. N. de Pinho, and C. Dias, “ATR-FTIR studies of poly(propylene oxide)/polybutadiene bi-soft segment urethane/urea membranes,” *Macromolecules*, vol. 36, no. 11, pp. 4195–4200, Jun. 2003.

[39] M. Faria, M. Rajagopalan, and M. N. de Pinho, “Tailoring bi-soft segment poly (ester urethane urea) integral asymmetric membranes for CO2 and O2 permeation,” *Journal of Membrane Science*, vol. 387–388, no. 1, pp. 66–75, Jan. 2012.

[40] Y. T. Dang *et al.*, “Room temperature synthesis of biocompatible nano Zn-MOF for the rapid and selective adsorption of curcumin,” *Journal of Science: Advanced Materials and Devices*, vol. 5, no. 4, pp. 560–565, Dec. 2020.

[41] A. Justin, J. Espín, I. Kochetygov, M. Asgari, O. Trukhina, and W. L. Queen, “A Two Step Postsynthetic Modification Strategy: Appending Short Chain Polyamines to Zn-NH2-BDC MOF for Enhanced CO2Adsorption,” *Inorganic Chemistry*, vol. 60, no. 16, pp. 11720–11729, Aug. 2021.

[42] H. Wang *et al.*, “Membrane adsorbers with ultrahigh metal-organic framework loading for high flux separations,” *Nature Communications*, vol. 10, no. 1, Dec. 2019.

[43] L. Zhu, X. Q. Liu, H. L. Jiang, and L. B. Sun, “Metal-Organic Frameworks for Heterogeneous Basic Catalysis,” *Chemical Reviews*, vol. 117, no. 12. American Chemical Society, pp. 8129–8176, Jun. 28, 2017.

[44] L. J. Murray, M. Dinc, and J. R. Long, “Hydrogen storage in metal-organic frameworks,” *Chemical Society Reviews*, vol. 38, no. 5, pp. 1294–1314, 2009.

[45] T. M. Eusébio, “Polyurethane urea membranes for membrane blood oxygenators: synthesis and gas permeation properties,” Master of Science, Instituto Superior Tecnico, Lisbon, 2017.

[46] “Fiji.” https://imagej.net/software/fiji/ (accessed May 21, 2022).

[47] H. M. C. C. Somarathna, S. N. Raman, D. Mohotti, A. A. Mutalib, and K. H. Badri, “Rate dependent tensile behavior of polyurethane under varying strain rates,” *Construction and Building Materials*, vol. 254, Sep. 2020.

[48] Z. Bai *et al.*, “Microstructure and mechanical properties of polyurethane fibrous membrane,” *Fibers and Polymers*, vol. 13, no. 10, pp. 1239–1248, Dec. 2012.

[49] D. de Meis, “Overview on porous inorganic membranes for gas separation.” ENEA - Italian National Agency for New Technologies, Energy and Sustainable Economic Development, Rome, 2017.

[50] A. Fuoco *et al.*, “Gas transport in mixed matrix membranes: Two methods for time lag determination,” *Computation*, vol. 8, no. 2, Jun. 2020.

[51] G. S. Park, “Transport Principles—Solution, Diffusion and Permeation in Polymer Membranes,” in *Synthetic Membranes: Science, Engineering and Applications*, Dordrecht: Springer Netherlands, 1986, pp. 57–107.

[52] M. Mulder, *Basic Principles of Membrane Technology*, 2nd Edition. Kluwer Academic Publishers, 1996.

[53] R. M. Barrer and E. K. Rideal, “Permeation, diffusion and solution of gases in organic polymers,” *Trans. Faraday Soc.*, pp. 628–643, 1934.

[54] S. W. Rutherford and D. D. Do, “Review of Time Lag Permeation Technique as a Method for Characterisation of Porous Media and Membranes,” Kluwer Academic Publishers, 1997.

[55] “Software & Manuals - Paroscientific, Inc.” https://paroscientific.com/software_manuals.php (accessed May 21, 2022).

[56] G. Pon, “Gas permeation in bi-soft segment poly(ester urethane urea) membranes for Membrane Blood Oxygenators,” Master of Science, Instituto Superior Tecnico, Lisbon, 2018.

[57] “SEM Signal - Electron Imaging - Accelerating Microscopy. ” https://www.thermofisher.com/blog/microscopy/sem-signal-types-electrons-and-the-information-they-provide/ (accessed May 03, 2022).

[58] W. E. Wallace, “Carbon dioxide,” *NIST Mass Spectrometry Data Center*. https://webbook.nist.gov/cgi/inchi?ID=C124389&Type=IR-SPEC&Index=0 (accessed May 28, 2022).

[59] J. E. Mark, “Rubber Elasticity,” *Journal of Chemical Education*, vol. 58, no. 11, pp. 898–903, 1981.

[60] F. P. Beer, E. R. Johnston, J. T. DeWolf, and D. F. Mazurek, *Mechanics of Materials*, 8th Edition. New York, NY: McGraw-Hill Education, 2020.

[61] A. R. Gonçalves Varandas Martins, “Characterization and Gas Permeation Properties of Blood Compatible Membranes for Blood Oxygenators,” Master of Science, Instituto Superior Tecnico, Lisbon, 2019.

[62] S. Escorihuela *et al.*, “Study of the effect of inorganic particles on the gas transport properties of glassy polyimides for selective CO2 and H2O separation,” *Membranes (Basel)*, vol. 8, no. 4, Jan. 2018.

[63] M. Maghami and A. Abdelrasoul, “Zeolite Mixed Matrix Membranes (Zeolite-MMMs) for Sustainable Engineering,” in *Zeolites and Their Applications*, InTech, 2018, pp. 115–134.

[64] D. N. Gray, “Polymeric Membranes for Artificial Lungs,” in *Polymeric Materials and Artificial Organs*, 1984, pp. 151–162.

[65] M. C. Faria Besteiro, “Development of poly(ester urethane urea) membranes for Extracorporeal Membrane Blood Oxygenators,” PhD, Instituto superior Tecnico, Lisbon, 2012.

[66] R. B. Restani, P. I. Morgado, M. P. Ribeiro, I. J. Correia, A. Aguiar-Ricardo, and V. D. B. Bonifácio, “Biocompatible polyurea dendrimers with pH-dependent fluorescence,” *Angewandte Chemie - International Edition*, vol. 51, no. 21, pp. 5162–5165, May 2012.

# Appendix A

Multiple alternative reagents were tested, in addition to the ones described in section 4.1.1., for the formation of polyurethane-based membranes. The first one was first generation polyurea dendrimers (PURE-G1) with a MW of 662.6 Da, provided by prof. Vasco Bonifácio, which had been synthesized according to previously reported methods [66]. The second reagent that was introduced was branched polyethylenimine (PEI) provided by Sigma-Aldrich (St. Louis, MO, USA). The third component used was tris(2-aminoethyl) amine (TREN) (purity of 97%) provided by Alfa Aesar (Haverhill, MA, USA). Figure 44 depicts the chemical structures of the PURE-G1, PEI and TREN reagents.

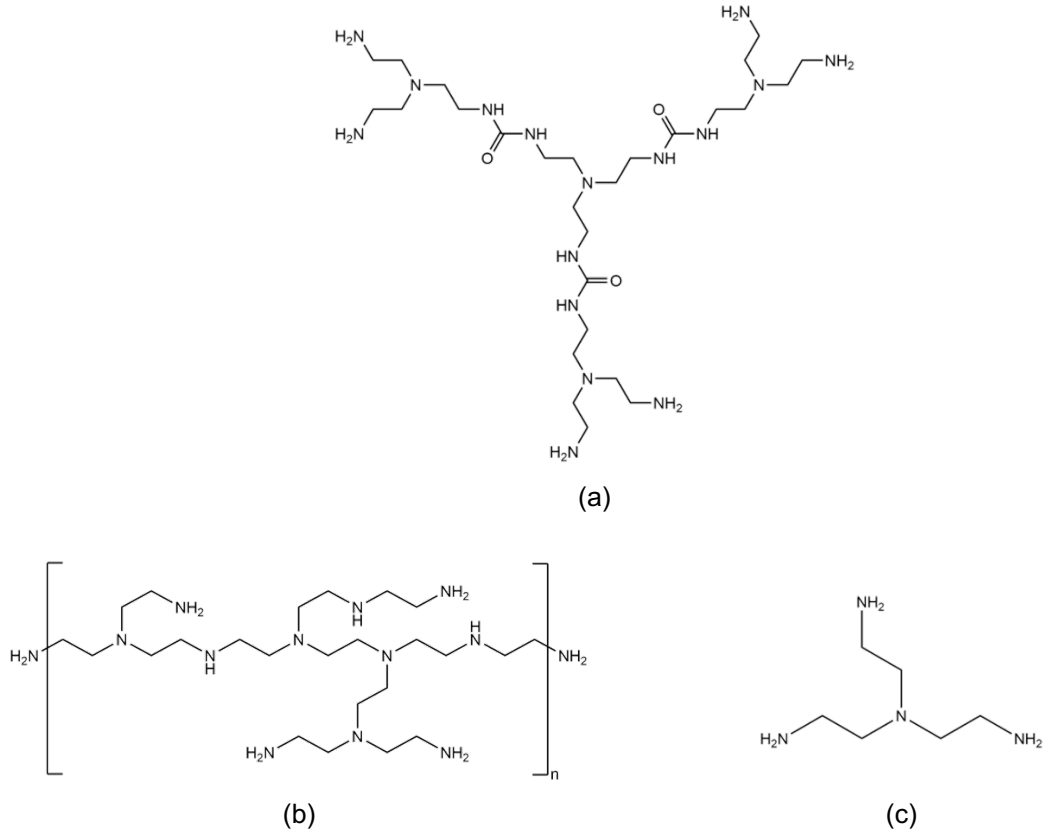

Figure 44. Chemical structures of: a) PURE-G1, b) PEI and c) TREN.

Each reagent was first dissolved in DMF solvent, and then added to polyurethane prepolymer, producing three different casting solutions which were subjected to magnetic agitation. In each case, the total polymer to solvent wt% ratio used was 90/10, and the polyurethane to second reagent wt% ratio was 95/5 for PURE-G1 and 99/1 for PEI and TREN. The goal was to cast each solution after the 2 hours of agitation to form PU-based membranes. However, within 15 to 30 minutes of agitation, solid masses started forming in each solution, making it impossible to proceed with the casting operation. Photographs of the precipitates formed inside each casting solution are presented in Figure 45.

(a) (b) (c)

Figure 45. Photographs of the precipitates that formed inside the casting solutions for: a) PU/PURE-G1, b) PU/PEI and c) PU/TREN.

Finally, tannic acid (TA) provided by Sigma-Aldrich (St. Louis, MO, USA), was also tested for the synthesis of PU-based membranes. The chemical structure of the TA is shown in Figure 46.

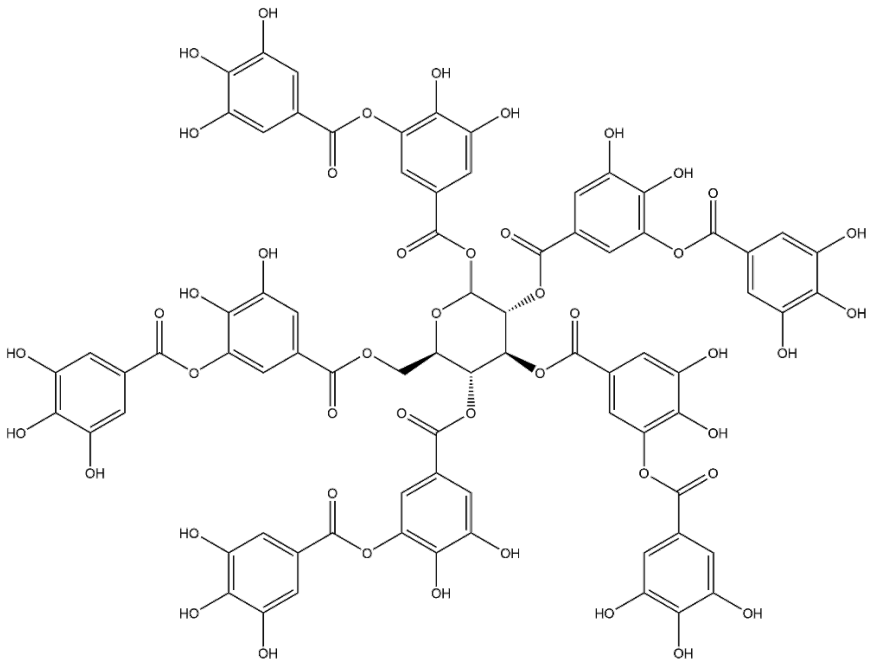

Figure 46. Chemical structure of tannic acid.

Over time, various batches of casting solutions containing PU and TA were prepared, with total polymer to DMF wt% ratio of 65/35 and polyurethane to tannic acid wt% ratio of 99.6/0.4. Each solution was submitted to 2 hours of magnetic agitation, cast on a glass plate using a 250 μm casting knife and removed in a water bath after curing at atmospheric conditions for 48 hours. However, when tested in the gas permeation set-up, no meaningful results could be obtained, as all the membranes appeared to contain pinholes.

# Appendix B

Before loading each membrane sample into the cell of the experimental gas permeation set-up, the thickness was measured using a Magnusson Vernier manual caliper (Longpont-sur-Orge, France). Additionally, the thicknesses of the pure PU and PU-based specimens used in the tensile tests were also measured prior to testing, using a Dexter® digital caliper (Lezennes, France). The average thickness values obtained with both the manual and digital calipers are presented in Table 10.

Table 10. Average thickness ($\ell$) and respective standard deviation of the nonporous symmetric PU membranes from groups 1, 2 and 3, obtained with manual and digital calipers.

| | **Membrane** | **Thickness, $\ell$ (μm)** | |
|---|---|---|---|
| | | **Manual Caliper** | **Digital Caliper** |
| Group 1 | PU | 213 ± 5.2 | 138 ± 5.0 |
| | PU-s | 196 ± 9.4 | 122 ± 11.1 |
| Group 2 | PU/TRIS | 191± 8.7 | 103 ± 7.8 |
| | PU/CR | 192 ± 12.6 | 134 ± 23.6 |
| | PU/MBCD | 197 ± 11.3 | 101 ± 2.5 |
| Group 3 | PU/Zn-$NH_2$-BDC | 199 ± 1.8 | |
| | PU/Cu-BTC-0.1 | 201 ± 2.2 | |
| | PU/Cu-BTC-1.0 | 200 ± 2.8 | |

# Appendix C

The wavelengths of the main characteristic peaks observed in the ATR-FTIR spectra of the pure PU, PU-based and MMM membranes are presented in Table 11.

Table 11. Assignments of the ATR-FTIR spectra of the PU prepolymer and the PU-based membranes.

| Wavenumber ($cm^{-1}$) | | Assignment | Reference |
|---|---|---|---|
| **PU prepolymer** | **PU based membranes** | | |
| $3323_{w,br}$ | $3323_{w,br}$ | $\upsilon$NH | [34] |
| $2857_{m}$ | $2857_{m}$ | $\upsilon CH_2$ | [33] |
| $2278_{s}$ | - | $\upsilon_{as}$NCO | [34] |
| $1725_{m}$ | $1725_{m}$ | $\upsilon$C=O | [34] |
| $1215_{m}$ | $1215_{m}$ | $\delta$NH and $\upsilon$CN | [33] |
| $1085_{vs}$ | $1085_{vs}$ | $\upsilon_{as}$COC (urethane and ether aliphatic) | [34] |

$_{VS}$ - very strong; $_{S}$ -strong; $_{m}$ - medium; $_{w}$ - weak; $_{vw}$ - very weak; $_{sh}$ - shoulder; $_{br}$ – broad